DEVELOPMENT AND OPERATION OF A SOLAR LIMB AO SYSTEM

BY

GREGORY EDWARD TAYLOR, B.S., M.S.

A dissertation submitted to the Graduate School

in partial fulfillment of the requirements

for the degree

Doctor of Philosophy

Major Subject: Astronomy

New Mexico State University

Las Cruces New Mexico

April 2014

"Design and Operation of a Solar Limb Adaptive Optics System" a dissertation prepared by Gregory E. Taylor in partial fulfillment of the requirements for the degree, Doctor of Philosophy, has been approved and accepted by the following:

Linda Lacey
Dean of the Graduate School

R. T. James McAteer
Chair of the Examining Committee

Date

Committee in charge:

Dr. R. T. James McAteer, Chair

Dr. Thomas R. Rimmele

Dr. Jason J. Jackiewicz

Dr. Bernard McNamera

Dr. David Voelz

DEDICATION

I dedicate this work to my parents and to my grandparents. Particularly my grandfather, Jack C. Hooper, who with his wife, Daris, spent so much time with me during my childhood. I will ever be grateful to them for their generosity and kindness. His example of hard work has helped me to get out of bed in the morning, even when this project was facing delays and my efforts seemed futile.

ACKNOWLEDGMENTS

I'd like to thank the staff of the Dunn Telescope at Sacramento Peak for their continual help in bringing this project about. In particular, I'd like to thank Doug Gilliam, the principal observer at the Dunn, for his help and advice.

VITA

EDUCATION

2007-2011 M.S., Astronomy
New Mexico State University, with Honors
Las Cruces, New Mexico, USA

2000-2007 B.S., Physics
University of Utah
Salt Lake City, Utah, USA

AWARDS AND GRANTS

2011-2014 NMSU Graduate Research Enhancement Grant

PROFESSIONAL ORGANIZATIONS

American Astronomical Society (& Solar Physics Division)

International Dark Sky Association.

PUBLICATIONS

Taylor, G. E., Schmidt, D., Marino, J. Rimmele, T. R., McAteer, R. T. J. 2014, *Performance Testing of an Off-Limb Solar Adaptive Optics System* Submitted to Solar Physics.

Hoffman, D. I.; Harrison, T. E.; Coughlin, J. L.; McNamara, B. J.; Holtzman, J. A.; Taylor, G. E.; Vestrand, W. T. *New Beta Lyrae and Algol Candidates from the Northern Sky Variability Survey 2009, AJ, 136, 1067.*

CONFERENCE PROCEEDINGS

Taylor, G. E., Rimmele, T. R., Marino, J., McAteer, R. T. J. 2013, in Society of Photo-Optical Instrumentation Engineers (SPIE) Conference Series, Vol. 8862, Society of Photo-Optical Instrumentation Engineers (SPIE) Conference Series

Taylor, G. E., Rimmele, T. R., Marino, J., Tritschler, A., McAteer, R. T. J. 2012, in Astronomical Society of the Pacific Conference Series, Vol. 463, Second ATST-EAST Meeting: Magnetic Fields from the Photosphere to the Corona., ed. T. R. Rimmele, A. Tritschler, F. Wöger, M. Collados Vera, H. Socas-Navarro, R. Schlichenmaier, M. Carlsson, T. Berger, A. Cadavid, P. R. Gilbert, P. R. Goode, & M. Knölker, 321

FIELD OF STUDY

Major Field: Solar Physics & Adaptive Optics

ABSTRACT

DEVELOPMENT AND OPERATION OF A SOLAR LIMB AO SYSTEM

BY

GREGORY EDWARD TAYLOR, B.S., M.S.

Doctor of Philosophy

New Mexico State University

Las Cruces, New Mexico, 2014

Dr. R. T. James McAteer, Chair

An Adaptive Optics system capable of locking-on to off-limb prominence structure has been proven successful. It has been shown to allow for diffraction limited spectroscopy and polarimetry of prominence structure. Spectroscopic data obtained using the Off-Limb AO system have been shown to contain a trove of information regarding the nature of solar prominences. In particular a Rayleigh-Taylor instability was seen in part of this data set. Such instabilities, and the rising plumes that result from them, are thought to be critical clues to the long-term persistence of quiescent solar prominences. This adaptive optics system will allow scientists to come one step closer to understanding the true nature of solar prominences.

Contents

LIST OF TABLES

LIST OF FIGURES

1. INTRODUCTION

1.1. What are Solar Prominences?

The sun is the central object in our solar system. It provides heat and light to our world and drives our weather. No life on earth would be possible without the sun. Since the sun is such an important part of our lives, it is useful to learn about it. The interior of the sun is divided into three main layers, the "core", the "radiative zone", and the "convective zone". The core is where the sun generates its energy via nuclear fusion of hydrogen into helium. It extends from the very center of the sun to about 0.2 solar radii. The radiative zone is a region which is so dense that it takes light about 100,000 years on average to pass through it. It extends to about 0.7 solar radii. Above this zone, convection is possible. This convection transports energy to what we call the surface of the sun. This surface constitutes the point on the sun where the optical depth is small enough to allow most light to freely escape. This layer is called the "photosphere". It is only a few hundred km deep.(Carrol & Ostlie 1996)

Above the surface of the sun, the atmosphere of the sun consists of two main layers, the "chromosphere" and the "corona". Each of these layers is hotter than the one below. The solar surface, at $\tau = 2/3$, has a temperature of about 5800 K. The chromosphere, which is about 2,000 km thick, has a temperature of up to 25,000 K. The temperature of the corona can reach millions of degrees. It extends out to more than two solar radii. Above the corona proper, the solar wind, which consists of charged particles, expelled from the sun at high speed, extends to the very edge of the solar system.(Carrol & Ostlie 1996)

The magnetic field of the sun is thought to be generated deep within the

convective zone. It is probably strengthened by the churning motions within the convective zone. The magnetic field of the sun extends out to the farthest reaches of the solar system. It interacts with the magnetic fields of the earth and other planets. These interactions cause what is known as "space weather".(Schrijver & Siscoe 2009) Where the magnetic field is strongest on the surface of the sun, so called "active regions" are formed. These may be seen as visible sun spots and are also the source for solar flares, highly energetic explosions on the sun which will be further discussed in Section 1.1.1.(Schrijver & Siscoe 2009)

Solar prominences consist plasma at the temperature of the solar chromosphere, which is suspended in the lower corona. These prominences can form over active regions or over less active regions, called quiescent regions. (Labrosse et al. 2010; MacKay et al. 2010) (Rimmele, Private Communication (2011)) In either case the magnetic field of the sun keeps the plasma suspended. In Figure 1.1, three images of solar prominences are shown. Image (a) shows a prominence which forms over an active region. These prominences are generally form close to the chromosphere, just a few times higher above the photosphere than the top of the chromosphere its self. Active region prominences generally have a horizontal filamentary structure.(Berger 2014) Images (b) and (c) show two different prominences which form over quiescent regions, these are called quiescent prominences. They generally have a vertical filamentary structure. (Berger 2014) The reason that active and quiescent prominences show different filamentary structure orientation is as yet unclear.(MacKay et al. 2010)

When a solar prominence is seen on the solar disk, it is often called a filament.(Labrosse et al. 2010; MacKay et al. 2010) Figure 1.2 shows three images which demonstrate the nature of solar filaments, prominences seen above the solar

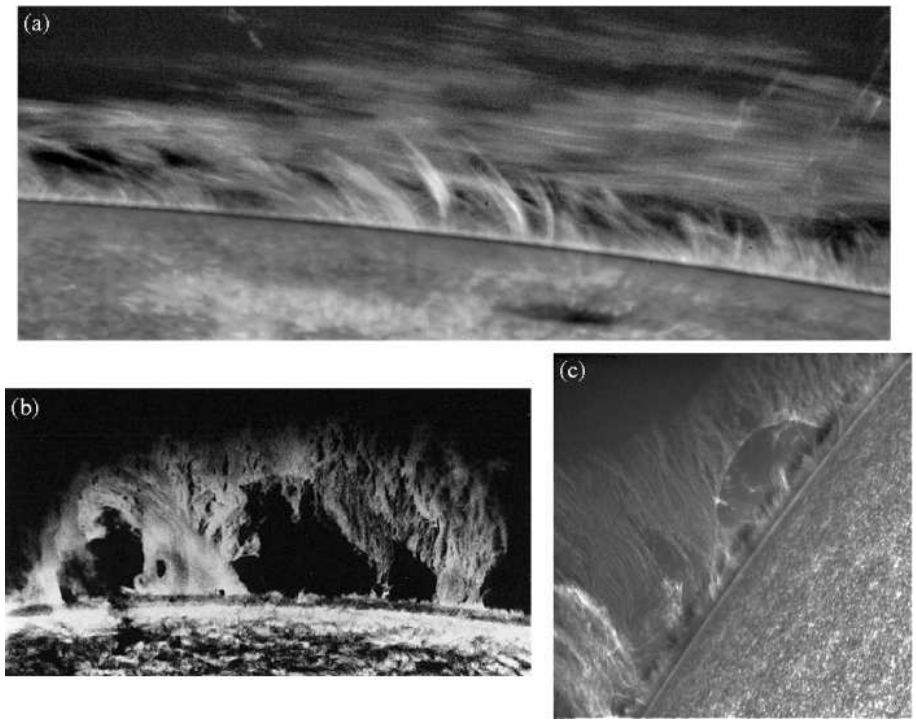

Fig. 1.1.— Three views of active and quiescent prominences. (a) Active region prominence, showing horizontal fibers, Ca II H image, from Hinode. (b) Quiescent prominence, Hα image from DST. (c) Quiescent prominence, showing vertical fibers, Ca II H image, from Hinode. DST. (from MacKay et al. 2010)

disk. Images (a) and (b) show images of the same filament, taken with different instruments. Note the thorn-like structures, these are called barbs. Barbs, when seen above the limb, extend down to the chromosphere.(MacKay et al. 2010) Image (c) shows the magnetic field configurations of the filament images in image (b). Note that the magnetic field changes polarity directly under the filament. This will be explained further below.

As seen in Figure 1.1, prominences are made up fibers of relatively cool plasma, suspended in the hot corona. Figure 1.3 shows the possible makeup of each individual fiber. The center of each fiber is cooler and denser than the surrounding material, it emits Hα light. Moving out from the center of the fiber, the gas

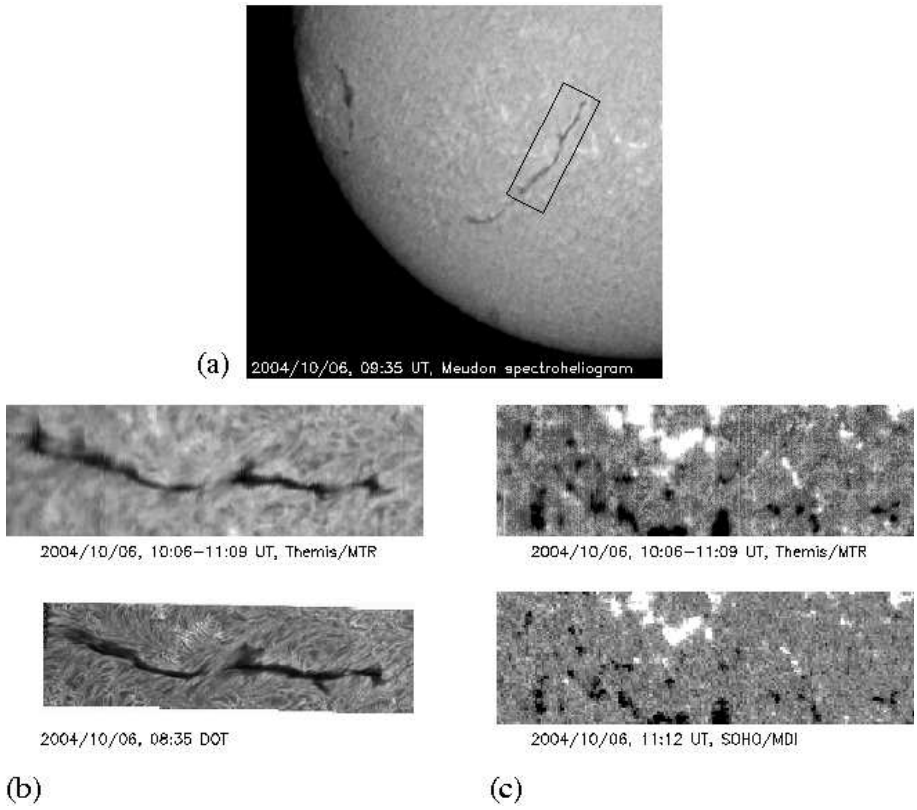

Fig. 1.2.— (a), (b) Two views of a solar filament, which is a prominence, viewed above the solar disk, Hα images. (c) Magnetogram of the prominence in figure (b). (from MacKay et al. 2010)

becomes hotter and more rarefied, emitting in more strongly ionized species. The hotter gas surround a prominence is called the Prominence-Corona-Transition-Region (PCTR). The higher the prominence fiber is within the corona, the smaller it is.

Prominences form above areas on the solar photosphere, where the magnetic field reverses polarity. This region is called a Polarity Inversion Line (PIL), as mentioned in Figure 1.2. Figure 1.4 shows the nature of a PIL. The left image shows that along one side of the PIL, the small chromospehric fibers point in one direction. Along the opposite side, they point in the opposite direction. The right

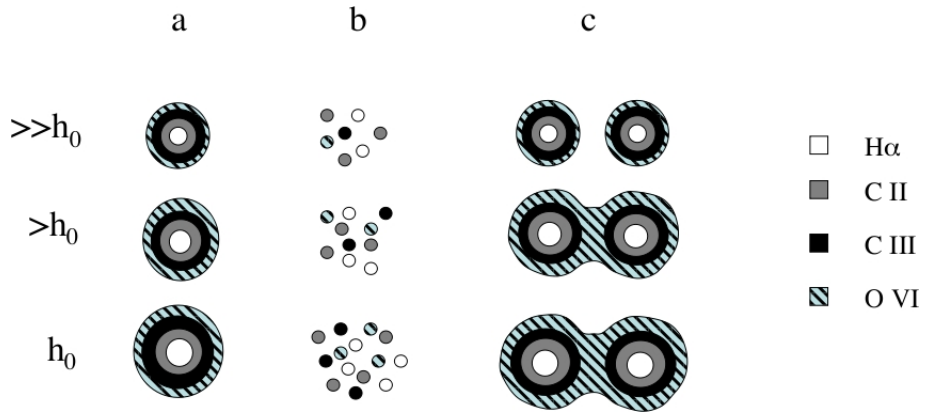

Fig. 1.3.— A model of the possible nature of each individual fiber. (a) An edge on view of an individual fiber, showing the different ionization regions. As one moves higher into the Solar Corona, more of the fiber will ionize, making the fiber smaller. (b) The cores of individual fibers may be at different temperatures. (c) Individual fibers, which may have been connected lower down, will be separated, higher into the Corona (from Labrosse et al. 2010)

image clarifies this phenomenon by showing a 3D representation of the magnetic field near a PIL. The magnetic field vectors are seen to point in opposite directions, on either side of the PIL.

The prominence itself forms within a magnetic flux rope. A flux rope is a long, twisted magnetic field region, which doesn't have a change in magnetic potential, along its length. Such a flux rope may form either from the shearing of magnetic arcades, or it may emerge from below the photosphere, already formed.(MacKay et al. 2010)

Figure 1.5 shows a possible mechanism for the formation of a magnetic flux rope above the solar surface. The left image shows that shearing motions within the solar material cause magnetic loops, called arcades, to be stretched to the breaking point. They then re-connect to form a rope-like magnetic structure. This process repeats until a flux rope is formed, as in the right image of Figure

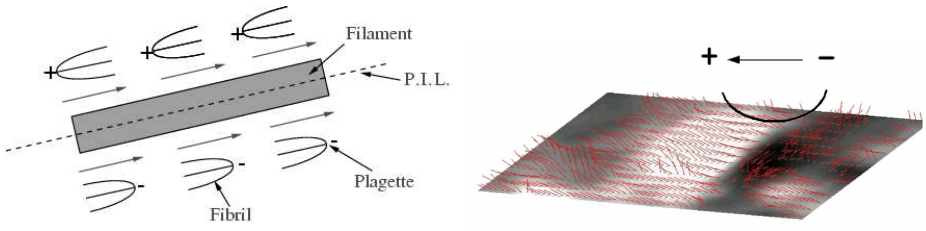

Fig. 1.4.— Left: A schematic representation of a Polarity Inversion Line (PIL), with a prominence above it. This schematic also shows the direction that small fibers in the chromosphere seem to point, when a prominence is viewed from above. Right: A simulated magnetogram, showing a PIL. (from MacKay et al. 2010) See also Figure 1.2(c).

1.5.

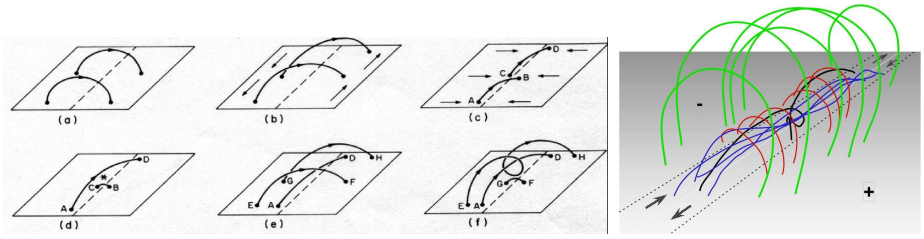

Fig. 1.5.— Left: A representation of the formation of a flux rope. Shearing motions within the photosphere cause magnetic arcades to be stretched. This continues until magnetic reconnections cause a flux rope to form. Right: A magnetic flux rope with larger magnetic arcades above it (from MacKay et al. 2010).

1.1.1. Why are Prominences Important?

One main reason that the study of solar prominence should be considered important is that they are often involved in Coronal Mass Eruptions (CMEs). CMEs occur when a flux rope becomes unstable. Since flux ropes very often contain solar prominences, prominences may show instabilities that could be used to predict an imminent CME (from Chen 2011). See Figure 1.6.

It is thought that emerging magnetic flux may cause the reconnections that

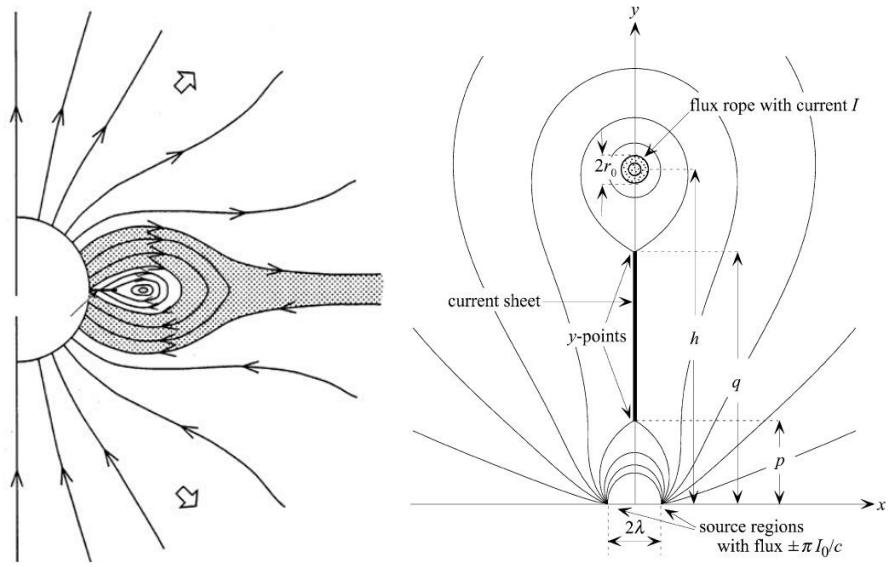

Fig. 1.6.— Left: An end on view of a flux rope. A solar prominence is shown as the thick line, perpendicular to the disk of the sun. Right: A flux rope is naturally buoyant. As the surrounding magnetic arcades undergo reconnections, the flux rope explodes violently upward (from Chen 2011) (Rimmele, Private Communication (2011)).

lead to CMEs, as shown in Figure 1.7 (e.g. Chen 2011). When a CME strikes the Earth's magnetic field, it causes what is known as a Solar Storm. Solar storms can directly impact our high-tech lives.

Despite continuing study of solar prominences, there is still much that is unknown about their physical and magnetic structure at small spatial scales.(Berger 2014; Labrosse et al. 2010; MacKay et al. 2010) There are ambiguities related to the broadening of spectral emission lines of prominences that are attributed to unresolved fine structure.(Labrosse et al. 2010) Thus the ability to measure spectra of solar prominences at very fine spatial scales is necessary to our understanding of solar prominences. Since solar prominence plasma interacts with the magnetic field in which it resides, an understanding of prominence dynamics can only be understood by the inversion of spectro-polarimetric data.(MacKay

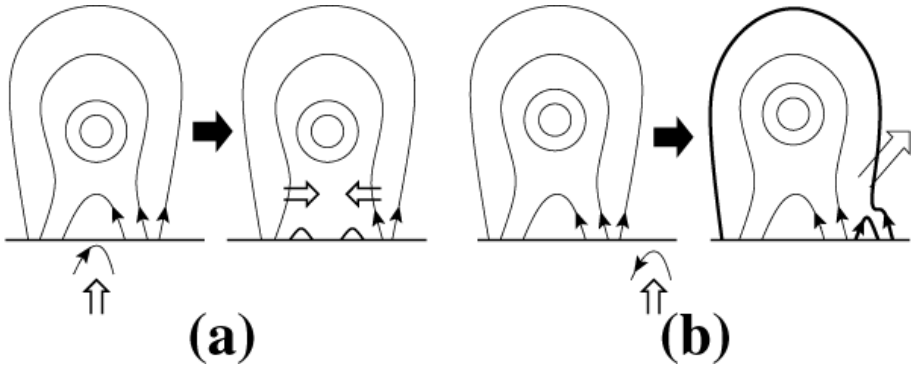

Fig. 1.7.— Left: Emerging magnetic flux, of a polarity opposite to that of the ambient field, emerges from the photosphere. This flux emerges at the center of the magnetic arcade, causing collapse. Right: The emerging flux is on the edge of the arcade. This too will cause instabilities and an eventual CME. (from Chen 2011)

et al. 2010) There are many ambiguities about prominence behavior, with respect to their magnetic fields, at the small spatial scales because these structures are unresolved.(MacKay et al. 2010) Space based instruments are capable of imaging solar prominences at very fine spatial scales.(Berger et al. 2011) However, to our knowledge, none has been launched that can perform spectro-polarimetry on a solar prominence, which is necessary for the understanding of prominence magnetic fields.(Tandberg-Hanssen 1995; MacKay et al. 2010)

Ground based telescopes have instruments which are capable of taking spectral and spectro-polarimetric data, for example IBIS and FIRS on the Dunn Solar Telescope (DST), in New Mexico.(Cavallini 2006; Jaeggli et al. 2010) Current solar AO systems are designed to utilize broad band light and are thus confined to locking onto structures on the disk of the sun; prominences are invisible in broadband light.(Rimmele & Marino 2011) This limits the usefulness of current solar AO systems. They can only be used to correct prominence images, and hence provide high resolution spectral or spectro-polarimetric data when there is a pore or other

Fig. 1.8.— A cartoon that shows the different aspects of our lives that can be affected by solar storms. First: The excessive radiation can be harmful to astronauts. It can also scramble signals from GPS satellites, causing ships, and other vehicles, to go astray. Solar storms can cause airliners to lose radio communication, especially near the poles, costing time and money. Solar storms can induce currents in the ionosphere. These currents can induce high voltage differences in transmission lines, shorting out transformers. These induced voltages can even cause pipelines to corrode. Finally, if the solar storm is powerful enough, the induced currents in the ionosphere can trick birds' internal navigation system, causing them to go astray. During a bad solar storm, one can't even communicate via carrier pigeon (from NASA Mission to Geospace 2011).

dark feature directly adjacent to the part of the limb near the prominence, as was done by Orozco Suárez et al. (2013). These data, however, are fundamentally limited in resolution because AO systems can only provide their best correction extremely close to the point upon which they are locked.(Hardy 1998) Only a purpose-built AO system that can directly lock onto solar prominence structure can allow for spectroscopic and spectro-polarimetric data at the diffraction limit

of the telescope. Thus allowing for an increase in our understanding of solar prominences.

We are the first to construct an Off-Limb solar AO system mainly because of the difficulty in measuring the incoming wavefront using only light from solar prominences. The main issue is photon flux. We have chosen to utilize Hα light from solar prominences because they emit very brightly at this wavelength, relative to other spectral lines. Even so, the required 0.5 - 0.7 Å filter bandwidth transmits very little flux. Thus, need to use all available Hα light, for the Wavefront Sensor (WFS). When we are able to measure the wavefront, using faint solar prominence detail, an entire AO system will need to be designed and optimized, to utilize these measurements. It is not possible to simply put a new WFS on an existing AO system. The difficulty of measuring the wavefront, coupled with the need to design an entirely new AO system, is the reason why we are the first to build an off-limb solar AO system. (For a review of specific problems of Solar AO in general, we refer to the earlier, comprehensive reviews of Rimmele & Radick (1998) and Rimmele & Marino (2011).)

1.2. Introduction to Adaptive Optics

Air changes its refractive index as it changes in temperature and humidity. Since air is constantly in motion, astronomers must constantly look through turbulent air. Adaptive Optics (AO) are designed to partially correct the distorted images that are the result of this phenomenon. (e.g. Hardy 1998; Roddier 1999; Tyson 2000, 2011)

Flowing fluids are turbulent when the Reynolds number, $Re = \frac{V_o L_o}{\nu_o}$, exceeds

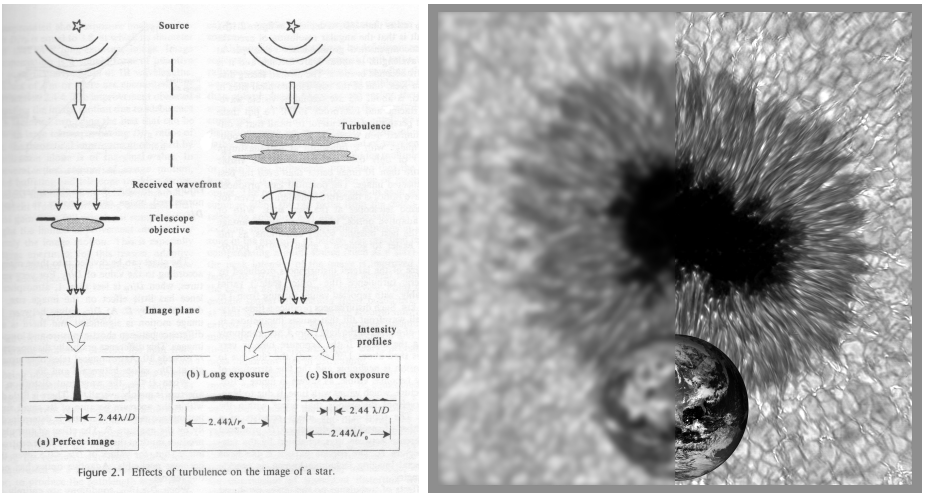

Fig. 1.9.— Left: (a) A perfect image, like a telescope in outer space might see. D is the telescope diameter. (b), (c) The effects of atmospheric turbulence are to blur the image. The term r_0 will be explained more fully in a moment. It describes the resolution of a telescope, when viewing through a turbulent atmosphere. Right: The left half of this image has been blurred to show the effects of atmospheric turbulence on a solar image. The right half shows the improvement gained via AO (from Hardy 1998; NSO/SP 2002).

some critical value. Where V_o is the characteristic velocity of the flow. L_o is the size of the blob of moving air. ν_o is the kinematic viscosity of the air, it is of order $15 \times 10^{-6} m^2\ s^{-2}$. The critical value of Re, for air, is of order 10^4. (e.g. Hardy 1998) (Rimmele, Private Communication (2011))

Atmospheric turbulence can be effectively described via the Kolmogorov model. Turbulence starts at some maximum size, the outer scale, $\mathcal{L}_0$. It then continuously breaks apart until a size scale is reached where the air is no longer turbulent, the inner scale ℓ_0. Finally, the inner scale is related to the outer scale by: $\ell_0 = \frac{\mathcal{L}_0}{Re^{3/4}}$. (e.g. Hardy 1998)

The 3D power spectrum of refractive index variations can be described by: $\Phi_N(\kappa) = 0.033 C_N^2 \kappa^{-11/3}$, for any one point in space. Where κ is the "spacial wave

number" ($2\pi/meters$). C_N^2 describes the strength of the turbulence.

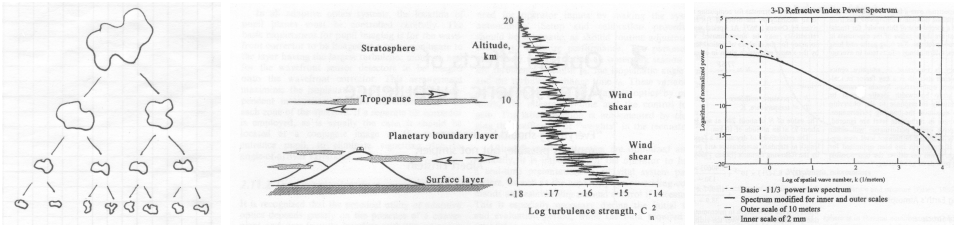

Fig. 1.10.— Left: A representation of Kolmogorov turbulence, showing moving blobs of air, breaking apart. Center: A graphical representation of turbulence strength, C_N^2. Note that it varies with height and wind speed. Right: The 3D power spectrum of refractive index variations, for any one point in space (from Hardy 1998).

To get the effect of the whole path that light travels through the atmosphere, we need to integrate. One important result is the Fried Parameter: $r_0 = \left[0.423k^2(\sec\zeta)\int_0^\infty dh\ C_N^2(h)\right]^{-3/5}$. Where k is the wave number of light, defined at 5000 Å. ζ is the zenith angle and h is defined as the path length through the atmosphere, integrated from the ground up. In basic terms, r_0 is the diameter, projected onto the telescope aperture, over which the wavefront varies by 5000 Å$/2\pi$, ie, the diameter of a diffraction limited telescope, given a certain amount of turbulence. (e.g. Hardy 1998) In normal terms, seeing with a Full-Width-Half-Maximum (FWHM) of $1''$ will have r_0 of 12cm, based on the FWHM of the Airy function of $1.03\lambda/D$. (O'Connel 2003)

1.2.1. How Does AO Work?

After a distorted wavefront enters a telescope, it passes into the AO system. Most astronomical AO systems operate in a so-called "Closed-Loop". This name comes from the fact that the Wavefront Sensor (WFS) is found behind the corrective optics (the Tip-Tilt Mirror (TTM), and the Deformable Mirror (DM)). In this

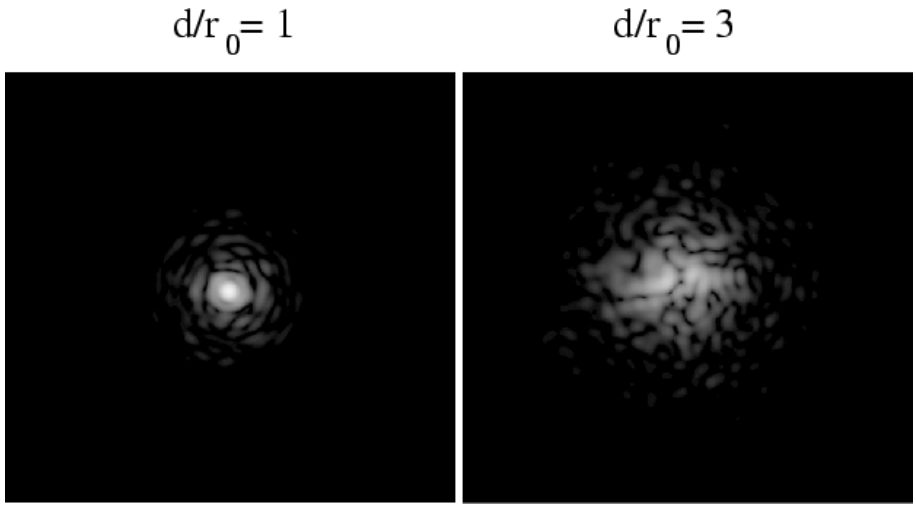

Fig. 1.11.— A representation of the ratio of a telescope's diameter to the Fried Parameter. When $r_0 = D$, the telescope is diffraction limited. When $r_0 < D$, the telescope is seeing limited (from Guyon 2002).

configuration, the AO system applies correction first (the initial iteration starts with a flat DM and centered TTM) and then measures the residual wavefront error. It then corrects for this residual and measures the wavefront again. In this way, the system can rapidly and accurately correct for wavefront errors. This is important, as the distorted wavefront changes appreciably, up to a few hundred times per second. (e.g. Hardy 1998; Roddier 1999; Tyson 2000, 2011)

A WFS measures the local slope of the incoming wavefront. There are several ways of doing this, but one of the simplest is the Shack-Hartmann WFS (SHWFS). A SHWFS operates by taking collimated light and focusing it into several small images. (For night-time astronomy, these images should be of a point-source.) Each of these images corresponds to the light coming through a small portion of the telescope aperture. In this way, the wavefront which enters the telescope is broken down into many small segments (the number of these depends upon many factors, which are not relevant here). The SHWFS then measures the local slope

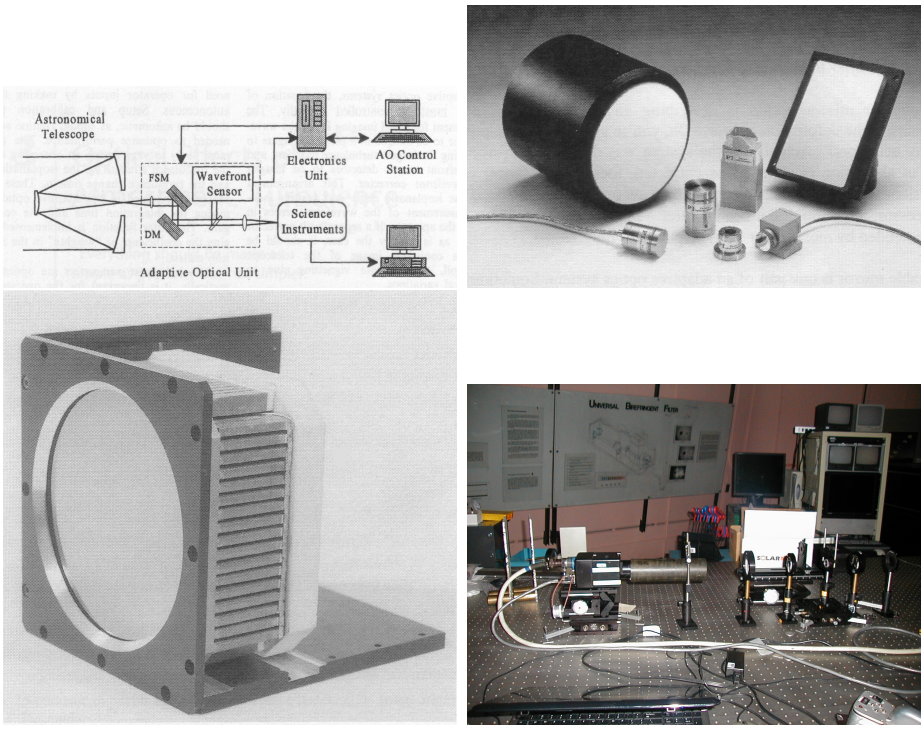

Fig. 1.12.— Left to Right: A closed-loop AO system schematic, a TTM (called a FSM, Fast Steering Mirror, in this illustration), a DM, and a WFS. (from Hardy 1998; Tyson 2000; Roddier 1999)

of the wavefront, in each subaperture. This information is sent to a computer, which reconstructs the wavefront. (e.g. Hardy 1998; Roddier 1999; Tyson 2000, 2011)

One efficient way of reconstructing the wavefront is by defining it in terms of a set of orthonormal polynomials. The Zernike polynomials are such a set. They are useful in that each polynomial represents a specific telescope aberration, such as astigmatism and coma. After a wavefront is measured, the reconstructor computes a series of coefficients, one for each Zernike polynomial. When the series is summed together, the output is a mathematical function that accurately describes the wavefront. This function is then used to apply the appropriate

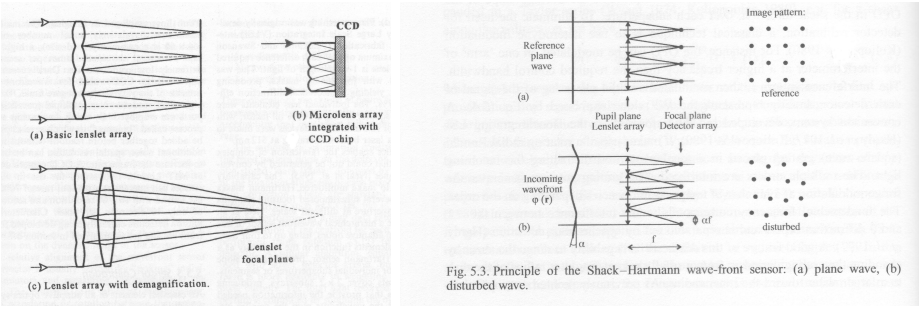

Fig. 1.13.— Left: The SHWFS breaks the incoming light into small sections, using an array of lenslets. Right: A representation of how the SHWFS measures the local slope of the wavefront.(from Hardy 1998; Roddier 1999)

correction to the TTM and the DM, in order to counter act the distortions in the wavefront and output a corrected wavefront to the science instrument. The reason that there is a separate TTM and DM is that the amplitude of Tip and Tilt corrections is much higher than that of higher order corrections. It is important to note that the degree to which the wavefront can be corrected depends upon the number of Zernike modes considered. However, there is a trade off between the number of modes which can be considered and the accuracy and speed with which the wavefront can be measured and reconstructed. (e.g. Hardy 1998; Roddier 1999; Tyson 2000, 2011)

DMs can be made in various configurations, some of which are shown below.

Solar AO systems can't use a point-source to measure the wavefront; an alternate technique must be used. The SHWFS, creates several images of detail on the solar disk. In order to measure the local tilts of the wavefront in each image, a cross-correlating algorithm is used. This algorithm measures the relative position of each image, with respect to some reference image. The resulting cross correlation functions, mimic the point-source images, used in night-time astronomy.

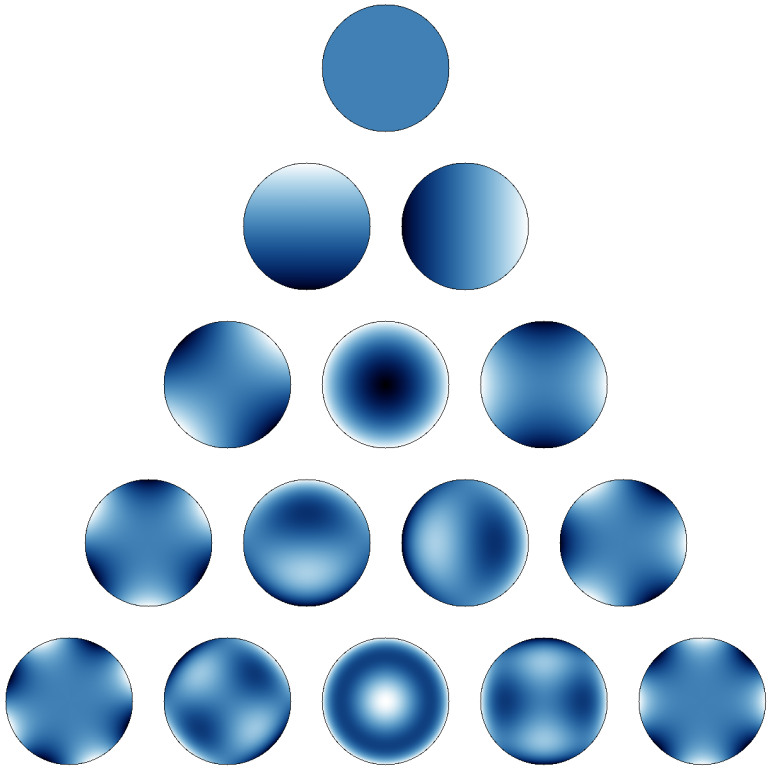

Fig. 1.14.— The first 15 Zernike Polynomials, starting with Z_1, "Piston".

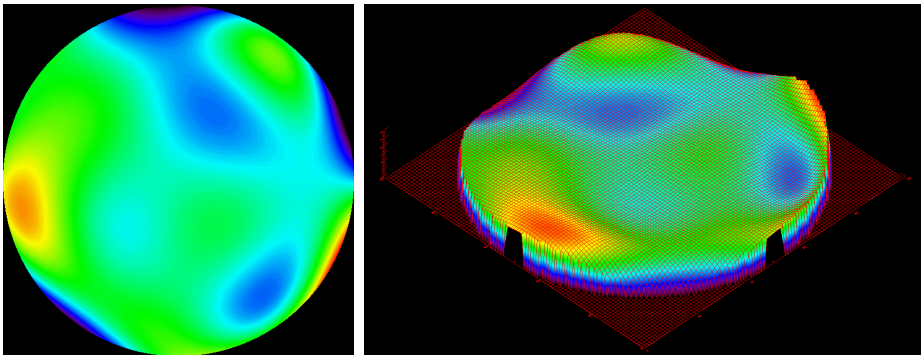

Fig. 1.15.— A reconstructed wavefront, based upon the first twenty Zernike polynomials, starting with Z_2.

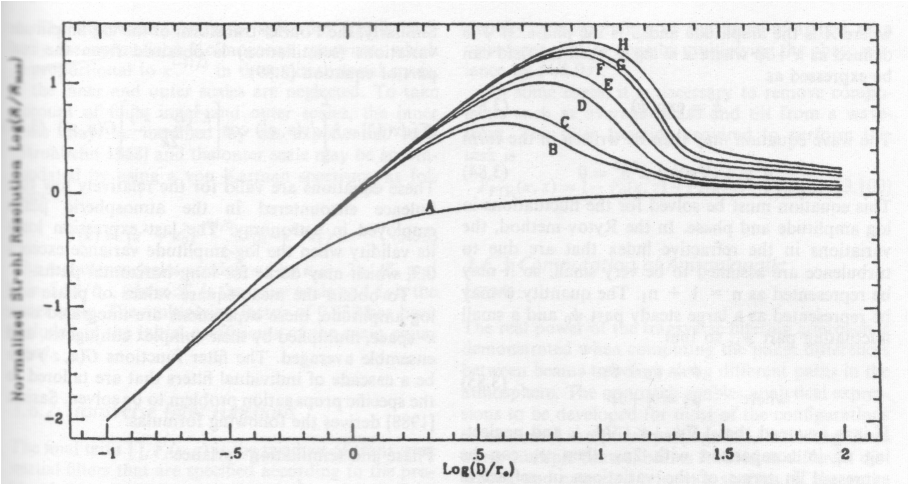

Fig. 1.16.— The degree of correction achievable by utilizing an increasing number of Zernike polynomials. The vertical axis is the logarithm of the normalized Strehl Ratio. It is normalized by dividing the measured Strehl Ratio, in a corrected image, by the Strehl Ratio of an uncorrected image, in the limit of $D >> r_0$. The Strehl Ratio is a measure of the peak intensity of the image of a point source, for an aberrated system, divided by the peak intensity of a perfect image. (A) An uncorrected image. (B) Corrected using Zernike polynomials up to Tip and Tilt, Z_3. (C) Corrected up to Defocus, Z_4. (D) Corrected up to Astigmatism, Z_6. (E) Corrected up to Coma, Z_8. (F) Corrected up to Trefoil, Z_{10}. (G) Corrected up to Spherical Aberration Z_{11}. (H) Corrected up to 5^{th} Order Astigmatism Z_{13}. Note that the maximum correction, for increasing number of modes, occurs at an ever higher ratio of D/r_0. (e.g. Hardy 1998)

1.3. Project Overview

My project will be to design and build an AO system which will be used to further our knowledge of solar prominences. I will explain this, in the following subsections.

1.3.1. The Need for Solar Limb AO

MacKay et al. (2010), outlined several open questions, two of which are relevant here:

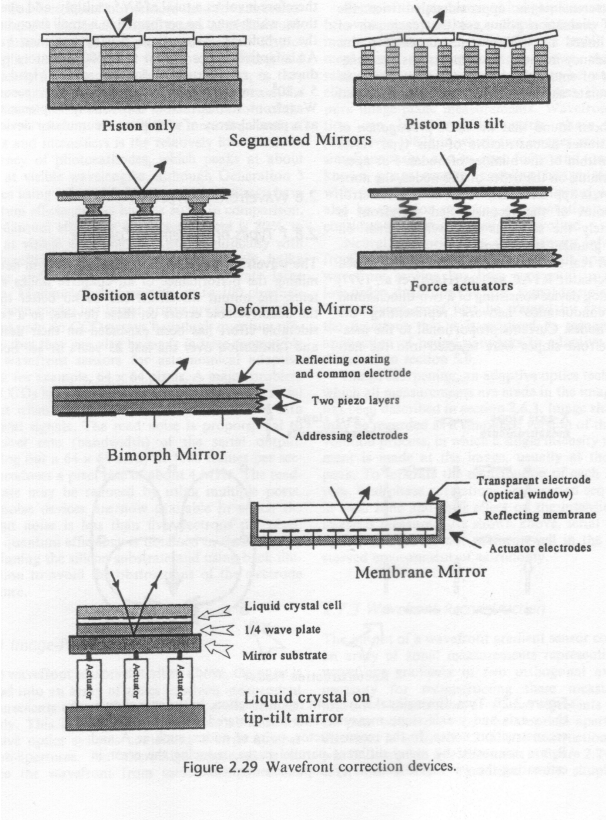

Fig. 1.17.— Various types of DMs. They are all designed to change the shape of the reflecting surface, in order to flatten the incoming wavefront. (e.g. Hardy 1998)

- Why do different Filaments and Prominences have such different morphologies?

- How does Prominence plasma collect and evolve?

Berger et al. (2010) identified one specific area that requires further study. They found that quiescent prominences appear to undergo what is known as Rayleigh-Taylor instability. This occurs when a fluid is suspended over another fluid of lower density. This imbalance can lead to plumes of the lighter material erupting through the denser material. The direction and strength of the magnetic

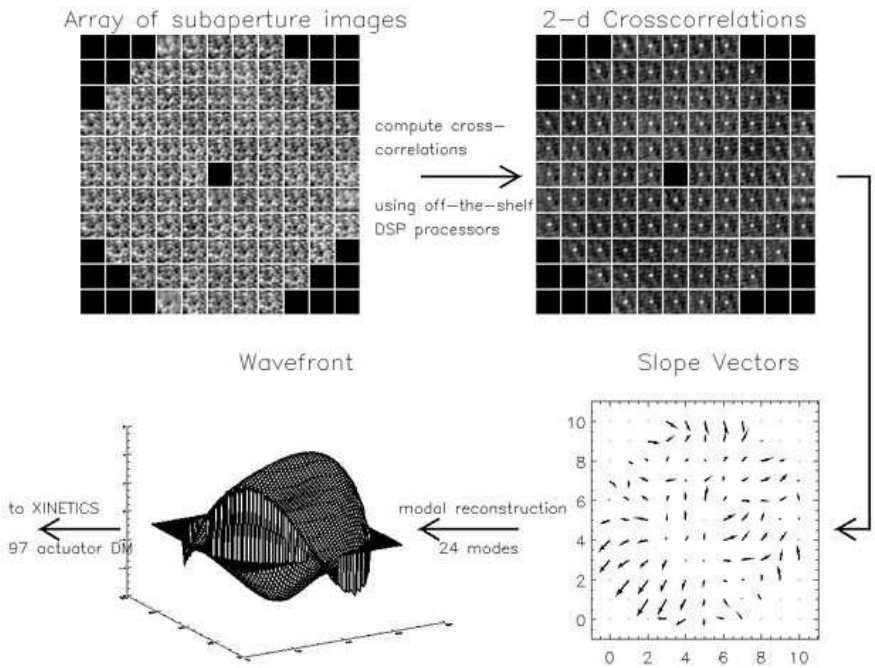

Fig. 1.18.— A representation of solar AO wavefront reconstruction, including the cross-correlation step(Rimmele & Radick 1998).

field in the prominence will affect the development of such instabilities. (see Berger et al. 2010)

Berger et al. (2010) propose that Rayleigh-Taylor instabilities are one way of replenishing the mass of quiescent prominences, which are constantly draining mass downward.

Space based imagers, such as the SOT on Hinode, can take images at high resolution, but they lack spectroscopic and polarimetric capabilities, necessary to understand prominence dynamics and their nature of the magnetic field which permeates them. Until now, such measurements have been made with ground-based telescopes, but at a resolution limited by the atmosphere. A solar limb AO system will allow us to do spectro-polarimetry at the same, or better resolution

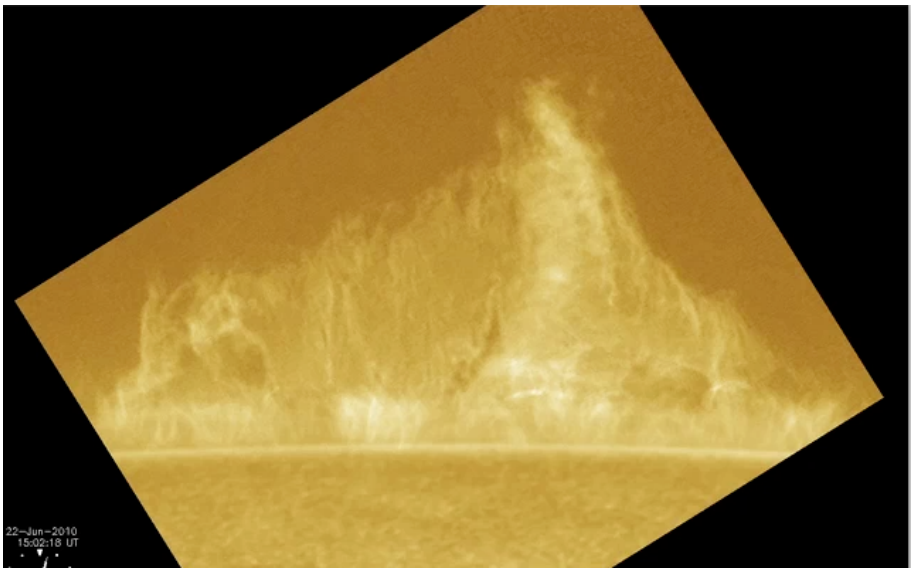

Fig. 1.19.— A CaIIK (3934 Å) image of a quiescent prominence, taken by the Hinode spacecraft. This image shows a great deal of intriguing detail, but lacks the detailed information that a spectro-polarimeter can provide, such as line of sight velocity, temperature, and magnetic field strength. (from Berger et al. 2011) (Rimmele, Private Communication (2011))

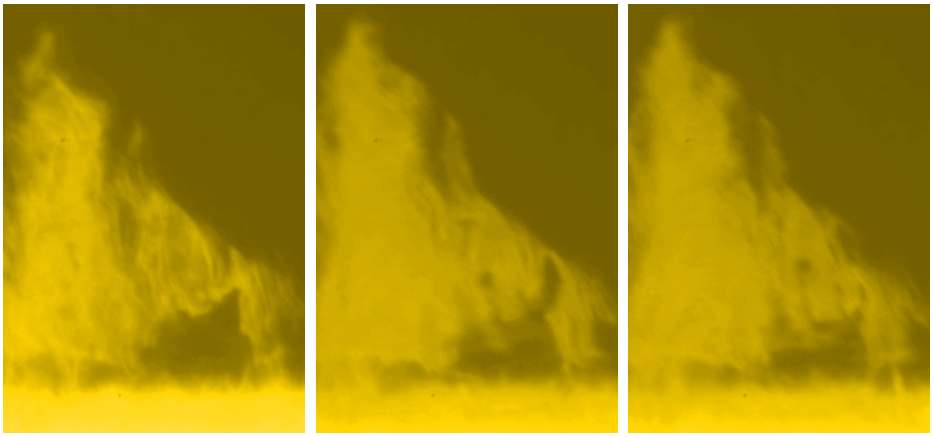

Fig. 1.20.— The development of a possible Rayleigh-Taylor instability. From left to right: A plume develops in a bubble of low-density plasma. The plume erupts through the prominence, leaving a track behind. (Hα (6563 Å) data from Hinode SOT *via* the Heliophysics Events Knowledge base Coverage Registry (HCR) http://www.lmsal.com/hek/hcr) using observation times within a few seconds of those quoted in Berger et al. (2011). (see also Berger et al. 2010)

as the images taken from a Hinode. We will also be able to acquire images at a resolution that rivals Hinode, with very high cadence. (Rimmele, Private Communication (2011))

Chen (2011) found that certain types of prominence oscillations may be the precursors to CMEs. A solar limb AO system will be able to measure these oscillations with precision, using high resolution, high cadence imaging, coupled with high resolution spectro-polarimetry. A capability which no other system, or spacecraft can match. (Rimmele, Private Communication (2011))

I intend to probe all of these questions, once the limb AO system is built. This system would be coupled with IBIS, a high cadence imager, capable of polarimetry, as well as two spectro-polarimeters, FIRS and SPINOR. (Rimmele, Private Communication (2011))

1.3.2. A New Type of Solar AO

At this point, the reader might ask:

"Why is Solar Limb AO so hard? Why hasn't anyone done this before?"

The main issue is photon flux. The required 0.5 - 0.7 Å filter bandwidth transmits very little flux. This makes it extremely difficult to measure the wavefront. (Rimmele, Private Communication (2011))

We will probably need to use all available Hα light, for the WFS. (A standard, solar AO system uses only part of the light for the WFS.) This means that we will need to use a dichroic beam splitter, and feed near IR light to IBIS or one of the spectro-polarimeters. (We would observe the Ca II 8542 Å line, for example.)

(Rimmele, Private Communication (2011))

When we are able to measure the wavefront, using faint solar prominence detail, an entire AO system will need to be designed and optimized, to utilize these measurements. It is not possible to simply put a new WFS on an existing AO system. (Rimmele, Private Communication (2011))

The difficulty of measuring the wavefront, coupled with the need to design an entirely new AO system, is the reason why we are the first to build a solar limb AO system.

2. SHACK HARTMANN WAVEFRONT SENSOR

2.1. SHWFS Setup

A lenslet array was employed to divide the incoming light beam into 21 subapertures. The Shack-Hartmann samples the pupil of the 76 cm Dunn Solar Telescope with 5 subapertures across the telescope diameter yielding a subaperture size of 15 cm. This is twice the subaperture size of the DST high order AO system used for on disk observations and was chosen to obtain sufficient photon flux on the wavefront sensor. A Zeiss 0.5 Å Hα filter was used for the imaging of prominences. Due to the low transmission of the Zeiss filter the exposure time had to be set to 20 ms in order to obtain sufficient signal-to-noise on the Dalsa D7 wavefront sensor detector (Datasheet 1999). The subapertures were imaged at an image scale of 0.6 arcseconds per pixel. We note that a 20 ms exposure time is too long for real time AO that is expected to correct atmospheric seeing. A 0.5 Å Hα high transmission interference filter has been ordered to alleviate this problem.

A series of frames was taken for each of several solar prominences. In order to measure image motion for each subaperture image, a reference subaperture was chosen from the first frame of each series. Cross correlations were performed for each subaperture image, for every frame, to detect image motion in each subaperture, relative to the reference image (see Rimmele & Marino 2011). A representation of this process is shown in Figure 2.1.

2.2. Shack-Hartman Results

Wavefronts were estimated for each frame, in terms of Zernike coefficients. The temporal variance of each Zernike coefficient was compared with the theo-

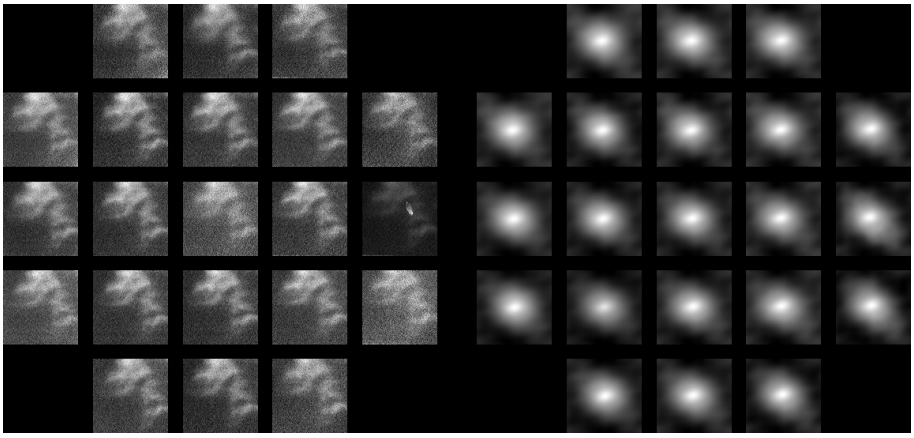

Fig. 2.1.— Lenslet images (left) and their associated cross correlation plots (right). The images from each subaperture represent image information taken from the corresponding portion of the full telescope aperture. Bright points in the cross correlation plots represent the position of the image within each subaperture.

retical expectation, given Kolmogorov Turbulence (Noll 1976). This is shown in Figure 2.2. The expected values were scaled by minimizing the difference between the first five modes (the least noisy) of the measured variance curve with those of the expected value curve.

This WFS seems to be able to adequately measure the incoming wavefront up to about 15 Zernike modes, using the light from solar prominences. To our knowledge, this is the first time that this has been accomplished. In order to measure more modes, we would have to divide the telescope pupil into more subapertures (e.g. Hardy 1998; Roddier 1999; Tyson 2000, 2011). However, as we've already stated, the amount of Hα flux available from a solar prominence is very limited.

Judging from these initial experiments the Shack-Hartmann prominence wavefront sensor appears to be a viable approach for Solar Limb AO, provided that exposure times can be reduced significantly.

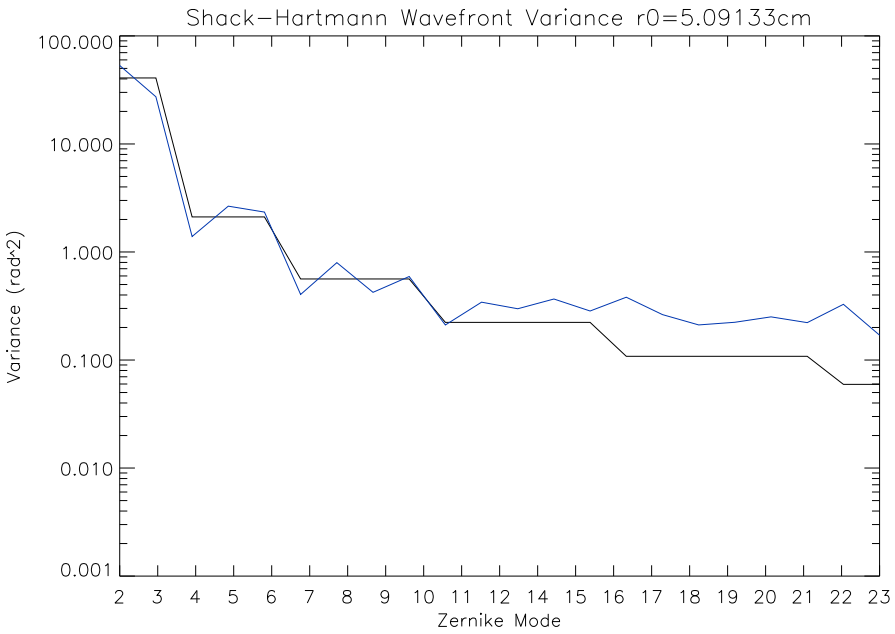

Fig. 2.2.— Temporal Variance of Zernike terms (blue) compared with the expected value (black), given the value of the Fried parameter, r0, shown in the graph title (e.g. Hardy 1998; Roddier 1999; Tyson 2000, 2011) (see also Noll 1976). The Temporal Variance was calculated for 100 frames, for the pointing shown in Figure 2.1. The Zernike terms are labeled, starting with Tip and Tilt, Z_2 and Z_3. The measured variances follow the expected ones for Zernike terms up to Z_{16}.

With the flux level predicted from a photometric analysis (see Appendix B), assuming a camera gain of 20 (a quantity that we estimated for our own Dalsa camera) and a nominal sensitivity of 27% at 6563Å (Datasheet 1999), we expect raw counts from 145 to 1035 per *millisecond*, which could allow for operation at 1 kHz. Our PD setup would only achieve 15 to 105 counts ms^{-1}.

Table 2.1. Initial SHWFS Setups

Filter Manufacturer	Setup 1 Zeiss	Setup 2 Coronado
Filter FWHM	0.5 Å	0.7 Å
Lenslet Pitch	400μm	400μm
Lenslet Focal Length	3.2mm	3.2mm
Number of Subapertures	5X5	7X7
Subaperture FOV (see Schmidt et al. 2010)	66″	84″
Camera	12 μm Pixels	12 μm Pixels
Camera Binning	1X1	2X2
Telescope Image Scale	7.42″mm^{-1}	7.42″mm^{-1}
Re-imaging Optics + Lenslet Magnification	0.1472	0.0569
Final Image Scale	0.605″ per Pixel	3.20″ per Pixel

2.3. Predicted Performance

As we stated in Section 1.1.1 there is very little light available for our SHWFS. Indeed, there is so little flux available, even in Hα light, that we are using a custom made Hα filter with very high transmission, see Figure 2.3 and Appendix B. This same type of filter will be used on the Visible Broadband Imager, on the ATST.(Rimmele et al. 2014)

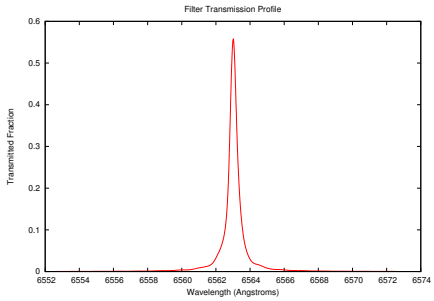

Fig. 2.3.— Filter transmission profile of our custom Hα filter.

Using our high transmission filter, we still are photon starved, thus it is necessary to make trade-offs in our design parameters. If we sample the wavefront finely, by dividing the SHWFS field of view into many subapertures, we lose a great deal of light and can no longer sense the wavefront. So, we use fewer subapertures for our SHWFS than for the SHWFS used for on-disk observation at the DST.(Rimmele & Radick 1998) We also need a large field of view per subaperture, to allow for the tracking of solar prominence features that are large in comparison to those seen on the disk, as we have directly discovered.(Taylor et al. 2012) Finally, the final pixel scale of the subaperture images must be chosen to balance resolution and image brightness.(Michau et al. 1993) The number of subapertures used, their FOV, and the final pixel scale are can be determined

analytically, as well as directly measured. (Scharmer et al. 2003) To verify that off-limb solar AO is possible and practical, we modeled the performance of a particularly promising SHWFS configuration.

2.3.1. WFS Noise From Indirect Methods

It is necessary to measure the noise created by the SHWFS and to estimate noise from the various other sources that are present in a finished AO system, in order to predict the ultimate performance of an Off-Limb AO system.(Hardy 1998)

I performed various tests with several different WFS configurations and cameras. (See Appendix 7.3 for more details.) The only camera we had in-house that could run at sufficient speed was the Dalsa D6.

A SHWFS was setup with a 5X5 array of subapertures (See Figure 2.4.), each with a Field of View (FOV) of 40" and an image scale of 0.86" per pixel. We measured the image scale and FOV using a resolution target. Several series of 2000 frames were taken. These were taken at frame rates of 100, 200, 300, 400, 500, 600, 750, 850, and 950 Hz. The exposure time for this camera is roughly equal to the inverse of the frame rate, as the readout is very fast.

The functional form for noise generated by a Correlating SHWFS is given by Rimmele & Marino (2011). However this function was explicitly stated to be for Nyquist sampling, which our system can't attain, due to low light levels. Michau et al. (1993) give a more complete version of this formula:

$$\sigma_x^2 = \frac{5m^2\sigma_b^2}{n_r^2\sigma_i^2}\frac{(dp)^2}{(f\lambda)^2}(\text{waves}^2), \tag{2.1}$$

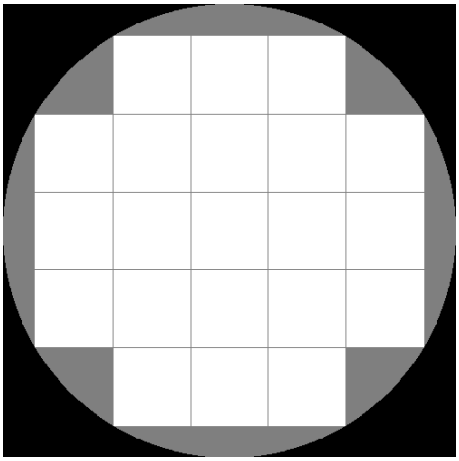

Fig. 2.4.— The pupil layout for the 5X5 grid. The outer circle is the telescope pupil, 76.2cm in diameter.

where σ_x^2 is the total noise and m is the Full-Width-Half-Maximum (FWHM) of the Cross-Correlation (CC) peak, from the subaperture images (See Figure 2.5.). σ_b^2 is the detector noise, which we assume to be read-noise plus photon noise. We measured the read noise to be approximately 68 electrons per pixel. The Photon noise was assumed to be Poisson noise: $\sigma^2_{\rm Photon} = g\bar{S}_{\rm ADU}$. Where g is the camera gain and $\bar{S}_{\rm ADU}$ is the average pixel value, in ADUs.(Barry & Burnell 2000) $n_r^2\sigma_i^2$ is the energy content of the image, d is the subaperture size, p is physical the size of the pixels, f is the effective focal length of the optical system (telescope plus bench optics), and λ is the wavelength at which the measurements are made, 6563 Å. Note that:

$$\frac{(dp)^2}{(f\lambda)^2} \approx \frac{(d\theta)^2}{(\lambda)^2}, \tag{2.2}$$

where θ is the image scale, in radians per pixel. d is 13.07cm. (See fig 2.4.)

To measure m, we used the CC peaks for the 5X5 array.(Rimmele & Marino 2011) Following the method of Michau et al. (1993), we fit a 2D Gaussian function to the central portion of each CC peak. m is the average FWHM of all the CC

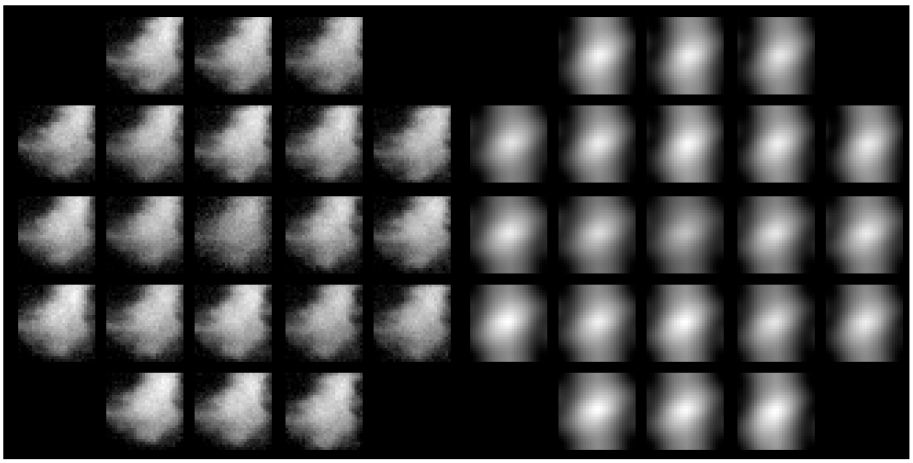

Fig. 2.5.— SHWFS images, using the Dalsa Falcon VGA300 HG. On the left are Prominence images which have been dark-subtracted and flat-fielded. On the right are the Cross-Correlation peaks.

peaks.The detector noise is again denoted as σ_b.

The energy of the image is:

$$n_r^2 \sigma_i^2 = \sum_j |S_j - \bar{S}|^2, \tag{2.3}$$

where S_j and $\bar{S}$ are the signal per pixel and the average pixel value, measured in electrons.(Michau et al. 1993)

I calculated the result of Equation 2.1, for each of the 2000 frames, at each exposure time, and then averaged over those 2000 frames. To create a smooth curve, I noted that Michau et al. (1993) use an approximation for an image of a given contrast, using our notation:

$$\sigma_x^2 \approx \frac{5m^2\sigma_b^2}{n_r^2 C g \bar{S}_{\rm ADU}} \frac{(d\theta)^2}{(\lambda)^2} (\text{waves}^2), \tag{2.4}$$

Where C is a factor related to the image contrast and n_r^2 is the pixel area of each subaperture image. C is found by dividing Equation 2.1 by Equation 2.4. Thus:

$$C = \frac{\sigma_i^2}{g\bar{S}_{\mathrm{ADU}}}, \tag{2.5}$$

I then plotted the results, scaling σ_i and σ_{Photon} with exposure time. Having done so, I multiplied each data point by 1.5, in order to account for anisoplanatism in each subaperture, as stated by Rimmele & Marino (2011). Figure 2.6 shows the calculated noise values, fitted with the smoothed curve, given by Equation 2.4. The error bars are 1 standard deviation of the noise calculated from each series of 2000 frames.

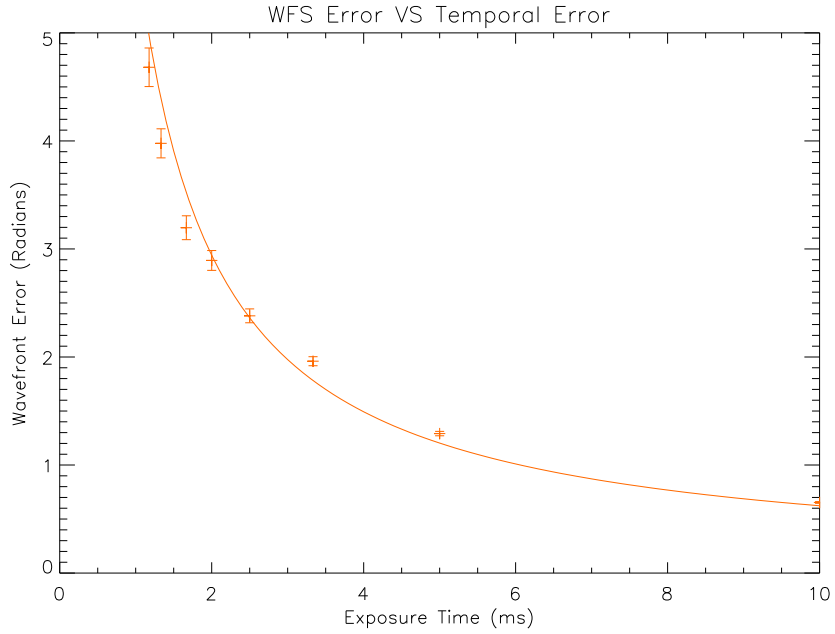

Fig. 2.6.— Sensor noise measurements obtained from the Dalsa D6. Points calculated from Equation 2.1 were fitted to Equation 2.4.

Because the noise levels were so high in Figure 2.6, a superior camera was needed, so I selected a Dalsa Falcon VGA300 HG, due to its high sensitivity, moderate read-noise, high speed, and low cost, coupled with one of our in-house lenslet arrays, to make the SHWFS. To achieve the required speed, we only read-

out a small portion of the camera chip (160X160 pixels). Figure 2.7 shows the relative improvement between the the D6 and the Falcon VGA300.

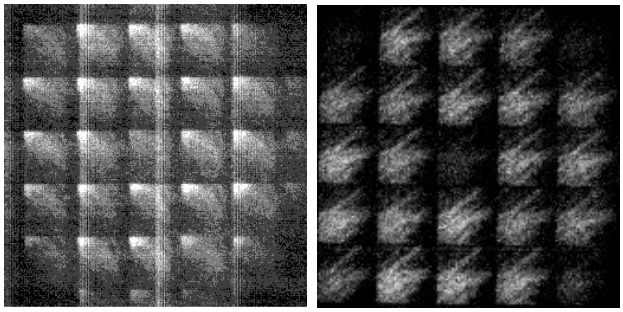

Fig. 2.7.— SHWFS Image quality comparison. Left: A single raw frame on a moderately bright prominence from the Dalsa D6. The exposure time was slightly longer than 1ms. Right: A single raw frame from the Dalsa Falcon VGA300. The exposure time was 900 μs. The left image is read-noise dominated, the right is dominated by shot-noise.

A new SHWFS was setup with a 5X5 array of subapertures, each with an FOV of 30" and an image scale of 0.82" per pixel. The smaller FOV was used in order to allow the camera to run at the requisite speed. I only read out 160X160 pixels. The same procedure was repeated from above, except only one exposure time was used, as I was fairly confident in the functional form from Equation 2.4. I ran this camera with a frame rate of 900Hz and exposure times of 900μs. The results will be shown in Figure 2.9, below.

2.3.2. WFS Error from Telemetry

In order to verify the above error measurements, I found the error in our SHWFS by direct measurement from SHWFS telemetry. We did this by taking the power spectrum of the total pixel shifts, as measured, that is: shift = $\sqrt{x_{\text{shift}}^2 + y_{\text{shift}}^2}$. The power spectrum should be taken for data with a zero mean, as stated by Marino.(Marino 2007) So we subtracted the average shift from each

member of the shift array, for each data set.

Using the method of Marino(Marino 2007), assuming white noise:

$$\sigma^2_{\mathrm{WFS}} = \sum_{1}^{N} \text{Noise Level.} \tag{2.6}$$

Where the noise level is the point where the power spectrum becomes flat and N is the total number of exposures in each time series (see Figure 2.8).

This becomes:

$$\sigma^2_{\mathrm{WFS}} = \text{Noise Level} * N \tag{2.7}$$

This yields the noise variance, in terms of pixels^2. To find the RMS noise in terms of nanometers, we apply the following:

$$\sigma_{\mathrm{WFS\ nm}} = \sigma_{\mathrm{WFS}} * \theta * d/(3600 * 57.3) \tag{2.8}$$

Where θ is the pixel scale, here 0.82" per pixel, and d is the subaperture diameter, 13.07 cm.

To find the error in radians:

$$\sigma_{\mathrm{WFS\ rad}} = 2\pi\sigma_{\mathrm{WFS\ nm}}/\lambda, \tag{2.9}$$

with λ being 6563 Å. we found the ratio between $\sigma_{\mathrm{WFS\ rad}}$ and σ_x, as found in Section 2.3.1, for each frame rate where $\sigma_{\mathrm{WFS\ rad}}$ was defined. We then scaled σ_x by the average of these ratios, for each prominence. We then fit Equation 2.4,

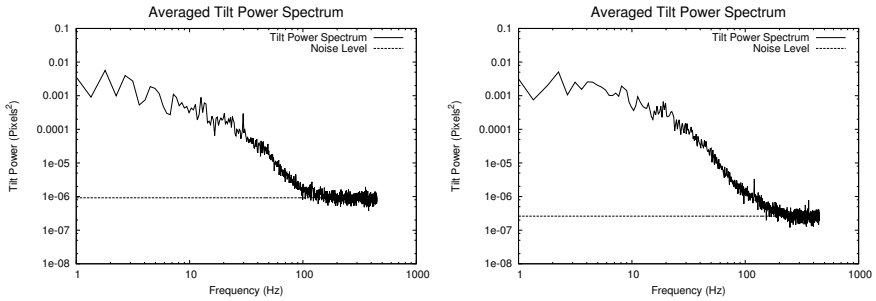

Fig. 2.8.— Left: Noise Power Spectrum for data taken at 900 Hz, for a moderate contrast prominence. Right: Noise Power Spectrum for data taken at 900 Hz, for a high contrast prominence.

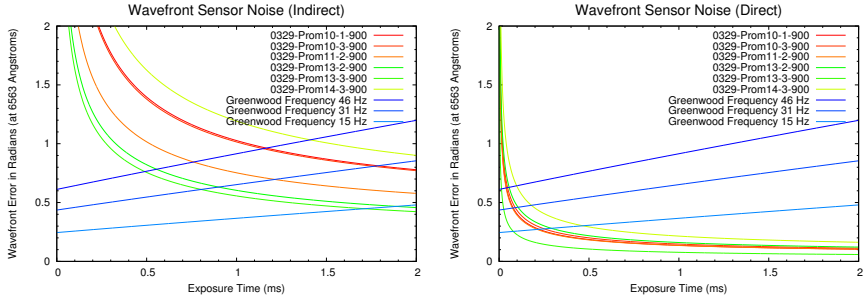

Fig. 2.9.— Left: The solid red to green lines represent the WFS noise for the various prominences which we observed. This is without the factor of 1.5 quoted in Section 2.3.1. The time delay errors, blue, are for 10cm seeing (at 5000 Å, 13.8 cm at 6563 Å, for which these errors are measured), with wind speeds of 5, 10, and 15 m/s, from bottom to top, respectively. These correspond to Greenwood frequencies of 15Hz, 31Hz, and 46Hz, again at Hα. See Section 2.3.3 for an explanation of time-delay error. Right: Noise calculated from telemetry data.

to the scaled σ_x, as shown in Figure 2.9 (We also show error due to the finite at which a SHWFS can measure the wavefront, which we explain in Section 2.3.3). Comparing the result from Equation 2.1 with our telemetry measurement, we find that Equation 2.1 overestimates the noise by about a factor of 4. This confirms the result found by Michau (2002).

Figures 2.9 show the importance of balancing the speed of the wavefront

measurements, the shorter the exposures, and thus the faster the wavefront measurements, the lower the noise from the atmosphere, but the higher the noise from the SHWFS its self. We will show how this impacts the quality of the final image in Section 2.3.3.

2.3.3. Strehl Ratio

The quality of an image is often measured in terms of its Strehl Ratio. The Strehl Ratio is the measure of the intensity of the peak of a point source image of an imperfect optical system, vs the intensity of that same object, as measured by a perfect optical system. A perfect optical system will have a Strehl Ratio of 1. Any imperfection in the optics or caused by atmospheric distortion will lower the Strehl ratio.(Born & Wolf 1999; Hardy 1998) A Strehl Ratio above 0.8 is considered diffraction-limited.(Born & Wolf 1999) However, an image still contains all of the information of a diffraction-limited one, only at a lower signal-to-noise ratio, until the Strehl ratio drops below about 0.1.(Hardy 1998)

In order to determine the Strehl Ratio that we expect to achieve from an AO system, using this SHWFS, we need to account for the other primary sources of error: Time Delay, Fitting and Aliasing errors. For all of the following error estimates, we assume a Fried Parameter, r_0, of 10cm, at 5000 Å. (See Hardy(Hardy 1998) for a more detailed discussion of AO error sources.)

To determine the error due to time delay, we used the functional form quoted by Hardy(Hardy 1998):

$$\sigma^2_{\mathrm{TD}} = 28.4(\tau_s f_g)^{5/3}, \tag{2.10}$$

where τ_s is the time delay and f_g is the Greenwood frequency and $f_g \approx 0.427\frac{v}{r_0}$,

for a single layer atmosphere model, which we assumed for this study, v being the wind speed.(Hardy 1998) This error only takes the speed of the camera into account.

To find τ_s, we assumed a delay equal to the exposure time, to get the data from the camera, plus a constant, pessimistic 500 micro second delay, for wavefront reconstruction plus the camera readout, etc. This yields $\tau_s = 500\mu\text{s} + \text{exposuretime}$. This is similar to the method used by Hardy.(Hardy 1998) We calculated three curves for r_0 of 10cm, at 5000 Å, which is 13.8cm, at 6563 Å, using the formula $r_0' = r_0(\lambda/5000)^{6/5}$.(Hardy 1998) we chose wind speeds of 5, 10, and 15m/s. Thus, our Greenwood frequencies were 15Hz, 31Hz, and 46Hz (See Fig. 2.9).

We used the forms of Fitting and Aliasing errors, as described by Rimmele and Marino,(Rimmele & Marino 2011) where the fitting error is:

$$\sigma_F^2 = 0.28\left(\frac{d}{r_0}\right)^{5/3}. \tag{2.11}$$

The aliasing error is:

$$\sigma_A^2 = 0.08\left(\frac{d}{r_0}\right)^{5/3}, \tag{2.12}$$

where d is the subaperture size.

In Figure 2.10, we show the resultant Strehl ratios that we expect, given the above errors. We used the approximation, SR $= e^{-\sum_i \sigma_i^2}$,(Hardy 1998) to find these Strehl ratios. All of the Strehl ratios were calculated at 8542 Å. To convert the SHWFS and Time Delay errors, which were measured in radians, at 6563 Å, we took note that 1 wave $= 2\pi$ radians, at a given wavelength, so:

$$\sigma_{8542 \text{ in radians}} = \frac{6563}{8542}\sigma_{6563 \text{ in radians}}. \tag{2.13}$$

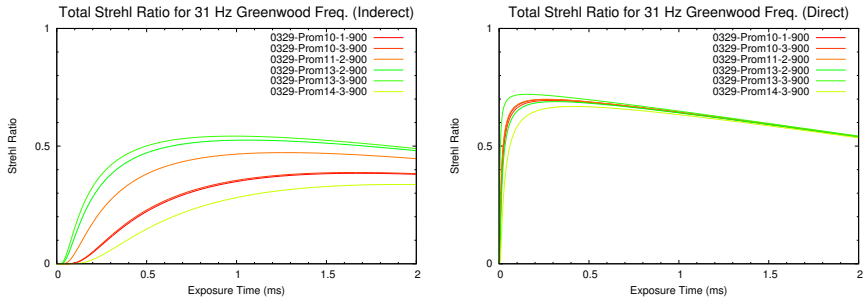

Fig. 2.10.— Left: Calculated Strehl ratio, taking into account all error sources. Only the curves for a Greenwood Frequency of 31Hz are shown. Right: Calculated Strehl ratio from telemetry data. These data are for 8542Å.

Figure 2.10 shows that we expect to have Strehl ratios of between 0.6 and 0.7, at 8542 Å, given a Fried parameter of 10cm and 10m/s wind.

There are a few important facts that can be gleaned from Figure 2.10. One: The faster the SHWFS is able to measure the wavefront, the better the achieved Strehl Ratio. Two: Using faint, low contrast prominences for sensing the wavefront lowers the maximum achievable Strehl Ratio. Three: For a fainter prominence, the maximum achievable Strehl Ratio occurs at a slightly slower frame-rate than for a brighter prominence. Four: We are limited by hardware to a speed of around 900Hz, which corresponds to an exposure time of about $900\mu s$. If we had a faster camera, we could achieve slightly better Strehl Ratios, but the achievable Strehl Ratio decreases slowly, to the right of its maximum point.

3. SYSTEM INTEGRATION

3.1. Bench Tests

The Off-Limb AO SHWFS was setup on a laboratory bench, in the NSO machine shop building. It utilizes a 97 actuator, Xinetics Deformable Mirror (DM). In these bench tests, the TTM was not used due to the lack of a suitable spare from the DST. Wavefront reconstruction is accomplished via the Kiepenheuer-Institute Adaptive Optics System (KAOS), which was originally coded for the German VTT telescope and was rewritten to operate the GREGOR telescope.(Berkefeld et al. 2012) We are running KAOS on an off-the-shelf computer, utilizing an Intel i7, quad-core processor. This is interfaced to the DM using a Xinetics, Gen III chassis, driving 144 channels. 97 channels are used for the DM, 2 for the TTM, and the remaining channels are unused.

Figure 3.1 shows the KAOS Graphical User Interface (GUI). The GUI contains all of the necessary controls for running the KAOS system. These include test and calibration functions, as well as the control functions for the AO system. It also includes displays which show the SHWFS subaperture images and the Cross Correlation functions. It also includes displays of the TTM and DM actuator commands.

The bench setup is shown in Figure 3.2. A laser with dual fiber-optic outputs was used to simulate pinhole images which are used to calibrate AO systems on the DST. Both fibers have an f/6 exit cone. The beam from one fiber was collimated with a lens having a focal length of 1051.56mm. This collimated beam is reflected off the DM to a Jagers doubled of focal length 1400mm. This beam is recollimated with a 225mm lens, forming a pupil diameter of 12.375mm. This

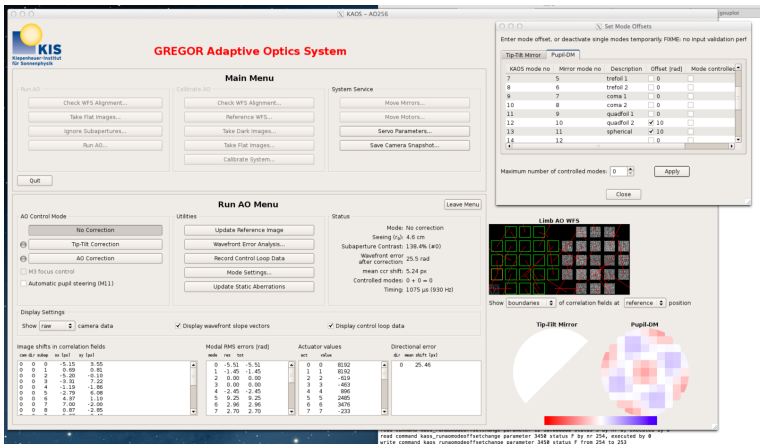

Fig. 3.1.— The GUI display for the KAOS system, as explained int eh text. It includes all of the necessary functions for operating an AO system.

is re-focused via a 600mm lens, which is reflected off of a flat mirror and passes through a 50/50 beam splitter. Half of the beam passes to an interferometer, as will be discussed below, the other half is bent 90 degrees and continues on to the SHWFS. After being dimmed by neutral density filters, the beam is collimated by a 100mm lens. This collimated beam is focused by a lenslet with a 400μm pitch and 9mm focal length. This is reimaged with a 300mm and 130mm lens, yielding a 5X5 Shack-Hartmann array, with 34 pixels per subaperture. This is very close to the 5X5 SHWFS setup as used on the DST, which has 32 pixels per subaperture and 0.82″ per pixel.

A second SHWFS setup was also tested, The final 100mm, 200mm, and 130mm lenses were replaced by 150mm, 200mm, and 100mm, lenses. The lenslet was replaced by one of the same pitch, but with a 12mm focal length. This created a 7X7 Shack-Hartmann array, which would simulate an image scale of about 1″ per pixel and subaperture size of about 24 pixels.

The second laser fiber feeds an interferometer. It was added to verify the

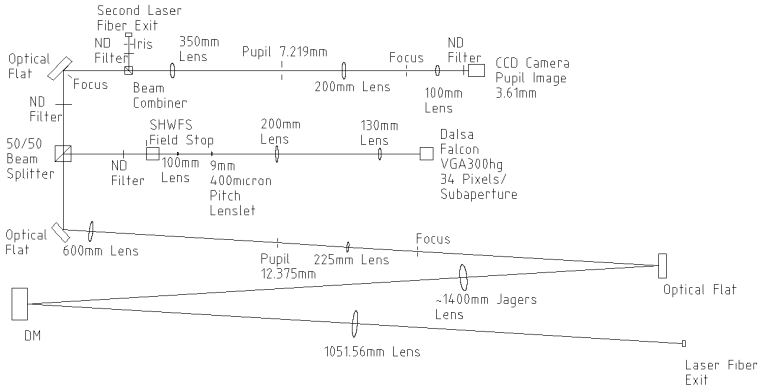

Fig. 3.2.— CAD drawing of the optical bench test setup. This is the setup used for the 5X5 SHWFS.

flatness of the DM. This was done because early, unsuccessful tests showed that DM to be very far from flat. The remaining 50% of the initial laser beam interferes with the light coming from the second laser fiber. This interference image is focused onto a CCD camera, using 350mm, 200mm, and 100mm lenses. With the information provided by the interferometer, much of the unflatness of the DM could be corrected. Figure 3.3 shows the results of the flattening of the DM. The left image shows many optical distortions as shown by the almost spaghetti-like shape of the fringes shown. The right hand image shows fringes which are much closer to the ideal of perfectly straight vertical bars, which would indicate a perfectly flat optical surface. This flattening was accomplished by using old data for this DM, as was taken in 2010. These data contain the actuator commands required to flatten the mirror, as used by the AO-76 system on the DST.(Ren et al. 2003) These commands were converted to a format that KAOS could understand and applied to the DM. As DMs change with time, the commands did not perfectly

flatten the mirror. The commands were manually adjusted slightly to make the DM flatter. KAOS could then do the rest of the work required to fully flatten the mirror.

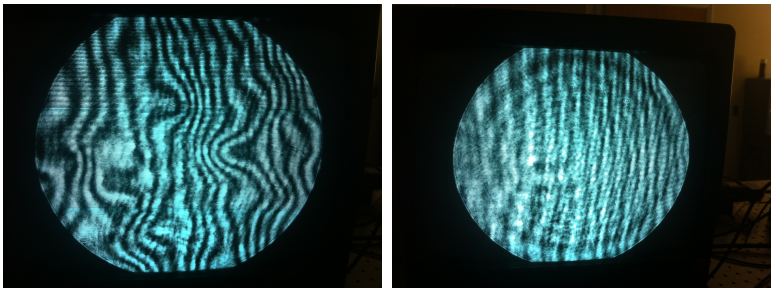

Fig. 3.3.— Left: The interferometer display of the non-flat DM. Right: DM after flattening. Though not perfect, represents a significant improvement.

An artificial heat source was placed in the collimated beam, just in front of the DM. This was done to simulate turbulence in the atmosphere. The lack of a Tip-Tilt Mirror (TTM) was a sever handicap to these tests. it turned out that KAOS could not apply sufficient correction to the DM alone, in order to counteract the Tip-Tilt aberrations caused by the heat source. Even so, improvement was noted. Figure 3.4 shows the improvement in image quality after the AO loop was closed. The red line in Figure 3.4 shows the total wavefront error, as calculated by KAOS, which would be present, were no correction applied. The blue line shows the residual wavefront error, as measured by KAOS, after the correction was applied. The exact numbers here are not as relevant as the overall percentage of improvement, since a Tip-Tilt mirror was not present and the exact pixel scale on the wavefront sensor was unclear.

A second test was performed to verify that the correct commands were being sent to the DM. A plate that produced a fixed amount of astigmatism was inserted into the collimated beam. This plate was rotated to produce varying degrees of

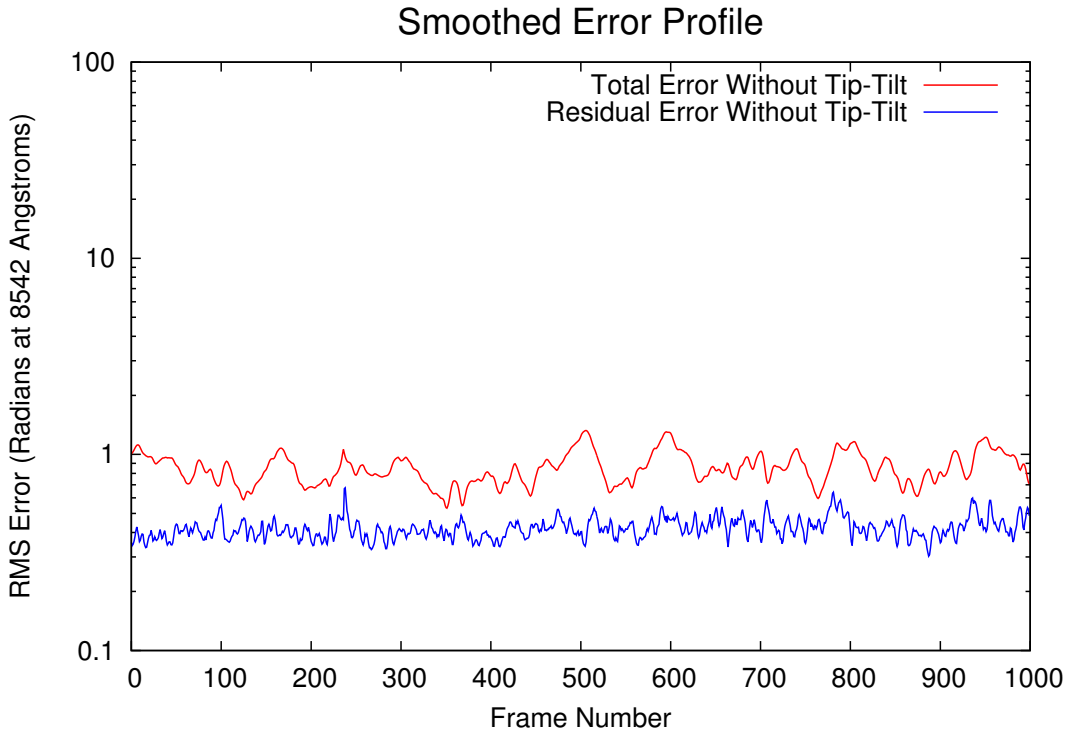

Fig. 3.4.— Total and residual wavefront errors with the Tip-Tilt removed. The Tip-Tilt was removed due to the lack of a TTM. The method by which these errors were measured is more fully explained in 3.2.1

astigmatism. The interferometer verified that KAOS was indeed giving the correct commands to the DM, in order to correct for this astigmatism.

Once it was evident that KAOS would perform as expected, tests on the DST were commenced.

3.2. Tests at the Dunn Solar Telescope

The following was reported by Taylor et al. (2013). The Off-Limb AO SHWFS, as tested in Section 2.3 was integrated into the DST AO bench. Tests were performed on Port 2 of the DST. The setup consists of a beam-splitter, which diverts 95% of the incoming Hα light to the SHWFS, leaving the remainder to feed the imaging camera. The rest is fed to the SHWFS. The bench optics shown are required to create a 5X5 SHWFS array with subaperture FOV of 30" and pixel scale of 0.82" per pixel. (See Figure 3.5) For these tests, the camera was run at a frame rate of 860Hz. This is slightly slower that the model frame rate, but it allowed for a border of a few pixels around the subaperture images. (The camera is now reading out 174X174 pixels.) This allows the KAOS system to compensate for slight misalignments in the optical system. Since we were running at a slightly slower frame rate, we used exposure times of 1ms in these tests. This lowered the noise coming from the SHWFS, at the expense of slightly more time-delay error.

3.2.1. Procedure

The KAOS system is capable of recording data which contains raw measurements from the SHWFS as well as the calculated errors in the reconstructed wavefront. KAOS records the commands sent to the TTM and the DM. It calculates the total atmospheric error in each mode, given the residual error and the commands sent to the DM. These data and their caveats are explained below:

When KAOS reconstructs the wavefront, it does so by utilizing Karhunen-Loève (K-L) modes.(Noll 1976; Dai 1995) The degree of correction that can be achieved depends upon the number of modes that can be utilized, which in turn

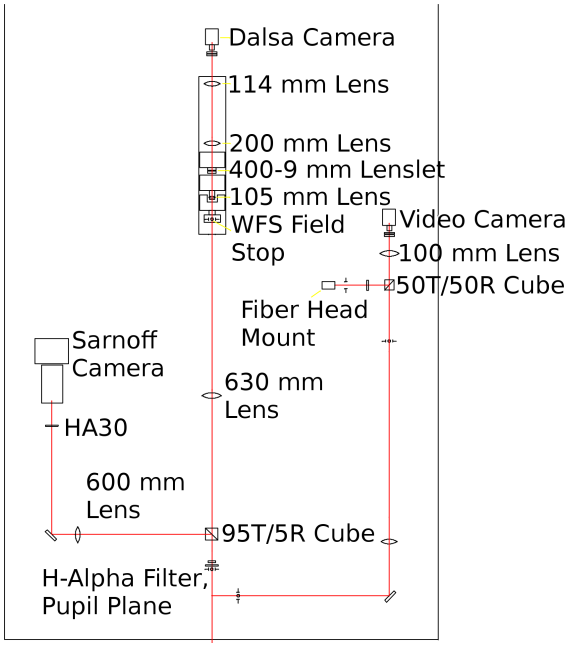

Fig. 3.5.— The experimental setup on Port 2 of the DST. The WFS is at top, with the imaging camera at left. An interferometer can be used to verify the flatness of the DM. It is to the right of the WFS and is used by diverting all light from the WFS, via a mirror.

depends upon the resolution to which the SHWFS can sample the wavefront.(Noll 1976; Hardy 1998) Even if those K-L modes can be perfectly determined, there are a residual error in the wavefront, corresponding to the infinite number of K-L modes which were not sensed.(Noll 1976; Dai 1995) K-L modes are ranked in various orders. Each mode in each consecutive order contributes less to the total error in the wavefront. Thus, the correction of a few modes can correct most of the distortion in the incoming wavefront.(Noll 1976; Dai 1995) Our setup can sense 20 K-L modes. Noll (1976) has tabulated the residual error expected after correcting 20 Zernike modes, which are similar to K-L modes, but with slightly higher residuals errors. (Noll 1976; Dai 1995)

The other major caveat is the way in which KAOS arrives at its measurements

of the total wavefront error in each K-L mode. It is done by noting the residual error in each mode and determining how much correction is being applied in each mode via the TTM and the DM and combining the two. If the pixel scale of the SHWFS was measured incorrectly, both the residual and total error measurements will be wrong. However, we have ensured that our measurements of the pixel scale are accurate. The DM used was a spare at the DST, and its neutral state wasn't exactly flat. This coupled with any static errors in the system, which would be corrected by the DM, affects the total wavefront error measurements.

To compare the measured performance of our AO system with the expected performance, shown in Figure 2.10, there are a few parameters which are of interest: r_0, B_{cl}, and the Strehl Ratio of the system. r_0 is also known as the Fried Parameter. (Fried 1965) It is defined as the diameter on the telescope pupil over which the total wavefront error is one radian of phase. It is generally specified at a wavelength of 5000 Å, and scales with wavelength as $r_0' = r_0(\lambda/5000)^{6/5}$. (Hardy 1998) B_{cl} is the "Closed-Loop Bandwidth". If we treat the AO loop like an RC filter, where higher update frequencies are attenuated, then B_{cl} can either be defined as the $0db$ or the $-3db$ cutoff frequency.(Hardy 1998) See the explanation of Strehl Ratio in Section 2.3.3.

r_0' can be calculated from the formula given by Noll (1976):

$$\langle \phi^2 \rangle = C * (D/r_0')^{5/3}. \tag{3.1}$$

Where D is the diameter of the telescope and $\langle \phi^2 \rangle$ is the variance wavefront error, in radians. C is a constant which is defined by the expected relative variance in a given mode, for a given turbulence model.(Noll 1976; Dai 1995) The average

variance of the first 3 modes was used, after Tip and Tilt, since these have the same approximate variance of $0.023927(D/r_0')^{5/3}$.(Dai 1995) Also, Tip and Tilt are subject to vibrations in the room, etc. r_0' was calculated by finding the average wavefront error over a series of 10,000 frames, or approximately 12 seconds. With r_0' known, it is trivial to find r_0. The Strehl Ratio can be approximated by:(Hardy 1998)

$$e^{-1\times[(\sum_i \phi_i^2)+residual]}. \tag{3.2}$$

Where, $\sum_i \phi_i^2$ is the sum of the residual errors for each mode over our time series, calculated by KAOS, and the residual is approximated here as: $0.0208(D/r_0')^{5/3}$. (Noll 1976) This is the residual for Zernike Polynomials, but it is only slightly more than that for K-L modes. (Noll 1976; Dai 1995)

Finding B_{cl} is a bit more involved. It is found by taking the power-spectrum of the residual error for a given mode with the AO system off, and plot it against the power-spectrum of the same mode with the AO system on (See Figure 3.6). The point at which they first cross is the $0db$ B_{cl}, the $-3db$ is where the corrected power is twice that of the uncorrected power. The Welch Method was used to plot the power-spectra.(Welch 1967)

3.2.2. Results

Telemetry data taken according to the procedure found in Section 3.2.1 were analyzed. These data were taken with the AO system correcting for 20 K-L modes. We found the $0db$ bandwidth to be approximately 38.8Hz and the $-3db$ bandwidth to be approximately 67.6Hz (See Figure 3.6. These values depend upon the degree of smoothing of the power spectra, so they are only "ballpark figures".

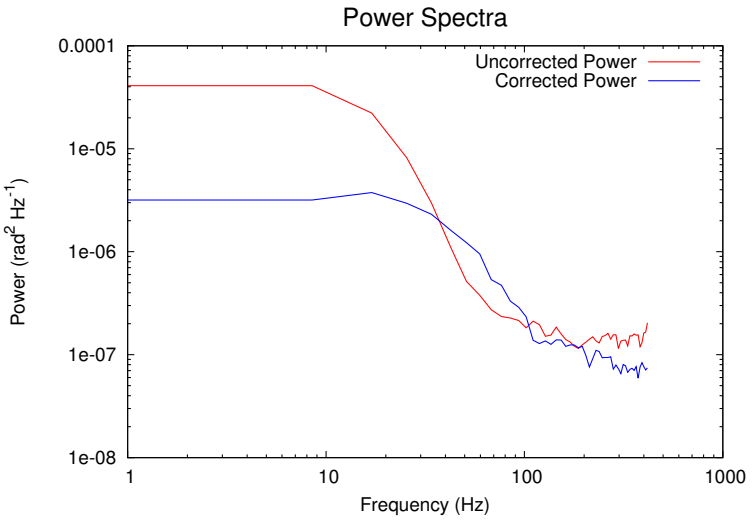

Fig. 3.6.— The power spectra from which B_{cl} was calculated. The approximate $0db$ and $-3db$ bandwidth values were found by interpolation.

A sample of the r_0 values and Strehl ratios we calculated are shown in Table 3.2.2. The data represent a temporal average, over a period of 12 seconds. One can note the large standard deviation among the r_0 values. This is due to the rapidly changing atmosphere. We did not have an accurate way to measure the Greenwood Frequency. Since total Strehl ratio depends upon this frequency, this accounts for the variation in measured Strehl ratios among similar r_0 values. Even given this fact, the below results measure favorably with our predictions, as shown in Figure 2.10. Also note that when the Strehl Ratio is highest, its standard deviation is lowest, which points to the stability of the AO system, during times of good seeing.

The 5000 Å r_0 and 8542 Å Strehl ratios from Table 3.2.2 are plotted in Figure 3.7. Note that for r_0 around 10cm, the Strehl Ratio is between 0.6 and 0.7, slightly

exceeding our predictions. This may be due to our very pessimistic time-delay error estimation. The spread in r_0 vs Strehl ratio is almost certainly due to the variation in Greenwood Frequency, but this is seen to be a secondary effect.

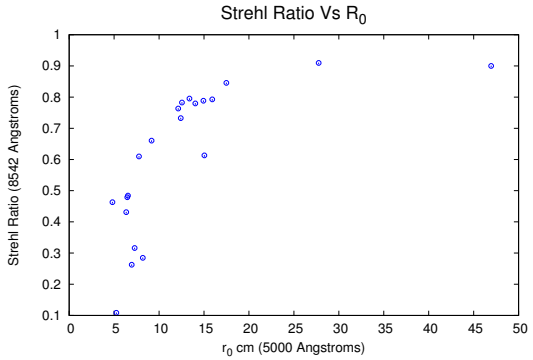

Fig. 3.7.— A graph of Strehl Ratio Vs r_0 value. Note that for $r_0 \sim$ 10cm, The Strehl Ratio is between 0.6 and 0.7, bettering predictions.

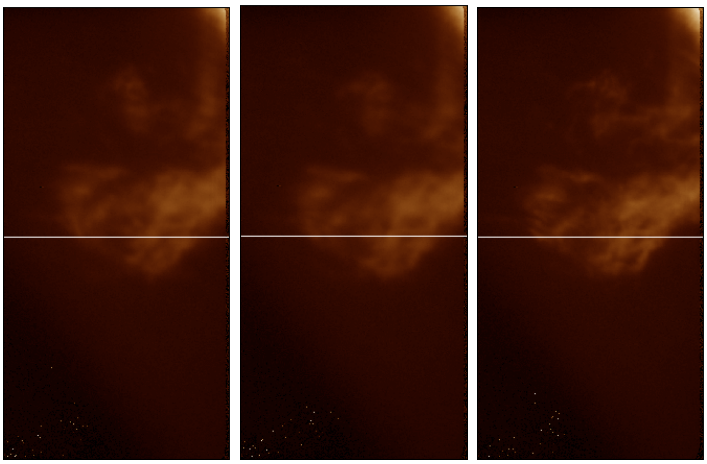

Fig. 3.8.— The above images were taken on December 10, 2013, between 16:50 and 16:55 UTC. Each image is the average of 100 frames, with a cadence of $4s^{-1}$. Each series was taken at 6563 Å. They show what a long exposure would look like during moments of moderate seeing, with the AO system totally off (left), only correcting for tip and tilt (center), and with the AO system correcting for 20 modes. r_0 varied from between about 15cm and 17cm, when these images were taken. (The second line in Table 3.2.2 was taken a few moments after the right hand image was taken.) Cross sections of each image are shown by the white line. Pixel values for each will be shown in Figure 3.9

Figure 3.8 depicts a few images which show the dramatic improvement that the AO system can provide. The images are each made from a series of 100 frames with an exposure time of 200ms each. They were taken at a frame rate of 4 frames-per-second and span 25 seconds. To better show the resolution improvement made in this figure, their cross sections are plotted in Figure 3.9. The left most image shows the cross section with the AO system turned off. The smooth variation in the curve belies the blurry nature of the image. With the Tip-Tilt mirror activated, the line shows more variation, meaning more image detail is visible, but the curve still changes smoothly. The right image shows very sharp edges and much more variation. This indicates the presence of much more detail at high contrast.

Figure 3.10 shows the improvement in image quality given by the off-limb AO system. For the first 3000 frames, the AO is applying no correction, the residual error is the same as the total atmospheric error, as measured by KAOS. At around frame 3000, we begin correcting for Tip and Tilt only. The residual error becomes the same as the total error minus the Tip and Tilt errors. Finally, at around frame 7000, we apply full AO correction, the residual error drops far below the total error lines. The seeing was quite good with, r_0 of around 17cm.

Figure 3.11 Shows the corresponding Strehl Ratios, calculated during the same sequence as that in Figure 3.10. Although the seeing is good, the improvement allowed by correcting for Tip and Tilt alone is highly variable and much lower than that given by making the full correction.

Similar tests were performed for a 7X7 SHWFS setup. The AO system wasn't able to stay locked very well, plus the measurement of the WFS pixel scale wasn't

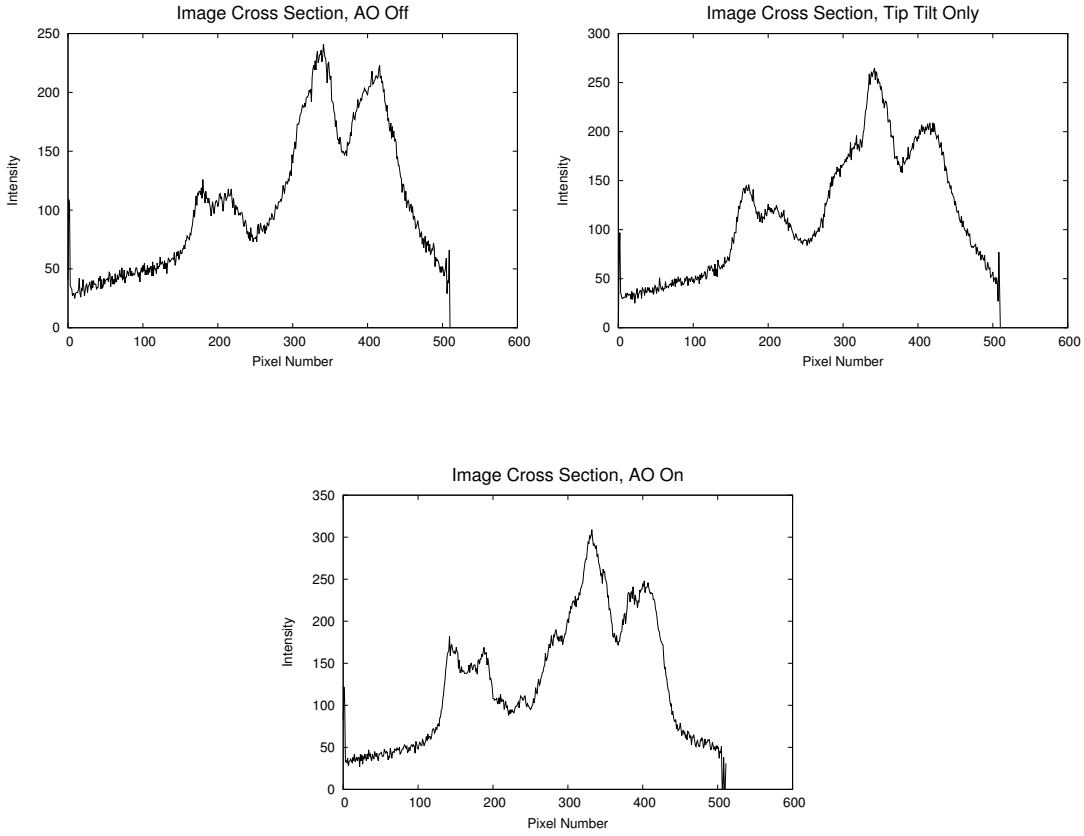

Fig. 3.9.— Cross Sections taken of each image image in Figure 3.8. The increase in sharpness for the fully corrected image is depicted by the sharp edges shown in the graph. This indicates that much finer details are visible.

accurate, due to a last-second lens substitution. For this reason, these data will not be included here. It was necessary to make note of this, however. In the ideal case, with a faster, less noisy, albeit much more expensive camera, a 7X7 array should work very well. However in this case, it was at the limit of what the hardware could do, making the 5X5 much more practical.

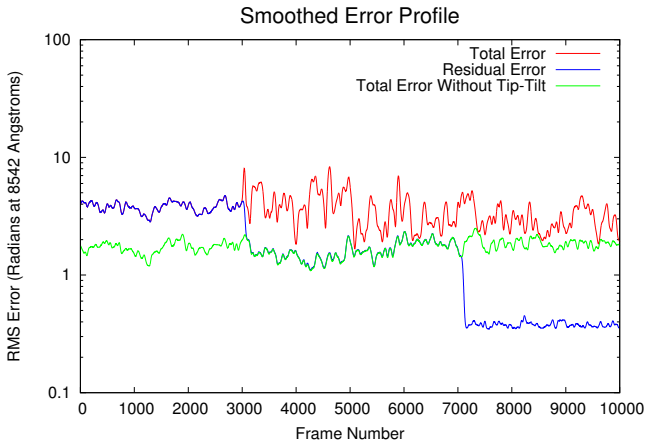

Fig. 3.10.— Wavefront error in radians at 8542 Å. These data have been smoothed by convolving them with a Gaussian Kernel, with a standard deviation of 15. The total error calculation becomes very noisy, once the TTM is activated, but the total without Tip and Tilt stays well behaved, even when the AO is fully activated. Since the reconstructed Tip and Tilt total errors weren't used for any calculations, this is of little consequence.

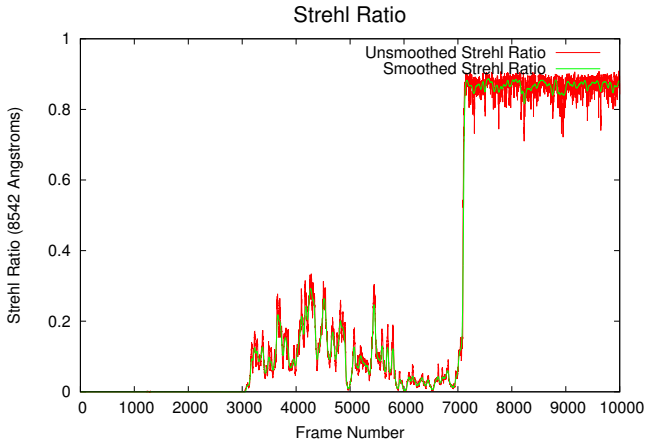

Fig. 3.11.— Strehl Ratio at 8542 Å for the data plotted in Figure 3.10. These data have been smoothed by convolving them with a Gaussian Kernel, with a standard deviation of 15. Although the Strehl Ratio is at times higher than 0.2, when only the TTM is active, it is highly variable.

3.2.3. Verification of Strehl Measurements

The Strehl measurements made above were verified by calculating the expected Strehl ratio in the same method as outlined in Section 2.3.2 However, since an accurate value for the time delay value τ_s, in Equation 2.10 wasn't known, a variant form was used:(Hardy 1998)

$$\sigma^2_{\mathrm{TD}} = \left(\frac{f_g}{f_{3db}}\right)^{5/3}, \tag{3.3}$$

where f_g is the Greenwood frequency and f_{3db} is the $-3db$ bandwidth above. Though there isn't a reliable way to find f_g from closed-loop data. Open loop data can be used to find f_g. The data set plotted in Figure 3.10 was used for this purpose. Part is open loop, part closed, which allows for a direct comparison between the Strehl ratio found calculated from the residual errors, as calculated by KAOS, and that predicted by the method in Section 2.3.2. Fried (1990) gives a method to find f_g from a Phase Fluctuation Power Spectrum. This is the exact power spectrum as calculated in Section 2.3.2. The only difference being that the power spectrum must be in terms of radians squared. This is calculated by multiplying the power spectrum, in terms of pixels squared by the factor:

$$(2\pi(((0.82/3600)/57.3) * 13.07\ cm * 100000000\ cm/\text{Å})/6563\text{Å})^2$$

This converts shifts in terms of pixels to radians of phase. (0.82/3600)/57.3 converts the angle per pixel from arcseconds ($0.82''$per pixel) into radians per pixel. The remaining factors convert radians of angle into radians of phase. 13.07cm is the physical size of a subaperture and 6563Å is the wavelength at which the measurements were made. The square is due to the power spectra being in terms of radians squared and pixels squared. Following the logic of Fried (1990), that if

two independent apertures have twice the mean square variance of a single one, then a full aperture will have a mean square variance equal to the ratio of its area vs the area of a single subaperture. Thus the power spectrum must be multiplied by this ratio. For high frequencies, that are below the noise cutoff:(Fried 1990)

$$\Phi_\phi(f) = (2\pi)^{-1} f_g^{5/3} |f|^{-8/3} \tag{3.4}$$

Where $\Phi_\phi(f)$ is the phase power spectrum, f_g is the Greenwood Frequency and f is frequency in Hz. From Equation 3.4 it is trivial to solve for the Greenwood Frequency:

$$f_g = \left(2\pi \frac{< \Phi_\phi(f) >}{|f|^{-8/3}} \right)^{3/5} \tag{3.5}$$

$< \Phi_\phi(f) >$ being the average of $\Phi_\phi(f)$ where the power spectrum follows $|f|^{-8/3}$ well. Values of $\Phi_\phi(f)$ between 30 and 70 Hz were averaged, as this is a region where the power spectrum follows the $|f|^{-8/3}$ shape particularly well. Figure 3.12 shows the scaled power spectrum, with power in units radians squared, with Equation 3.4 plotted for the Greenwood Frequency found in Equation 3.5. This power spectrum was calculated by measuring the motion of the tip and tilt of the wavefront in each subaperture. The power spectrum was taken of this motion. All of these power spectra were added together to make the final spectrum, as explained above. The fit to the $|f|^{-8/3}$ line is shown as the diagonal line in the graph.

With σ^2_{TD} known, the WFS noise was found with the same method as that described in Section 2.3.2. The power spectrum is plotted in Figure 3.13. The power spectrum is shown to have a noticeable noise-tail, just as shown in Section Section 2.3.2. The noise level is shown as the dotted line. All other noise sources are the same as those found in Section 2.3.2, but using the value for r_0 calculated

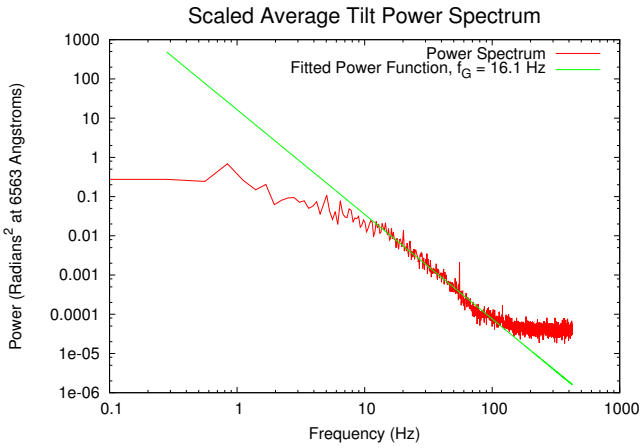

Fig. 3.12.— Phase power spectrum, in terms of radians, for the open-loop cross-correlation peak shift data, as described in the text. This is plotted along with the line found by fitting Equation 3.4 to the spectrum, as explained in the text.

from KAOS error data. Results from using this method on several data sets are tabulated in Table 3.2.3.

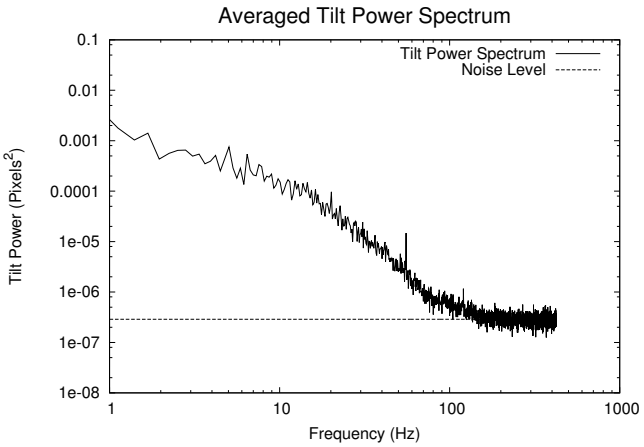

Fig. 3.13.— Noise Power Spectrum taken from the open loop cross-correlation shifts, during open-loop portion of Figure 3.10.

Note that Table 3.2.3 shows that the Predicted Strehl is closest to that ob-

Table 3.1. A sampling of r_0 and Strehl ratios.

r_0 cm, 5000 Å	Standard Deviation	Strehl, 8542 Å	Standard Deviation	Strehl, 6563 Å
15.9184	7.5325	0.7926	0.0652	0.6773
14.9362	6.9773	0.7884	0.0610	0.6709
17.4868	9.2392	0.8456	0.0395	0.7536
9.1684	4.7710	0.6605	0.0609	0.4978
6.4664	3.1955	0.4789	0.0713	0.2911
14.0340	6.7349	0.7797	0.0791	0.6601
12.1283	6.4545	0.7635	0.0497	0.6346
6.3531	3.2902	0.4312	0.0820	0.2457
12.4115	8.7072	0.7327	0.0707	0.5937
27.7547	16.9233	0.9097	0.0382	0.8527
46.9440	24.7305	0.9000	0.0707	0.8397
7.7688	6.6223	0.6098	0.0754	0.4366
6.5431	3.9170	0.4841	0.0989	0.3001
12.5479	6.7247	0.7827	0.0560	0.6624
13.3796	7.0181	0.7954	0.0510	0.6803
4.8167	2.5083	0.4631	0.0125	0.2716
15.0399	7.6358	0.6131	0.1380	0.4499
6.9543	3.8224	0.2626	0.1305	0.1192
5.2454	2.8631	0.1084	0.0942	0.0332
8.1936	4.3825	0.2846	0.1346	0.1349
7.2867	3.7827	0.3161	0.1220	0.1549

Table 3.2. Strehl Comparison

r_0 cm, 5000 Å	r_0 cm, 6563 Å	Greenwood Frequency Hz at 6563 Å	Strehl from KAOS data	Predicted Strehl
16.4873	22.8512	25.2142	0.8110	0.7918
19.0975	26.4688	26.1654	0.8524	0.7941
36.6253	50.7622	34.2277	0.8179	0.7589
17.0242	23.5953	16.1223	0.8665	0.8638
25.7892	35.7435	46.5290	0.7513	0.6694
7.7077	10.6827	51.7470	0.5945	0.4769
24.3757	33.7844	92.3926	0.5947	0.3478

tained for KAOS data, when the Greenwood frequency is lowest. This could be due to various factors. For one, the power spectrum from which the Greenwood Frequency measurement was taken doesn't follow the -8/3 power slope well. The Greenwood frequency fits for each data set are plotted, in the order in which they appear in Table 3.2.3, in Figures 3.14 through 3.20. These figures show the power spectra and the $|f|^{-8/3}$ functional fits, just as in Figure 3.12.

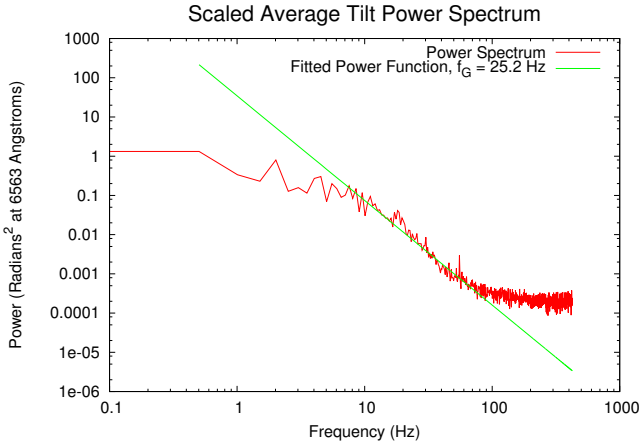

Fig. 3.14.— Table 3.2.3 line 1.

Additionally, the fitting criterion was somewhat arbitrary, but it is close for all but the very fastest Greenwood Frequency measurement. Because these Greenwood Frequency measurements provide believable numbers, and the predictions from this method come fairly close to the measured values, this is believed by the author to be a reasonable method for confirming the measurements taken by KAOS. Also note: There was a lot of wind on the day during which the last data set was taken, both on the ground and aloft, thus the Greenwood Frequency should have been quite high. Also, even though the average measured Strehl for that data set was 0.6, this was only due to the large r_0 value. The Limb AO

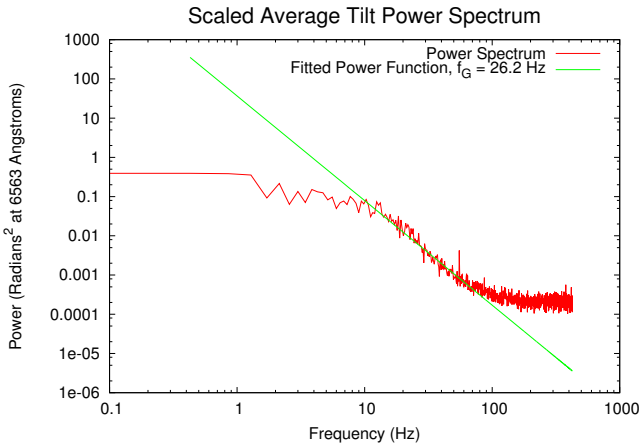

Fig. 3.15.— Table 3.2.3 line 2.

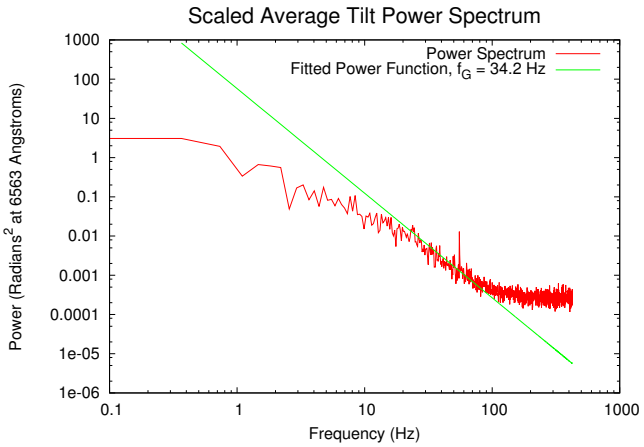

Fig. 3.16.— Table 3.2.3 line 3.

system had great difficulty maintaining the lock and there was a great deal of variance in the Strehl Ratio measurement. This is shown in Figure 3.21. Finally, the atmosphere its self could have changed, from the time that the AO system was completely off, to the time when it was fully locked, several seconds later. Indeed this is very probable. Nevertheless, the comparisons in Table 3.2.3 instill

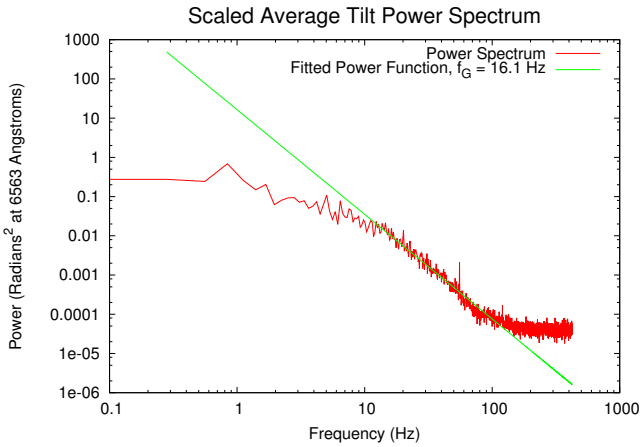

Fig. 3.17.— Table 3.2.3 line 4.

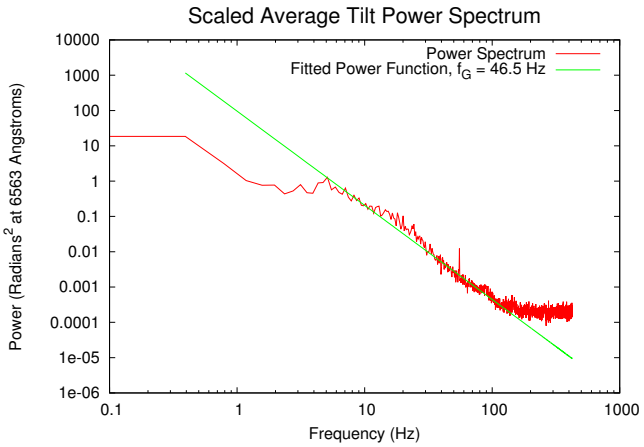

Fig. 3.18.— Table 3.2.3 line 5.

a good deal of confidence.

The second to the worst prediction was on line 6 of Table 3.2.3. This data The predicted Strehl is shown in Figure 3.22. This graph shows that there is still a great deal of variance in the Strehl measurements, but the system is well behaved.

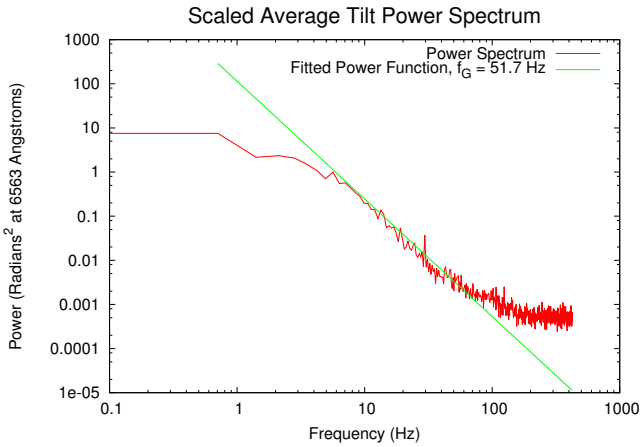

Fig. 3.19.— Table 3.2.3 line 6.

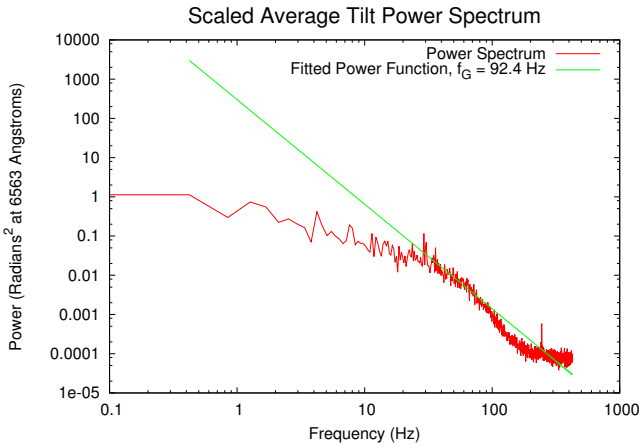

Fig. 3.20.— Final line from Table 3.2.3 The power spectrum taken for this data set doesn't follow the -8/3 power law slope well.

The results in Table 3.2.3 and Figures 3.21 and 3.22 show an additional piece of information: The AO system works best when the Greenwood Frequency is below the $-3db$ frequency of the AO system.

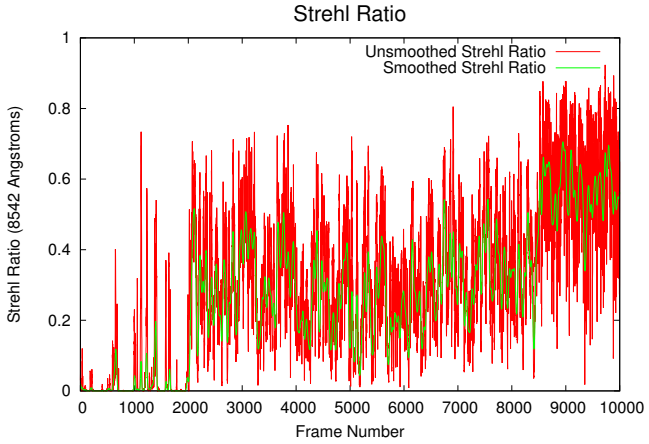

Fig. 3.21.— Final line from Table 3.2.3. The Limb AO system had a great deal of trouble keeping the lock during this dataset. The AO is off from Frame 0-2000, TT only from Frame 2000-8500 and on from 8500-10000.

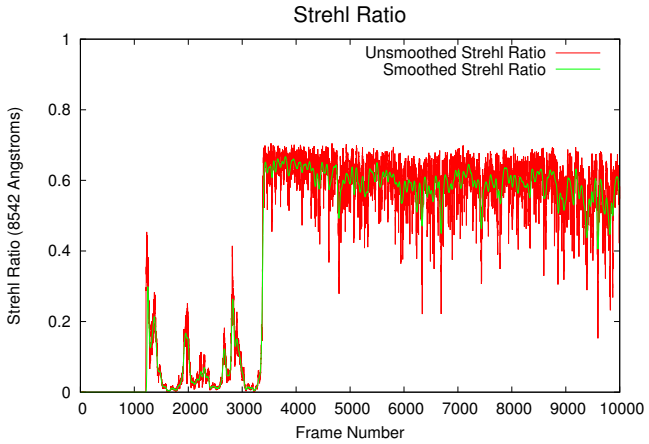

Fig. 3.22.— Final line from Table 3.2.3. The Limb AO system is well behaved during this data set.

4. STATEMENT OF SCIENTIFIC PROBLEM

In the study of solar prominences, there is one significant phenomenon that has recently come to the attention of scientists. That is what happens during the creation of bubbles and plumes in quiescent prominences. Bubbles form beneath quiescent prominences and are dark in visible light images. Plumes form at the top boundary between a prominence and a bubble. They seem to be turbulent flows within a prominence and larger plumes may pass all the way through it.(Berger 2014) Such a plume was noted by Stellmacher & Wiehr (1973), who deduced that some sort of instability was responsible for it. The phenomenon of rising plumes was re-discovered after the launch of the Hinode Satellite. About that time, de Toma et al. (2008) noted these plumes in Hα images taken at the Mauna Loa Observatory. Ryutova et al. (2010) were the first to to suggest that these plumes were consistent with a Rayleigh-Taylor (RT) buoyancy instability. In general, an RT instability occurs when an dense fluid is suspended above a less-dense one, in this case, against the force of gravity.(Chandrasekhar 1981)

4.1. Rayleigh-Taylor Instability

Chandrasekhar (1981) gives a thorough introduction into the RT instability, both in the non magnetic and the magnetic case. In the case of RT instabilities, in solar prominences, we assume that the prominence material is held aloft by a magnetic field that is horizontal with respect to gravity.(Kippenhahn & Schlüter 1957) The following derivation is from Chandrasekhar (1981), for the horizontal magnetic field case:

Start with the equations of ideal Magnetohydrodynamics:(Chandrasekhar

1981; Davidson 2001)

$$\frac{\partial \mathbf{B}}{\partial t} - \nabla \times (\mathbf{u} \times \mathbf{B}) = 0, \tag{4.1}$$

where $\mathbf{B}$ is the magnetic field vector and $\mathbf{u}$ is the velocity vector.

$$\mathbf{E} = -\mu \mathbf{u} \times \mathbf{B}, \tag{4.2}$$

where $\mathbf{E}$ is the electric field vector and μ is the magnetic permeability.

$$\nabla \cdot \mathbf{B} = 0. \tag{4.3}$$

$$\int_S \mathbf{B} \cdot dS = \text{constant}. \tag{4.4}$$

Where S is a closed surface.

$$\frac{d}{dt}\left(\frac{B_i}{\rho}\right) = \frac{B_j}{\rho}\frac{\partial u_i}{\partial x_j} \tag{4.5}$$

Where ρ is the density of the material and B_i, x_j, and u_i are vector components of each, respectively. Finally,

$$\frac{\partial \mathfrak{M}}{\partial t} = \mu \int_V \mathbf{u} \cdot (\mathbf{B} \times \mathbf{J})\, dV + \frac{\mu}{4\pi} \int_S (\mathbf{H} \cdot \mathbf{u})\, \mathbf{B} \cdot d\mathbf{S}, \tag{4.6}$$

where, $\mathfrak{M}$ is the magnetic energy contained in volume V, $\mathbf{J}$ is the electric current density and

$$(\mathbf{B} \times \mathbf{J}) = -\mathscr{L}, \tag{4.7}$$

which is the Lorentz force.

The rest of the derivation comes from Chandrasekhar (1981): We assume that any disturbance in equilibrium has the following form:

$$e^{(ik_x x + ik_y y + nt)}, \tag{4.8}$$

where k_x, k_y, and n are constants. k_x and k_y are the spatial wave numbers of the disturbance. Let the horizontal magnetic field be defined to be in the x direction. The perturbation equations become:

$$\rho n u = -ik_x \delta p, \tag{4.9}$$

$$\rho n v - \frac{\mu B}{4\pi}\left(ik_x b_y - ik_y b_x\right) = -ik_y \delta p, \tag{4.10}$$

$$\rho n w - \frac{\mu B}{4\pi}\left(ik_x b_z - D b_x\right) = -D\delta p + \frac{g}{n}\left(D\rho\right) w, \tag{4.11}$$

where $D = \frac{d}{dz}$ and u, v, and w are the x, y, and z components of velocity, respectively. ρ is the density of the parent material and δp is the change in pressure. g is the gravitational acceleration. b_x, b_y, and b_z are perturbations in the magnetic field, where

$$\mathbf{b} = \frac{ik_x}{n} B\mathbf{u}. \tag{4.12}$$

Inserting the components of $\mathbf{b}$ into Equations 4.10 and 4.11, we get:

$$\rho n v - \frac{ik_x}{n}\frac{\mu B^2}{4\pi}\zeta = -ik_y \delta p \tag{4.13}$$

and

$$\rho n w - \frac{ik_x}{n}\frac{\mu B^2}{4\pi}\left(ik_x w - Du\right) = -D\delta p \frac{g}{n}\left(D\rho\right) w, \tag{4.14}$$

where

$$\zeta = ik_x v - ik_y u \tag{4.15}$$

Multiplying Equations 4.9 and 4.13 by $-ik_y$ and ik_x, respectively, and adding them together, we get:

$$\left(\rho n + \frac{k_x^2}{n}\frac{\mu B^2}{4\pi}\right)\zeta = 0. \tag{4.16}$$

Thus:

$$\zeta = ik_x v - ik_y u = 0. \tag{4.17}$$

Therefore, Equation 4.13 becomes:

$$\rho n v = -ik_y \delta p. \tag{4.18}$$

Equations 4.9 and 4.18 can be combined, after multiplying them by $-ik_x$ and $-ik_y$, respectively to obtain:

$$\rho n Dw = -k^2 \delta p, \tag{4.19}$$

where $k^2 = k_x^2 + k_y^2$. From Equation 4.17 and the equation:

$$ik_x u + ik_y v = -Dw, \tag{4.20}$$

we find:

$$u = i\frac{k_x}{k^2} Dw \tag{4.21}$$

Inserting Equation 4.21 into Equation 4.14, we find:

$$\rho n w - \frac{\mu B^2 k_x^2}{4\pi k^2 n}\left(D^2 - k^2\right) w = D\delta p + \frac{g}{n}\left(D\rho\right) w. \tag{4.22}$$

Using Equation 4.19 and 4.22, δp can be eliminated, giving:

$$D\left(\rho Dw\right) + \frac{\mu B^2 k_x^2}{4\pi n^2}\left(D^2 - k^2\right) w - k^2 \rho w = -\frac{gk^2}{n^2}\left(D\rho\right) w. \tag{4.23}$$

When $k_x = 0$, Equation 4.23 reduces to:

$$D\left(\rho Dw\right) - k^2 \rho w = -\frac{gk^2}{n^2}\left(D\rho\right) w; \tag{4.24}$$

Which is the same form as that obtained for no magnetic field. When $k_x \neq 0$, we make note of the condition that w and b_z are continuous at $z = 0$, but Equation 4.12 implies that b_z is continuous when w is continuous. Satisfying the condition that "w is continuous when $z = 0$", we need only satisfy the condition:

$$\Delta_0\left(\rho Dw\right) + \frac{\mu B^2 k_x^2}{4\pi n^2}\Delta_0\left(Dw\right) = \frac{gk^2}{n^2}(\rho_2 - \rho_1) w_0, \tag{4.25}$$

which follows from integrating Equation 4.23 across the interface. ρ_1 and ρ_2 are the densities below and above the interface, respectively. w_0 is the z velocity at the interface.

$$\Delta_0(f) = f(z_0 + \varepsilon) - f(z_0 - \varepsilon), \tag{4.26}$$

is the jump experienced by f across the interface at z_0, ε being an infinitesimal number. Applying the following, for the two fluids:

$$w_1 = Ae^{+kz}(z < 0) \tag{4.27}$$

$$w_2 = Ae^{-kz}(z > 0), \tag{4.28}$$

where A is a constant, we obtain:

$$n^2 = gk \left\{ \frac{\rho_2 - \rho_1}{\rho_2 + \rho_1} - \frac{\mu B^2 k_x^2}{2\pi(\rho_2 + \rho_1)gk} \right\}. \tag{4.29}$$

The additional term of k_x^2 in Equation 4.24 has an effect which is the same as surface tension. This effective tension can be defined as:

$$T_{\text{eff}} = \frac{\mu B^2}{2\pi k} \cos^2 \vartheta, \tag{4.30}$$

where ϑ is the inclination of the wave vector (k_x, k_y) to the direction of $\mathbf{B}$. This tension originates in the tension $\mu B^2/4\pi$, which exists along the lines of force. The effect of this tension when $k_x \neq 0$, and its absence when $k_x = 0$, are clearly shown by the simulations of Khomenko et al. (2014).

4.2. Observational Plan

The observational plan is to study rising plumes on quiescent prominences and determine if their motions are consistent with those arising from RT instabilities. This will be don by measuring the 3D velocities of prominence plumes, or more

specifically, the surrounding material, using IBIS, at the DST.(Cavallini & IBIS Team 2004) The measurements will be taken of the 8542 Å spectral line, using the Limb AO system. Time series of sufficient length will allow for the observation of any plume motion.

5. OBSERVATIONS

The Limb AO system was installed on Port 4 of the DST. The optical layout of the SHWFS its self was virtually identical to that used on Port 2, See Figure 3.5. The difference being that a Dichroic beam-splitter was included to divert only Hα light toward the SHWFS, the rest was sent to IBIS. Figure 5.1 shows the layout for this setup. There was some difficulty in finding a CAD drawing of Port 4, so a photograph is shown. The optical components are the same as used on Port 2, in Figure 3.5.

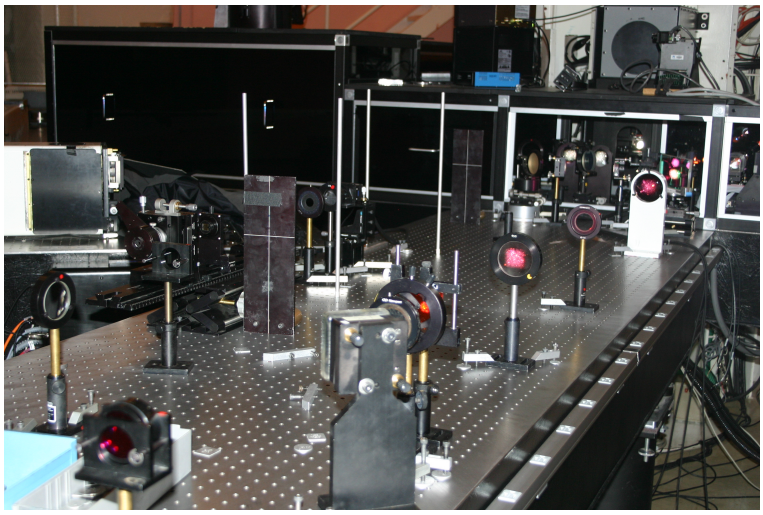

Fig. 5.1.— The optical layout on Port 4.

IBIS was set to intensity only mode, with the central wavelength of 8542 Å. (See Cavallini & IBIS Team (2004) for more on IBIS.) In this configuration, twin Fabre-Perot (FP) ètalons were used to create a band pass of several tens of Femto Meters. The central wavelength passed by the FP ètalons can be tuned by applying voltage to controllers FP1 and FP2. A program of 17 wavelengths per scan was selected. This means that images were taken at each of 17 wavelengths, which represent a scan through the 8542 Å line. The file length was set at five

scans per file. A sample of the data logged for one file is shown in Table 5.

Observations were taken on December 17 and 19, 2013. Images of each prominence were taken for the maximum useful time, given seeing and cloud conditions. Table 5 shows the start and finish times for each data set, as well as the position of the prominence on the sun, and other relevant parameters.

Table 5.1. Sample Observation File

Filter	Relative Wavelength Å	Acquisition Time	FP1 V1	FP2 V2	ExpTime (sec)	Stokes
8542	-0.5541	17/Dec/2013 16:52:44.168	-142	41	0.200	I
8542	-0.4289	17/Dec/2013 16:52:44.483	-72	61	0.200	I
8542	-0.3054	17/Dec/2013 16:52:44.794	-3	81	0.200	I
8542	-0.1926	17/Dec/2013 16:52:45.107	60	99	0.200	I
8542	-0.0924	17/Dec/2013 16:52:45.417	116	115	0.200	I
8542	-0.0065	17/Dec/2013 16:52:45.731	164	129	0.200	I
8542	0.0687	17/Dec/2013 16:52:46.041	206	141	0.200	I
8542	0.1188	17/Dec/2013 16:52:46.354	234	149	0.200	I
8542	0.1689	17/Dec/2013 16:52:46.663	262	157	0.200	I
8542	0.2190	17/Dec/2013 16:52:46.972	290	165	0.200	I
8542	0.2673	17/Dec/2013 16:52:47.282	317	173	0.200	I
8542	0.3425	17/Dec/2013 16:52:47.594	359	185	0.200	I
8542	0.4302	17/Dec/2013 16:52:47.905	408	199	0.200	I
8542	0.5411	17/Dec/2013 16:52:48.213	470	217	0.200	I
8542	0.6539	17/Dec/2013 16:52:48.525	533	235	0.200	I
8542	0.7791	17/Dec/2013 16:52:48.835	603	255	0.200	I
8542	0.9026	17/Dec/2013 16:52:49.145	672	275	0.200	I
8542	-0.5541	17/Dec/2013 16:52:49.457	-142	41	0.200	I
8542	-0.4289	17/Dec/2013 16:52:49.768	-72	61	0.200	I
8542	-0.3054	17/Dec/2013 16:52:50.081	-3	81	0.200	I
8542	-0.1926	17/Dec/2013 16:52:50.390	60	99	0.200	I
8542	-0.0924	17/Dec/2013 16:52:50.702	116	115	0.200	I
8542	-0.0065	17/Dec/2013 16:52:51.011	164	129	0.200	I
8542	0.0687	17/Dec/2013 16:52:51.320	206	141	0.200	I
8542	0.1188	17/Dec/2013 16:52:51.632	234	149	0.200	I
8542	0.1689	17/Dec/2013 16:52:51.941	262	157	0.200	I
8542	0.2190	17/Dec/2013 16:52:52.248	290	165	0.200	I
8542	0.2673	17/Dec/2013 16:52:52.558	317	173	0.200	I
8542	0.3425	17/Dec/2013 16:52:52.869	359	185	0.200	I
8542	0.4302	17/Dec/2013 16:52:53.181	408	199	0.200	I
8542	0.5411	17/Dec/2013 16:52:53.492	470	217	0.200	I
8542	0.6539	17/Dec/2013 16:52:53.805	533	235	0.200	I
8542	0.7791	17/Dec/2013 16:52:54.115	603	255	0.200	I
8542	0.9026	17/Dec/2013 16:52:54.427	672	275	0.200	I
8542	-0.5541	17/Dec/2013 16:52:54.736	-142	41	0.200	I
8542	-0.4289	17/Dec/2013 16:52:55.045	-72	61	0.200	I
8542	-0.3054	17/Dec/2013 16:52:55.356	-3	81	0.200	I
8542	-0.1926	17/Dec/2013 16:52:55.664	60	99	0.200	I
8542	-0.0924	17/Dec/2013 16:52:55.976	116	115	0.200	I
8542	-0.0065	17/Dec/2013 16:52:56.288	164	129	0.200	I
8542	0.0687	17/Dec/2013 16:52:56.598	206	141	0.200	I
8542	0.1188	17/Dec/2013 16:52:56.908	234	149	0.200	I
8542	0.1689	17/Dec/2013 16:52:57.218	262	157	0.200	I
8542	0.2190	17/Dec/2013 16:52:57.527	290	165	0.200	I
8542	0.2673	17/Dec/2013 16:52:57.838	317	173	0.200	I
8542	0.3425	17/Dec/2013 16:52:58.150	359	185	0.200	I
8542	0.4302	17/Dec/2013 16:52:58.458	408	199	0.200	I

Table 5.1 (continued)

Filter	Relative Wavelength Å	Acquisition Time	FP1 V1	FP2 V2	ExpTime (sec)	Stokes
8542	0.5411	17/Dec/2013 16:52:58.769	470	217	0.200	I
8542	0.6539	17/Dec/2013 16:52:59.081	533	235	0.200	I
8542	0.7791	17/Dec/2013 16:52:59.394	603	255	0.200	I
8542	0.9026	17/Dec/2013 16:52:59.704	672	275	0.200	I
8542	-0.5541	17/Dec/2013 16:53:00.013	-142	41	0.200	I
8542	-0.4289	17/Dec/2013 16:53:00.324	-72	61	0.200	I
8542	-0.3054	17/Dec/2013 16:53:00.636	-3	81	0.200	I
8542	-0.1926	17/Dec/2013 16:53:00.948	60	99	0.200	I
8542	-0.0924	17/Dec/2013 16:53:01.257	116	115	0.200	I
8542	-0.0065	17/Dec/2013 16:53:01.568	164	129	0.200	I
8542	0.0687	17/Dec/2013 16:53:01.878	206	141	0.200	I
8542	0.1188	17/Dec/2013 16:53:02.189	234	149	0.200	I
8542	0.1689	17/Dec/2013 16:53:02.500	262	157	0.200	I
8542	0.2190	17/Dec/2013 16:53:02.810	290	165	0.200	I
8542	0.2673	17/Dec/2013 16:53:03.123	317	173	0.200	I
8542	0.3425	17/Dec/2013 16:53:03.431	359	185	0.200	I
8542	0.4302	17/Dec/2013 16:53:03.745	408	199	0.200	I
8542	0.5411	17/Dec/2013 16:53:04.054	470	217	0.200	I
8542	0.6539	17/Dec/2013 16:53:04.363	533	235	0.200	I
8542	0.7791	17/Dec/2013 16:53:04.674	603	255	0.200	I
8542	0.9026	17/Dec/2013 16:53:04.984	672	275	0.200	I
8542	-0.5541	17/Dec/2013 16:53:05.295	-142	41	0.200	I
8542	-0.4289	17/Dec/2013 16:53:05.608	-72	61	0.200	I
8542	-0.3054	17/Dec/2013 16:53:05.920	-3	81	0.200	I
8542	-0.1926	17/Dec/2013 16:53:06.230	60	99	0.200	I
8542	-0.0924	17/Dec/2013 16:53:06.541	116	115	0.200	I
8542	-0.0065	17/Dec/2013 16:53:06.852	164	129	0.200	I
8542	0.0687	17/Dec/2013 16:53:07.160	206	141	0.200	I
8542	0.1188	17/Dec/2013 16:53:07.469	234	149	0.200	I
8542	0.1689	17/Dec/2013 16:53:07.779	262	157	0.200	I
8542	0.2190	17/Dec/2013 16:53:08.093	290	165	0.200	I
8542	0.2673	17/Dec/2013 16:53:08.402	317	173	0.200	I
8542	0.3425	17/Dec/2013 16:53:08.713	359	185	0.200	I
8542	0.4302	17/Dec/2013 16:53:09.025	408	199	0.200	I
8542	0.5411	17/Dec/2013 16:53:09.335	470	217	0.200	I
8542	0.6539	17/Dec/2013 16:53:09.647	533	235	0.200	I
8542	0.7791	17/Dec/2013 16:53:09.957	603	255	0.200	I
8542	0.9026	17/Dec/2013 16:53:10.269	672	275	0.200	I

Table 5.2. Observation Data Sets

Number of scans	Start Time UTC	End Time UTC	Stony Hurst Latitude	Stony Hurst Longitude	Heliocentric Position Angle	Heliocentric Radius Vector
300	2013-12-17 16:23:23.155	2013-12-17 16:50:11.545	-30.710165	90.426271	239.28824	1.0109487
265	2013-12-17 16:52:44.494	2013-12-17 17:16:19.014	-65.584140	-92.100276	155.60132	1.0253192
65	2013-12-17 17:19:22.879	2013-12-17 17:25:10.074	-32.575555	-90.479100	122.57769	1.0264107
500	2013-12-17 17:32:16.640	2013-12-17 18:02:54.446	-32.685768	-90.482831	122.68794	1.0189056
500	2013-12-17 18:03:05.745	2013-12-17 18:33:42.073	-32.685745	-90.484568	122.68794	1.0189037
500	2013-12-17 19:43:09.208	2013-12-17 27:41.155	-38.514076	-90.661036	128.51806	1.0305234
500	2013-12-19 15:34:02.198	2013-12-19 16:04:29.229	-20.553385	-90.271571	110.55339	1.0095985
500	2013-12-19 16:04:58.783	2013-12-19 16:35:26.453	-20.553372	-90.272585	110.55339	1.0095968
500	2013-12-19 16:36:27.464	2013-12-19 17:06:53.182	-21.791147	-90.308492	111.79162	1.0078409
500	2013-12-19 17:09:37.999	2013-12-19 17:54:15.208	32.380331	-88.724719	57.598306	1.0200615
500	2013-12-19 18:00:06.079	2013-12-19 18:44:32.888	32.221597	-88.728338	57.757036	1.0239320

5.1. Data Processing

5.1.1. IDL Preprocessing Routines

When IBIS takes spectroscopic data, due to the optical design, the center of the image is blueshifted, relative to the edges.(S. Criscuoli, Private Communication) In addition to the usual flat fielding, and dark subtraction, the preprocessing routines must correct for this artifact. This is done by measuring the intensity across the flat field images, for each of the 17 wavelengths, and determining how much the software needs to correct each image. This allows for the spectroscopic data to be scientifically accurate in each image, across the entire field of view. The preprocessing package also can be used to de-stretch the images, in order to counteract the atmosphere's distortion. However, de-stretching wasn't applied here, as it is very complicated with prominences and can even crash or yield unpredictable results, when it tries to de-stretch the large amount of black space around the prominence.(K. Reardon, Private Communication)

After the IDL code finishes, it returns proprietary .sav files, containing all of the image data. These were converted to .fits files, using IDL, in order to allow me to use my own Perl Data Language (PDL) code to do the final processing.(See pdl.perl.org (2014))

Figure 5.1 shows the result from the IBIS preprocessing. The optics in the IBIS bench caused a somewhat severe reflection artifact. Figure 5.1 was logarithmically scaled, to show the bright limb and faint prominence and reflections in the same image.

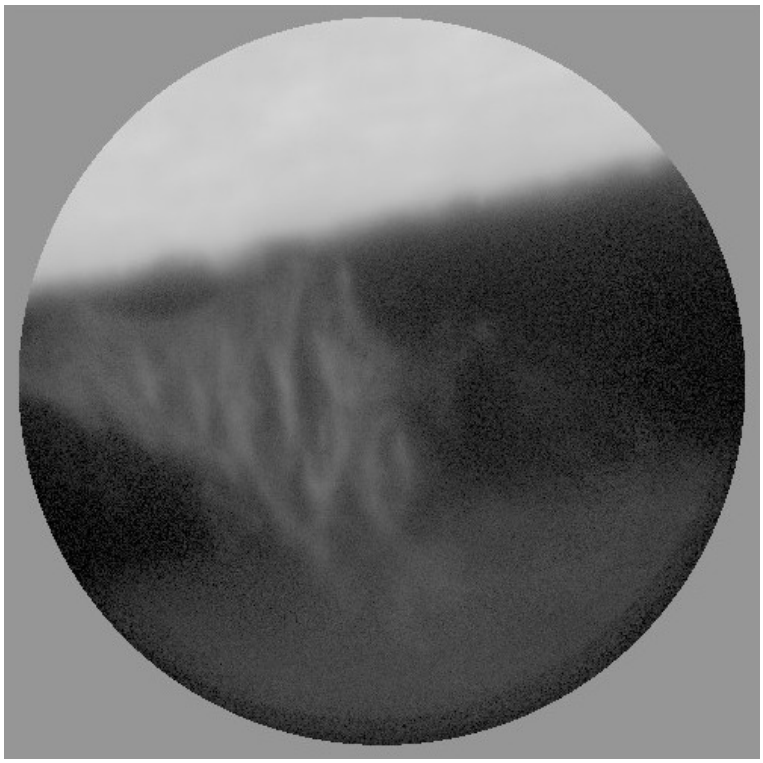

Fig. 5.1.— A raw preprocessed image, of the 8542 Å line center. Internal reflections from the IBIS optical train are evident. This image has been log scaled, to show the reflections more clearly.

5.1.2. Velocity Extraction

For each spectral scan, the intensity per pixel, per wavelength was extracted. This translates into a coarse spectrum for each pixel. On the first attempt, 5 scans were averaged together, in order to increase the signal to noise ratio. A sample raw spectrum is shown in Figure B.2. It turned out that there was a large degree of background light contaminating the spectrum. In order to remove the background, 100 spectra from an area well away from the prominence and solar limb were averaged. All reflections from the IBIS optics, as shown in Figure 5.1, were carefully avoided. The background spectrum is shown in the center panel. Once it was subtracted, the resultant spectrum is clearly due to emission from the

solar prominence. This result is shown in the right-hand panel.

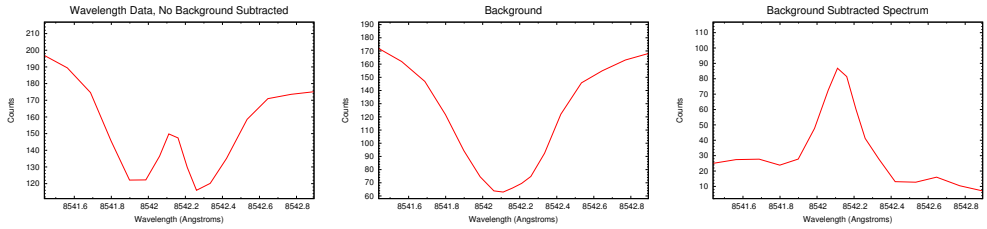

Fig. 5.2.— Left: A sample raw spectrum, showing a great deal of background contamination. Center: The extracted background spectrum. Right: The same spectrum as on the left, but with the background removed, showing itself to be an emission spectrum.

With the spectra extracted, it was necessary to fit a function to each spectrum, in order to determine the center of the spectral line. Three different functions were fitted to each, two different Gaussians and a cubic. The functional fits will be shown in Figure 5.3. Details of how these fits were performed will be explained below.

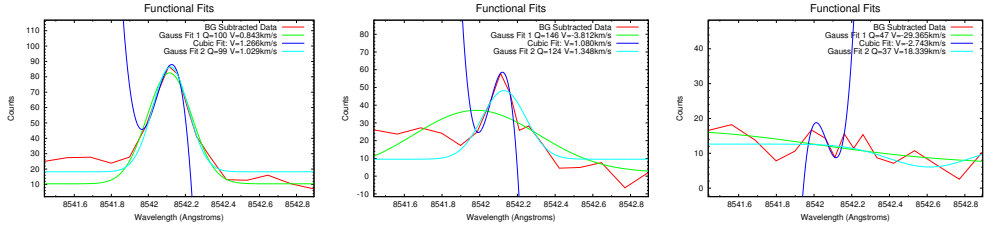

Fig. 5.3.— Left: Functional fits for high SNR data. Center: Functional fits for low SNR data. The built-in Gaussian fit failed, while my slow Gaussian fit came-up with a better result. The hyper-slow cubic also did well. Right: Functional fit on pure noise, no fitting routine could fit this spectrum. Units are $km\ s^{-1}$.

The cubic function seemed to find the center well on high Signal-to- noise-Ratio (SNR) data, but did poorly on other data. When the functional parameters of the cubic were found, the derivative was taken to find the zeros, one of which was the maximum. The second derivative was taken, to find which zero had a

negative slope, this point was taken to be the maximum. On data with poor SNR, the cubic would get confused, so it was difficult to be sure if it would be sufficiently accurate, over the whole data set. It was also painfully slow, the few hundred million fits in the entire data set took nearly 24 hours.

The first Gaussian was a built-in fitting routine that fit the function using the central few points, and estimated the background. This function was quite robust and perhaps 10 times faster than the cubic fit routine. The way in which it fit the background wasn't satisfactory. Also, the center of the Gaussian didn't seem exactly centered with what the eye would see as the center of the spectral line. However, it was very consistent, over all but the poorest data, it could even fit Gaussians with a negative peak, for absorption data, like on the disk.

The second Gaussian fit was an iterative fitting routine. The resultant fit quality was compared with that of the first Gaussian by measuring the sum of the absolute value of the difference between the spectral line and the fits at each wavelength, ie $\sum_i |fit_i - spec_i|$. Better fits could be obtained routinely, but only at the expense of speed. If this fitting function were made to run as fast as the first Gaussian, the resultant velocity map would be very noisy (See Figure 5.7). Only by slowing the fitting routine down, to make sure it was accurate, did I obtain a high quality map. This made the second Gaussian fit about as slow as the cubic fit. For This reason, the first Gaussian fitting method was selected. It should be noted that the iterative fitting routine ran in parallel, with three cores, while the built-in Gaussian fit was using a single core.

Using the first Gaussian function, the velocity analysis was repeated for single scans and for the average two scans, not just the original average of five. To do

this with the cubic routine would have taken weeks, but this took less than 18 hours to do literally billions of Gaussian fits.

5.1.3. Velocity Maps

Once the peak wavelength was calculated, the velocity of the plasma was determined, relative to the observer, using the standard formula:(Carrol & Ostlie 1996)

$$v = c\left(\frac{\lambda - \lambda_0}{\lambda_0}\right), \tag{5.1}$$

where c is the speed of light, 299792.458 $km\ s^{-1}$, and λ_0 is 8542.09 Å.(NIST 2014) The velocity, v was plotted for each pixel and made into a velocity map. The resultant velocity maps, from each fitting method, are shown in Figures 5.4 through 5.7.

Since these are busy images, it is proper to discuss in detail what they contain. At each pixel of each velocity map one can see the velocity found by fitting the central peak of the derived spectrum at that point. Multiple different regions are evident in which the bulk motion of the plasma is either away from the viewer or toward the viewer, denoted as a positive and negative velocity, respectively (bright and dark on the velocity map). Figure 5.4 shows the result of determining the velocities via a cubic fit to the spectra. Figure 5.5 shows the result for the first Gaussian fit. Figure 5.6 shows the result of the second Gaussian fit, running at a very low speed. Figure 5.7 is the high-speed version of the second Gaussian fit. This produces a very noisy velocity map.

It is difficult to see the difference between the velocity maps obtained by the

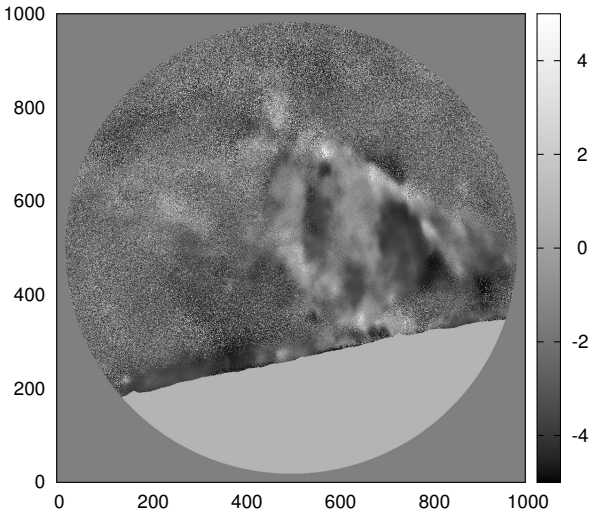

Fig. 5.4.— Velocity map derived from the cubic function fit. Units are $km\ s^{-1}$.

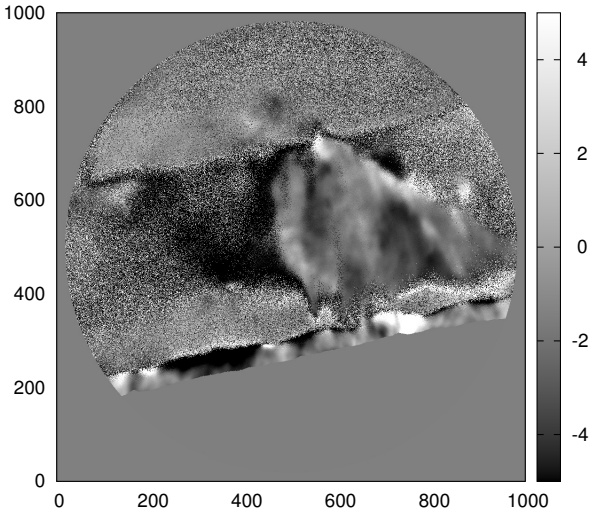

Fig. 5.5.— Map derived from Gaussian Fit 1. Units are $km\ s^{-1}$.

different methods here, due to the way in which these images were reproduced, but the difference is real enough. The first Gaussian fit seems to be the most

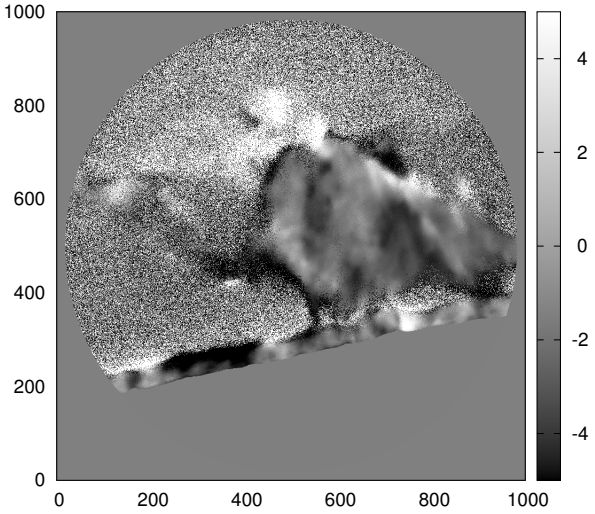

Fig. 5.6.— Velocity map derived from Gaussian Fit 2. Units are $km\ s^{-1}$.

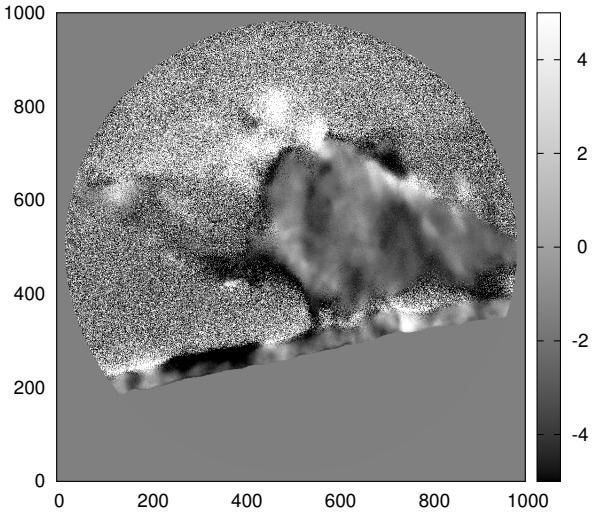

Fig. 5.7.— Velocity map derived from Gaussian Fit 2, at high speed. Units are $km\ s^{-1}$.

robust, it even captures the velocity in the reflected light, even though that light is substantially fainter than the prominence.

The take-away message from these velocity maps is that the first Gaussian fit method is by far the best, given the speed at which it runs and the quality of the velocity map which it produces. It is quite evident that there is much more detail in the velocity map its self, that is there are many subtle differences in velocity visible within any given region. The interpretation of this will need to be looked at in finer detail, but it is clear that more information can potentially be extracted from these higher quality data.

5.2. Image Refinement

Some of the images were sharpened in order to overlay them over the velocity maps. The process was straight forward: The first step was to stack the line center image, plus the one blue-ward and the one red-ward of line center, in order to simulate a single image taken with Hinode, or a similar instrument, since the IBIS passband is very narrow, to allow for precise spectroscopic analysis. The second step was to remove the background, which was done using the same pixels that were used to remove the background from the spectroscopic data. Most of the reflections were removed by simulating them with two components. A rotated image plus a shifted, rotated one, was then subtracted from the original. This mostly removed the reflection artifact. The result of this step is shown in Figure 5.8.

An un-sharp mask was applied to the original, to enhance the detail.(Jansson 2012) This was done by convolving the image with a Gaussian kernel, to make

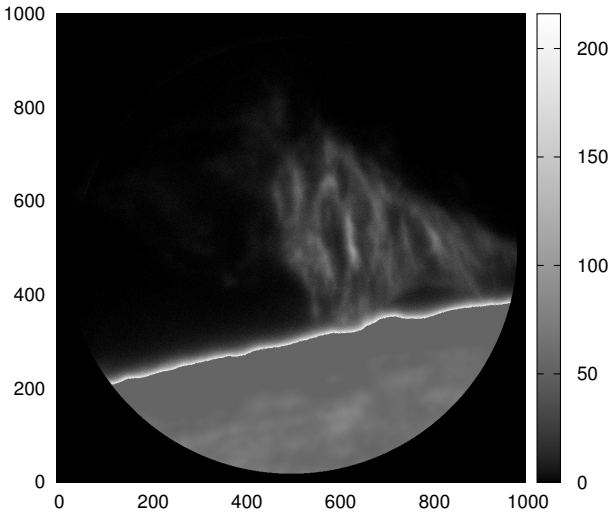

Fig. 5.8.— Image with the background and reflections subtracted.

a blurred copy of the original. This blurred copy was then subtracted from the original, to create an image of the fine details in the original. Finally the detail image was added to the original, thus enhancing the details in it. The result of this step is shown in Figure 5.9.

This also enhanced the considerable noise of the original, hence the resulting image was convolved with a very small Gaussian kernel, sufficient to remove the noise, but not significantly blur the image. The limb was masked with a crude gradient mask, such that the brightest parts were dimmed the most. This final step is shown in Figure 5.10. Figures 5.8, 5.9, and 5.10 are displayed this size to show the difference between them.

Figure 5.11 shows the processed image overlaid with a velocity map. In this case, a rainbow color scheme is used to allow the viewer to see the velocity map and the image at the same time. The color scheme was chosen such that blue

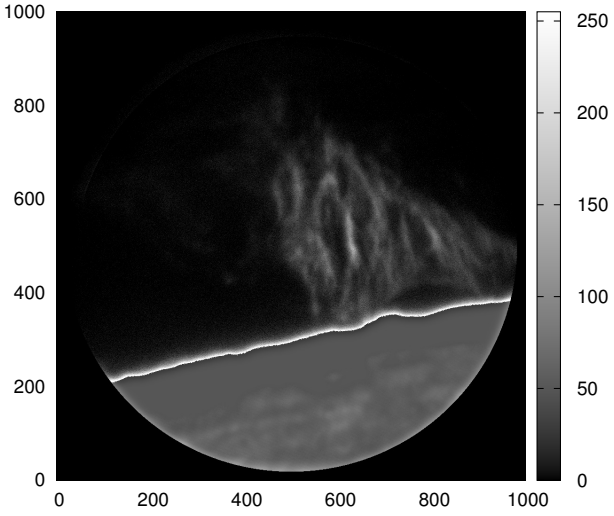

Fig. 5.9.— Image after applying a mild un-sharp mask.

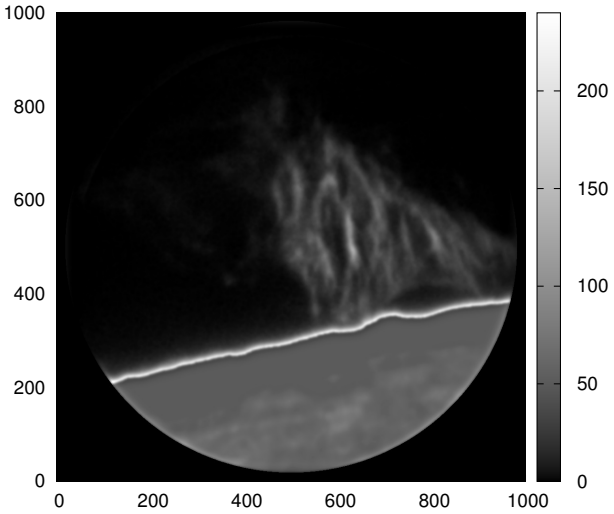

Fig. 5.10.— Image after noise removal.

represents blue-shifted light; red represents red-shifted light. The maxima are -5 and 5 $km\ s^{-1}$, as before. One can immediately see the relationship between the

details in the image and the velocity of those components.

An additional step was taken in processing the velocity map for this and all subsequent velocity data. Each frame at each wavelength had the reflected light subtracted, just as was done for the image data. The velocities were then calculated in the same manner as before. This allowed the determining of the velocity in the very topmost part of the solar prominence. There are some horizontal artifacts which remain after the subtraction process, but they do not affect the final quality of the velocity map.

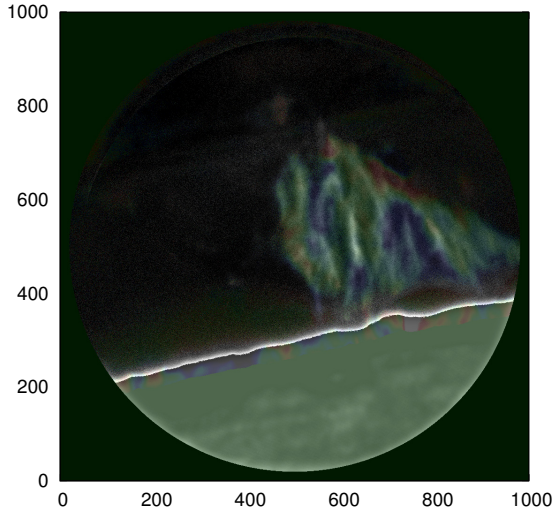

Fig. 5.11.— Overlay of velocity map corresponding to the time of the image.

6. RESULTS

6.1. Imaging Data

Analysis of the data set which were processed in Section 5.1 show what can convincingly be shown to be a RT instability developing and turning into a plume which rises through the prominence. Figures 6.1 through 6.4 show the instability developing. Figure 6.1 shows the perturbations as they are just forming in the bubble below the prominence. This is manifested by the slight scalloping on the left hand edge of the bubble and its flat top. These are denoted by a yellow line and an arrow, respectively. Figure 6.2 shows the further development of the RT instability. Here the Instability has already begun to enter the non-linear phase, where the initial perturbations grow rapidly to form a plume. This is shown by the yellow outline, the arrow shows the direction of propagation. Figure 6.3 shows the plume about ready to rise. It is outlined in yellow. Figure 6.4 shows the rising of the plume which developed in the RT instability. Again, outlined in yellow. Figure 6.5 shows the late stages of the plume rising. This plume shows the classic "mushroom head" indicative of a Kelvin-Helmholtz instability in the rising material. (Tom Berger, Private Communication) The plume is outlined in yellow and arrows point to the Kelvin Helmholtz instabilities.

This prominence also exhibits behavior that further indicates that the rising plume of material begins as an RT instability. Recall that an RT instability occurs when dense material is supported over light material. Berger (2014) states the there should therefore be material visible in data from the Solar Dynamics Observatory. In Figure 6.6, this is indeed visible. In the left panel is an image taken in 191 Å light (The bubble is outlined in yellow). The timing of this image

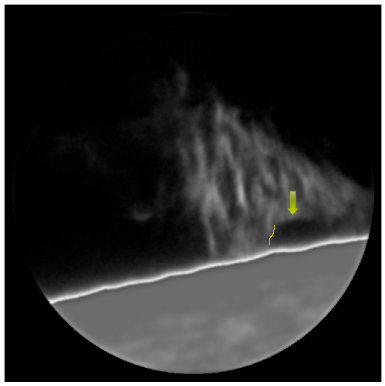

Fig. 6.1.— The beginning of an RT instability, shown by the slight scalloping on the left hand side of the bubble and the flat top of the bubble. (Yellow line and arrow, respectively)

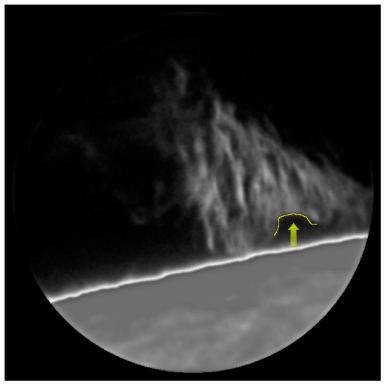

Fig. 6.2.— The continued development of an RT instability. Here the perturbations have become non linear and one is growing rapidly to become a plume.

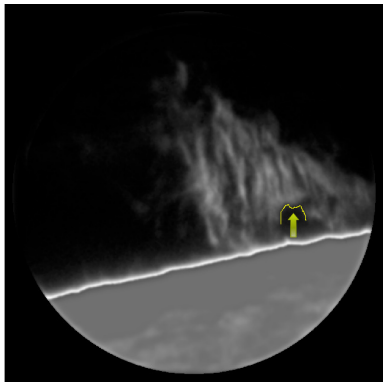

Fig. 6.3.— The RT instability has nearly reached its climactic eruption.

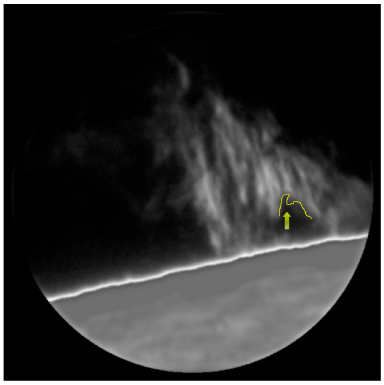

Fig. 6.4.— The RT instability has become a rising plume of material.

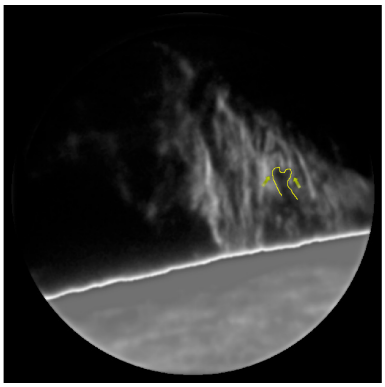

Fig. 6.5.— The rising plume of material has begun to have a Kelvin-Helmholtz instability on its top. This occurs when a plume of material rises through another material.

roughly corresponds to the beginning of the time series which was processed in Section 5.1 and is a few moments before Figure 6.1. The right hand panel was taken in 211 Å light and shows the rising plume, outlined in yellow. These data were obtained from the Heliophysics Coverage Registry.(HCR 2014)

6.2. Velocity Data

There are very many interesting results in the velocity data. Of particular note are the apparently very chaotic motions on the boundary of the bubble. In the very first frame of the series, Figure 6.7 The edge of the bubble appears to

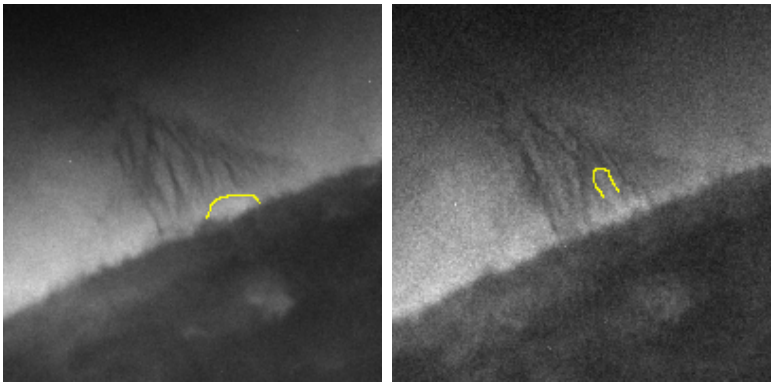

Fig. 6.6.— Left: An image in 191 Å light showing hot material within the bubble (outlined in yellow). Right: 211 Å data, showing hot material rising in the plume (outlined in yellow).

be highly redshifted. A closer look at the spectral line shows a different story. In Figure 6.8, all of the spectra within the yellow rectangle have been averaged. This shows what appears to be a very highly chaotic environment, with light in emission and absorption. The highly redshifted velocity which were extracted turns out to be a fit of this absorption feature. One should note that there is a great deal more scattered light this close to the limb, than the region where the normal background was subtracted.

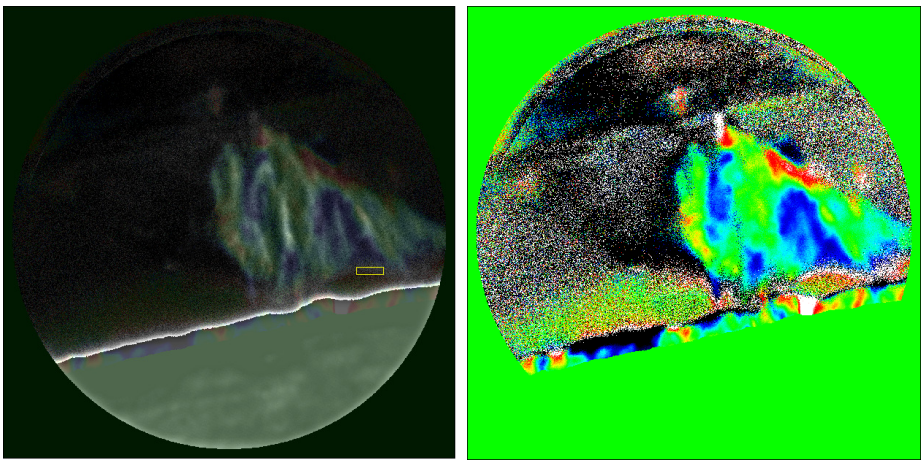

Fig. 6.7.— Left: Velocity map with image overlay, showing area where spectra were extracted. Right: Velocity map only, for reference.

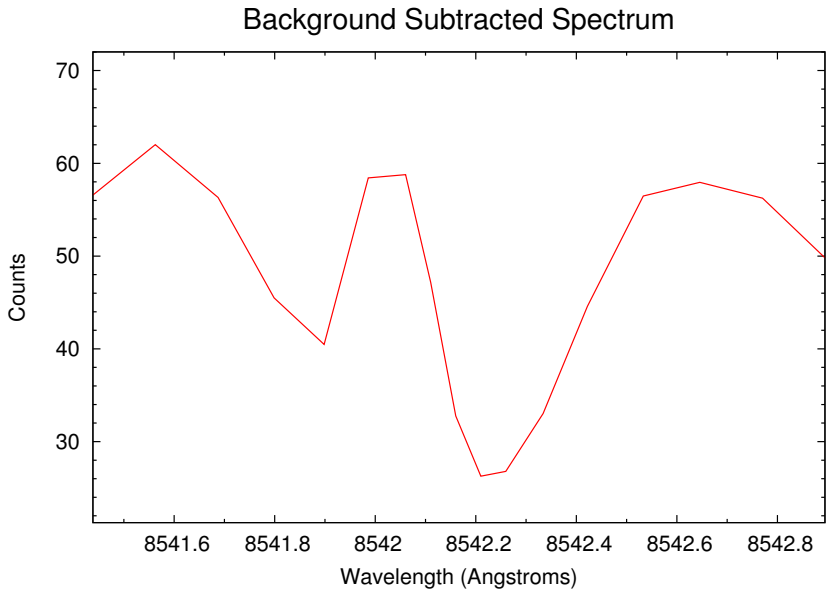

Fig. 6.8.— An average of the spectra from the rectangle in Figure 6.7.

A second area, close to the limb, was chosen from which to select a background to do background subtraction. When this was done, the ambiguity was immediately resolved. What appeared to be chaotic, turned out to be a solid emission spectrum, with a blueshifted velocity. This is shown in Figure 6.9. The blueshifted velocity seems to indicate that material is being pushed out of the way of the rising bubble, in this case, toward the observer.

The same procedure was performed with a second unusual area, later in the time series, as seen in Figures 6.10 through 6.12. Within this area the spectra were again averaged and the same background was subtracted as was done for the velocity maps in Section 5.1. This is shown in Figure 6.11. In Figure 6.12, The same background was subtracted as was used in Figure 6.9. Even with the

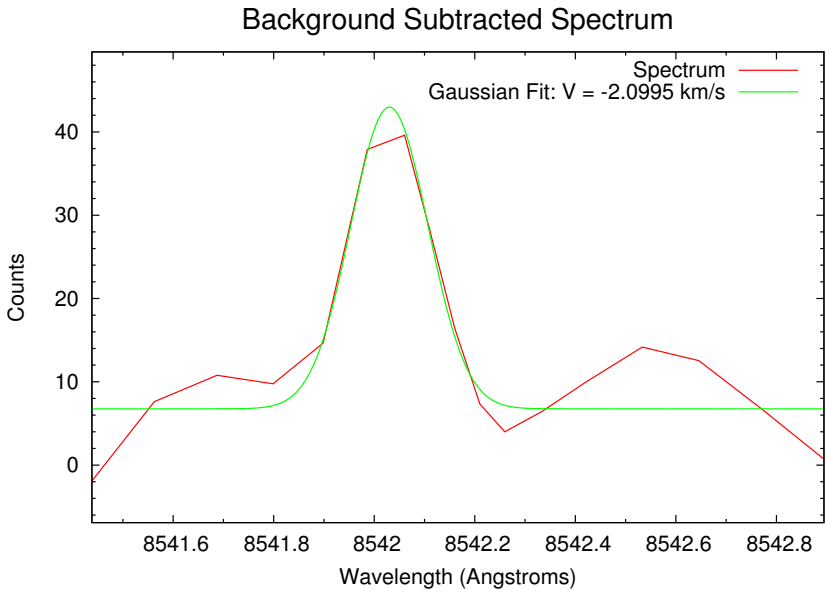

Fig. 6.9.— An average of the spectra from the rectangle in Figure 6.7, this time with the proper background subtracted, showing a clear blueshift.

subtraction of this stronger background, no reliable velocity could be extracted. This could probably be attributed to chaotic motion in the edge of the bubble, as the hot gas within rises.

Another interesting phenomenon can be found in the velocity maps. When the plume rises through the prominence, as shown in Figure 6.5, it pushes the prominence plasma out of its way, both to the sides as well as toward and away from the observer. Figure 6.13 clearly shows this happening. Plasma on the left of the plume is being pushed away from the observer while plasma on the right is being pushed toward the observer. The plume is outlined in yellow and the portions being pushed toward and away from the observer are denoted by arrows.

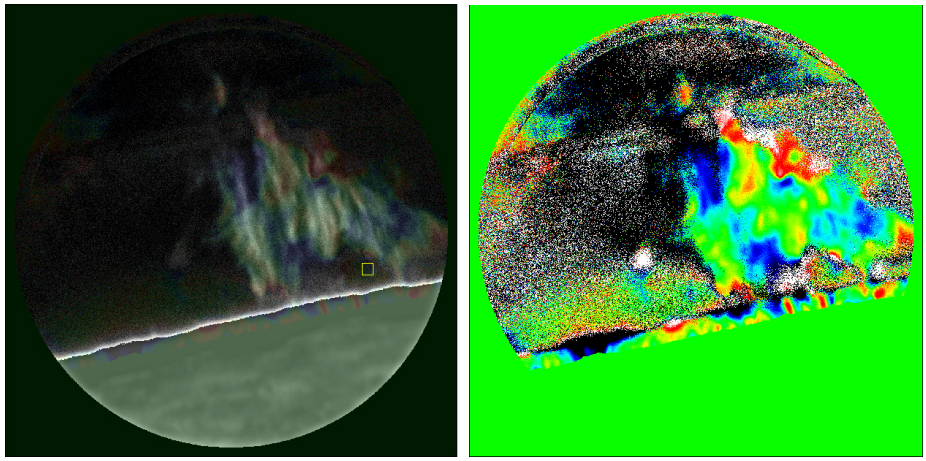

Fig. 6.10.— Left: Velocity map with image overlay, showing area where spectra were extracted. Right: Velocity map only, for reference.

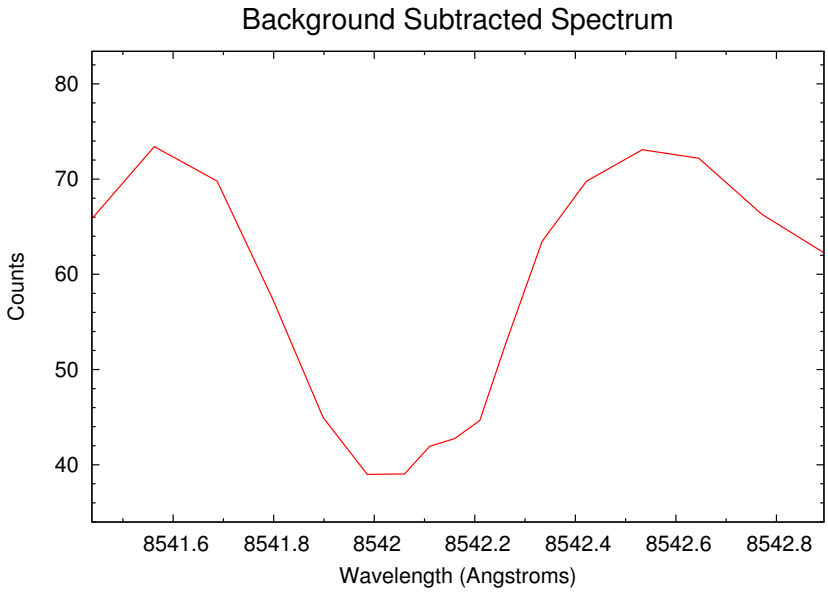

Fig. 6.11.— An average of the spectra from the rectangle in Figure 6.10.

6.3. Plasma Oscillation

There is one more interesting phenomenon that was noticed in this data set: When viewing an animation of the velocity maps, it was noticed that there is an

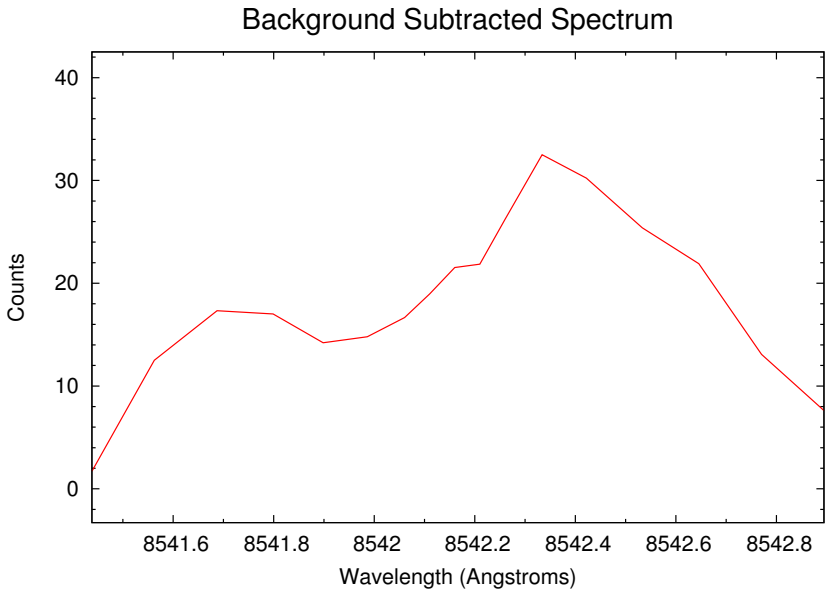

Fig. 6.12.— An average of the spectra from the rectangle in Figure 6.10, this time with the proper background subtracted. No velocity can be extracted here.

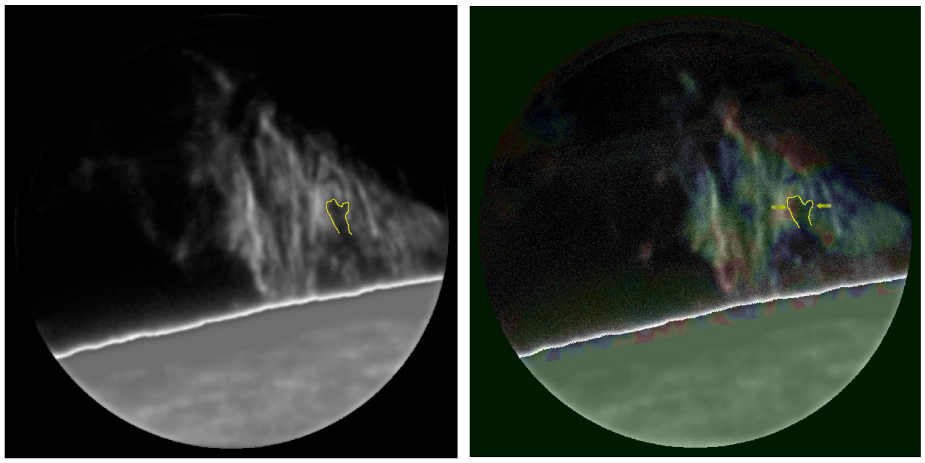

Fig. 6.13.— Left: The plume rising through the prominence. Right: Velocity map overlay on the same image, showing plasma being pushed out of the way of the plume. (Arrows)

oscillation. The plasma seems to be oscillating toward and away from the viewer, in such a way that the wave propagates from the right to the left, during the time

series. This sort of thing has been noticed before and is useful in determining the magnetic nature of solar prominences. (Ballester 2014) More study is needed to determine the nature of this oscillation: its wavelength, period, velocity, etc.

7. CONCLUSIONS AND FUTURE WORK

7.1. Conclusions

An AO system designed to work with light from solar prominences will be a great boon to the solar prominence community. This type of system will allow the study of solar prominences with unprecedented detail from the ground. As has been explained in Sections 1.3.1 and 3.2.3, there are many phenomena which can only be understood with high-resolution spectroscopy and spectropolarimetry data. In Section 3.2.3, the phenomenon of the Rayleigh-Taylor (RT) instability was examined in detail. This instability was shown to occur when a dense fluid is supported by a lighter fluid, in an accelerated system, in this case, under the force of gravity. (Chandrasekhar 1981)

The scientific data that was shown in Section 6 are consistent with an RT instability. There are a great many dynamical phenomena that my data show which would have been exceedingly difficult, if not impossible to get from the ground before now. Tom Berger at NSO is particularly interested in my data set and wants to use it in an upcoming paper, in which I will be one of the authors.

The fundamental principals of Adaptive Optics have been shown and, in particular, solar AO. The results of many experiments with various Shack-Hartmann Wavefront Sensors (SHWFS) were expounded. In Section 1.3.2 The results of many experiments with many different SHWFS configurations were shown. The process of optimizing a SHWFS was also shown in Section 1.3.2. This process included the modeling of various noise sources, to determine the most optimal frame rate for the SHWFS. It was shown that this system is really only limited by the capabilities of the available hardware. Every AO system must balance the

cost vs the performance of a system.(Hardy 1998) This AO system was built on a virtual shoestring budget, therefore the performance shown was truly remarkable.

Additionally, tests were performed with an alternative WFS, the Phase Diversity system, which is discussed in Appendix B.3. This WFS was proven to be inadequate for the Off-Limb AO system's needs, though it has promise for the future.

The utility of the Off-Limb Solar AO system has been thoroughly demonstrated. This system has been shown to work to the diffraction limit at Ca II 8542 Å, when the seeing conditions permit. Though it does require that the wind speed not be too high, see Section 3.2.2. When the conditions are right, the performance is truly astounding, given that it consists of essentially spare parts and an inexpensive camera for the SHWFS.

This AO system was mainly a proof-of-concept system. A fully optimized off-limb AO system, with the necessary budget for a high-end, ultra-low-noise camera for the SHWFS would surely be an important addition to any modern solar telescope and especially for the ATST.

7.2. A Few Important Points

There are a few quirks associated with the operation of an Off-Limb Solar AO system.

1. There must be contrast in the images within each subaperture in two orthogonal directions. Images that contain light from the solar disk, with a very faint prominence will cause the system to have a great deal of difficulty

in tracking the wavefront.

2. A prominence that is very large such that the image covers most of the subaperture, except for only one side will also cause trouble, unless there is sufficient contrast within the prominence to lock on to.

3. It is evident from this experiment, that prominences can and often do change very rapidly. This means that if one is locked upon some bubble-like feature in a prominence, the AO system will follow that bubble as it moves inside of the prominence. The KAOS system will update the reference subaperture image at whatever rate the user might choose. An update rate of once per minute was chosen. With this update rate, the AO system won't lose lock due to a changing prominence, but, as was said, the point onto which it is locked will change, relative to the position of the sun.

4. When the seeing is poor, the AO system will loose the lock. This causes KAOS to panic, setting the Tip-Tilt Mirror (TTM) and Deformable Mirror (DM) into extreme amounts of correction. In the case of the DM, this could be harmful, if allowed to persist. This is because adjacent actuators on the DM are set to opposite extremes of correction. This can cause undue strain to the points at which the actuators connect to the face-plate of the DM; see Figure 1.17.(Rimmele and Schmidt: Private Communication)

5. When the system panics, the procedure is to turn off all correction, manually update the reference image and re-lock the AO.

6. The DST staff was set upon using a particular set of off-band blocking filters for the main filter. This is due to the filter's design, it doesn't block light

that is far from the main passband, it would be too difficult to produce such a filter. The off-band filters used blocked a fair amount of light at Hα, upwards of 30% each. One of the broad-band IBIS blocking filters would have been preferable. This filter has a transmission of more than 80% at Hα and blocks UV and IR light very well. The techs could never be convinced to use one. Perhaps they were worried about UV light damaging the IBIS filter. Although I may not have explained myself properly when I requested this filter be used. The use of this filter for out of band blocking would have increased the light throughput to the SHWFS by a significant amount, more than 50%.

7.3. Future Work

A very large amount of spectroscopic data of solar prominences with IBIS and the off-limb AO were taken. Only a small portion of these data have been processed and analyzed, due to the size of the data sets involved. Future study of these data will hopefully show much about the dynamics of solar prominences. Spectropolarimetry data of prominences have also been taken, again with IBIS and the off-limb AO. As the processing of them is much more involved, the analysis of has not even begun. Future work with these data would include mapping the 3d magnetic field of the solar prominences, which hasn't been done at this resolution.

Another item which could be studied in the future is the oscillation which was discovered in the velocity maps.. This oscillation could be of use for future studies of prominence magnetism.

Additional future work would potentially include the acquiring of a faster,

lower noise SHWFS camera. During the SPIE conference, in August of 2013, I talked with a representative of Hamamatsu. He had a camera which could possibly be read at over 1000 fps, for a small ROI. This camera, he stated had a read noise of 3 electrons, rms, at this high speed.(Hamamatsu 2014) The camera costs 10X the amount of the one we were using, however. Also, it wasn't clear if it could only achieve this high speed using a rolling shutter readout mode, which would distort the images in each subaperture, if they changed at high speed. A similar camera from Andor was examined, who explain the rolling/global shutter problem.(Andor 2014) If the Hamamatsu camera were capable of running fast enough, with a satisfactory read-out characteristic, then it would be trivial to measure the wavefront with more subapertures, due to the very low read-noise. The other option would be a purpose-built intensified, or emccd camera, which also have exceedingly low read-out noise, but are also extraordinarily expensive.(Denvir & Conroy 2003) If such a camera were available, we would be able to utilize the full 10X10 SHWFS array that our DMs were designed for. Indeed, I feel that the ATST team should consider such a camera for the SHWFS of their proposed off-limb AO system.

APPENDICES

APPENDIX A. CAMERA PROPERTIES

Barry & Burnell (2000) show how to measure Gain and Read-Noise for a CCD camera. First:

$$\sigma_{pe}^2 = g\bar{S}_{ADU}, \tag{A.1}$$

where σ_{pe}^2 is the image variance, measured in Photo-Electrons, g is the gain factor, the number of Photo-Electrons per ADU, and $\bar{S}_{ADU}$ is the average signal, measured in a flat-field image. Furthermore:

$$\sigma_e = g\sigma_{ADU}, \tag{A.2}$$

where σ_e is the total noise, in terms of electrons, and σ_{ADU} is the same, in terms of ADUs. Since noise adds in quadrature:

$$\sigma_e^2 = \sigma_{pe}^2 + \sigma_{ron}^2, \tag{A.3}$$

where σ_{ron}^2 is the Read-Noise. Substituting equations A.1 and A.2 into equation A.3, we find:

$$g^2\sigma_{ADU}^2 = g\bar{S}_{ADU} + \sigma_{ron}^2. \tag{A.4}$$

Equivalently:

$$\sigma_{ADU}^2 = \frac{1}{g}\bar{S}_{ADU} + \frac{1}{g^2}\sigma_{ron}^2. \tag{A.5}$$

This is simply a linear function of the form, $y = mx + b$.

According to Barry & Burnell (2000), the best way to find the variance of a flat-field image, σ_{ADU}^2, is to subtract one flat field from another, and divide the variance of the resulting image by 2, since this image will have double the variance of the original flat-fields (Barry & Burnell 2000). One then plots the mean signal for flat-fields of increasing exposure length, $\bar{S}_{ADU}$ vs σ_{ADU}^2. The slope of a linear

fit to these points is $\frac{1}{g}$, and the intercept is $\frac{1}{g^2}\sigma_{ron}^2$. It is then trivial to solve for σ_{ron}.

To do this, 1000 frames were taken of a stable, fiber-optic lamp at each of several frame rates, namely: 950, 900, 850, 800, 750, 700, ..., 250 fps. (Slower than that and the camera began to saturate.) All frames were dark-subtracted, using the average of 100 dark frames, at each frame rate. $\bar{S}_{ADU}$ for each frame rate was simply the average over all the pixels, for all of the frames. σ_{ADU}^2 was found as follows:

$$\sigma_{ADU}^2 = \frac{1}{999}\sum_{i=1}^{999} variance(flat_i - flat_{i+1})/2 \tag{A.6}$$

The properties of each camera were measured. The gain and read-noise for each are shown below.

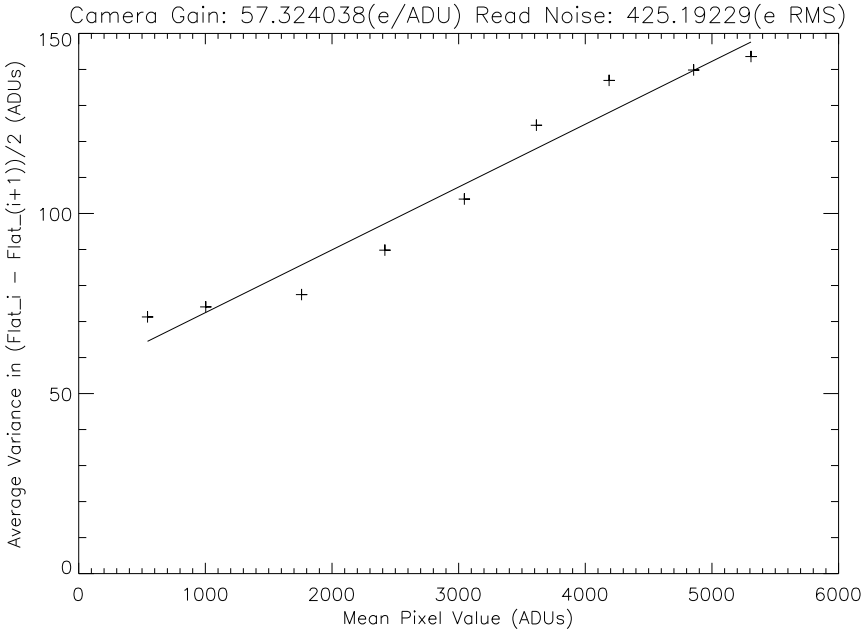

Fig. A.1.— The gain and read-noise, measured for the FLIR Camera.

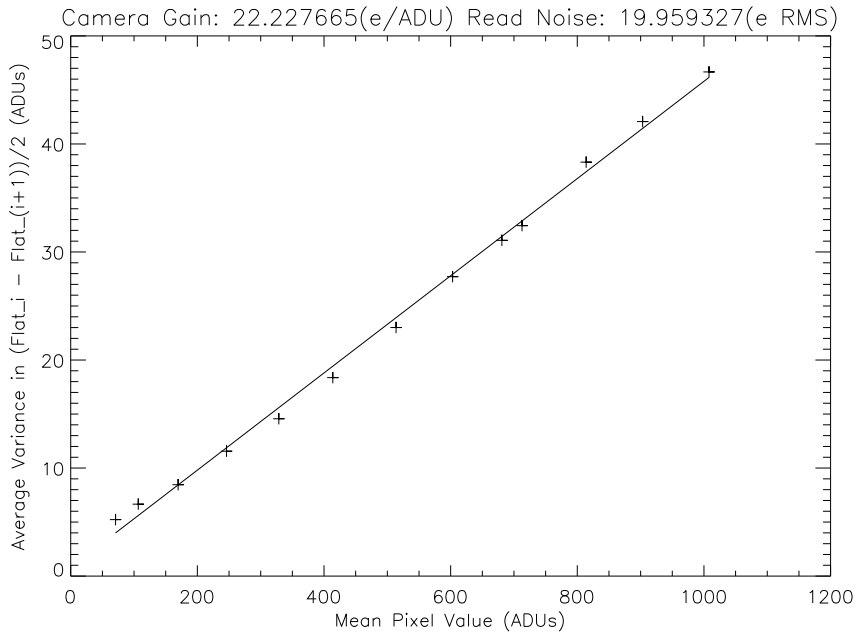

Fig. A.2.— The gain and read-noise, measured for the D7.

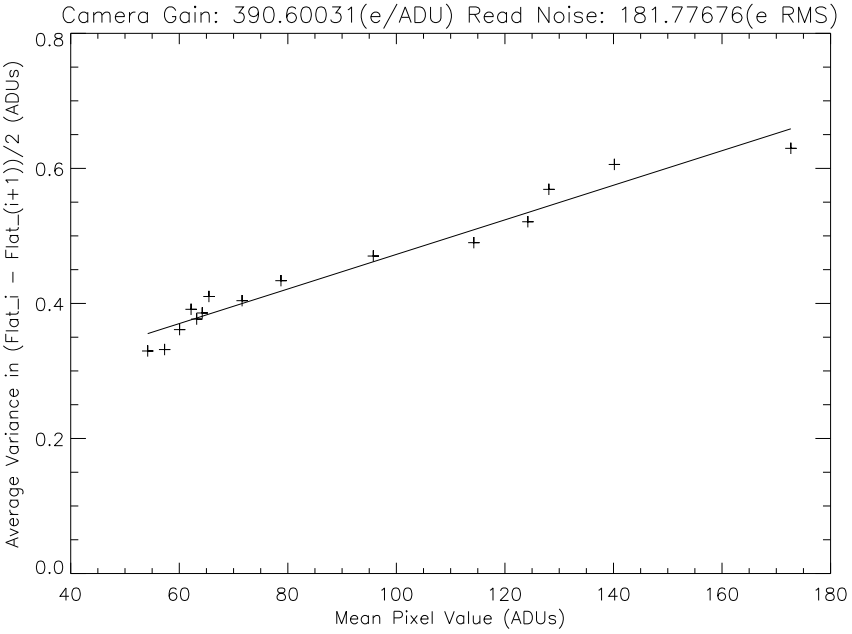

Fig. A.3.— The gain and read-noise, measured for the D6.

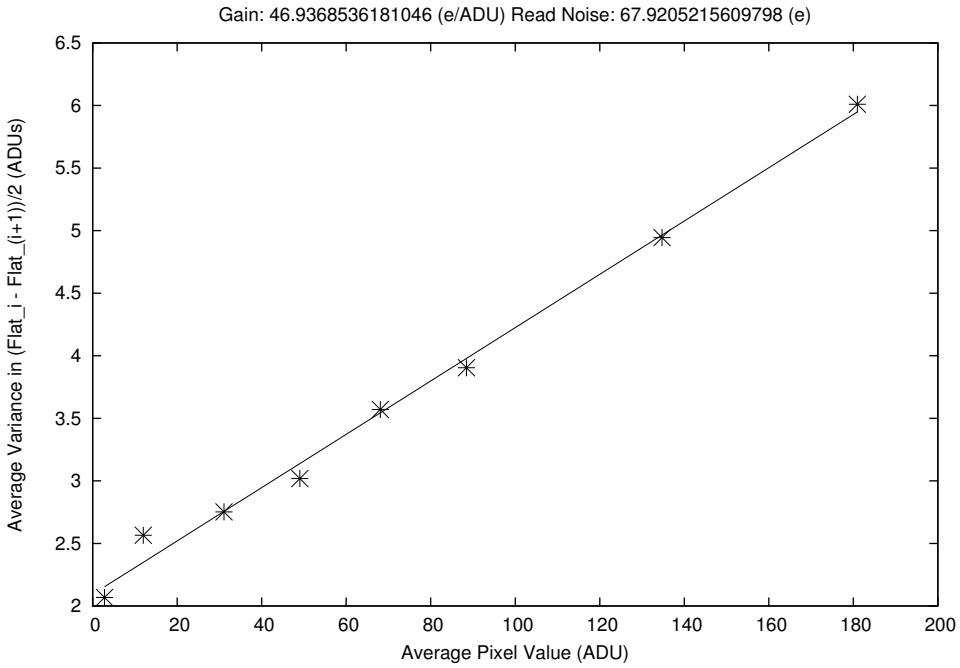

Fig. A.4.— The gain and read-noise, measured for the VGA300hg.

APPENDIX B. RADIOMETRY

B.1. Light Transmission

A photometric analysis was performed for the optimum SHWFS configuration, following the method of Dereniak & Boreman (1996). This analysis takes into account the reflectance and transmission of all mirrors, lenses, and optical windows on the DST and our optical bench.

In order to determine the light throughput of an optical system, one needs to first take into account the transmission or reflectance of each optical element. Dereniak & Boreman (1996) show how this is to be done. This analysis is first performed without taking scattering into account. Dereniak & Boreman (1996) gives the transmission of an uncoated lens as follows:

$$t = \frac{4n_2 n_1}{(n_2 + n_1)^2}, \tag{B.1}$$

where n_2 is the index of refraction of the lens and n_1 is the index of refraction of the medium in which the lens is placed. For air, $n_1 \approx 1$ (Dereniak & Boreman 1996). The total throughput is:

$$T = \sum t \times \sum R. \tag{B.2}$$

That is the sum of all lens transmission times the sum of all mirror reflections.

The telescope its self has 2 silica windows and 3 aluminum coated mirrors (see NSO/SP 2011). For one setup, we used 7 fused silica lenses and a BK7 lenslet. There were also 5 Ag coated mirrors. There were, additionally, 2 95/5 beam splitters in the beam. This yields a total throughput, ignoring filters for

Table B.1. Optical Properties of Lenses and Mirrors

Materials Used	
n fused silica	1.46
n BK7	1.51
R Al	90%
R Ag	95%
t fused silica	96.50%
t BK7	95.87%
t 95/5 Beam splitter, silica	91.65%
t Prefilters	70%

Table B.2. Number of Optical Elements

Element Type	Number
Fused Silica Lens or Window	9
BK7 Lens or Window	1
Al Mirror	3
Silver Mirror	5
95/5 Beam Splitter	2
Prefilters	2

now, of 32.9%. Schmitt et al. (1983) found that high quality lenses have minimum a scattering ratio of about 1%. The same scattering is assumed for the mirrors as an adequate measure of this could not be found. That should make t for each type of lens 1 percentage point lower. Taking this into account for all lenses and mirrors, the total throughput is found to be 26.7%. There are additionally two prefilters, for blocking out-of-band light, each with a transmission at Hα of about 70%. Adding in the two prefilters, the total transmission becomes 13.1% The optical setup, downstream of the telescope, is shown in Figure B.1.

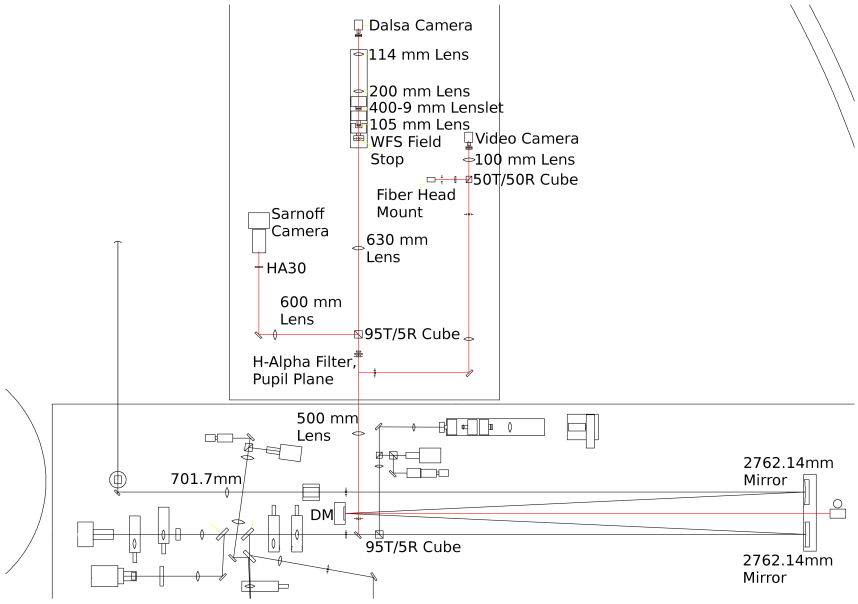

Fig. B.1.— The sample setup that was used for the radiometry calculations.

B.2. Filter Properties

For this set of experiments, The same type filter was utilized that will be used on the ATST Visible Broadband Imager.(Rimmele et al. 2014) The filter

transmission was found by dividing the average rows of a raw spectrum, taken through the filter, Figure B.2, with an averaged, calibrated reference spectrum, Figure B.3. The resultant transmission spectrum is shown in Figure B.4.

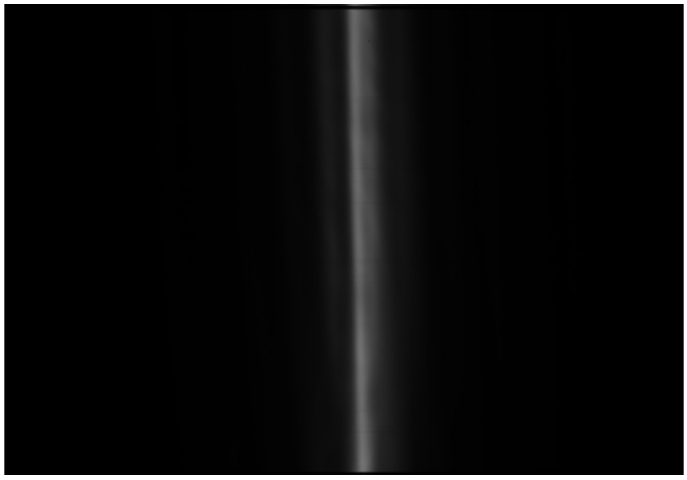

Fig. B.2.— Raw Filter Spectrum.

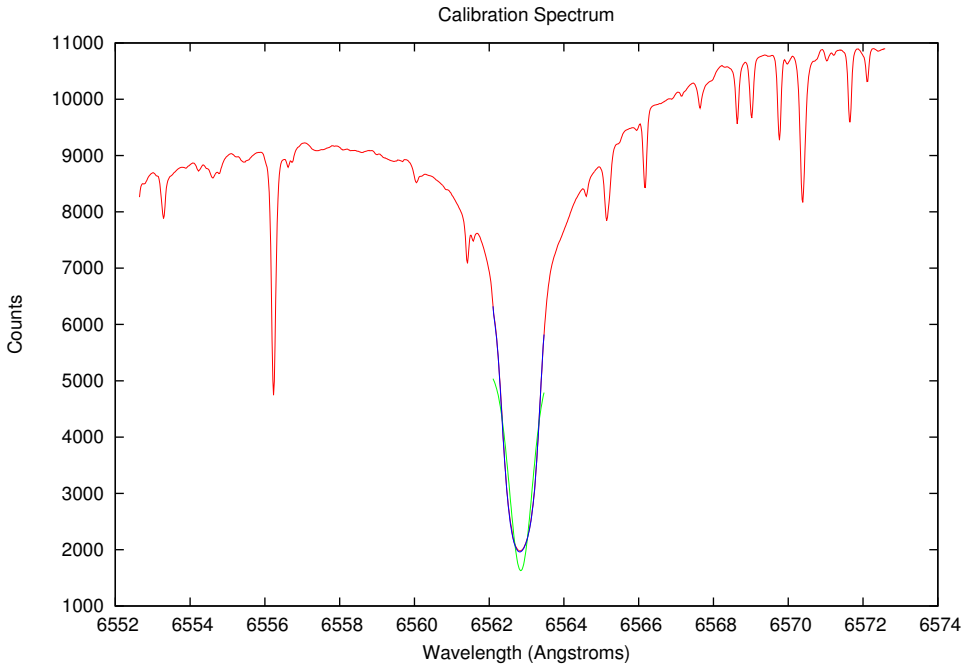

Fig. B.3.— Filter Calibration Spectrum.

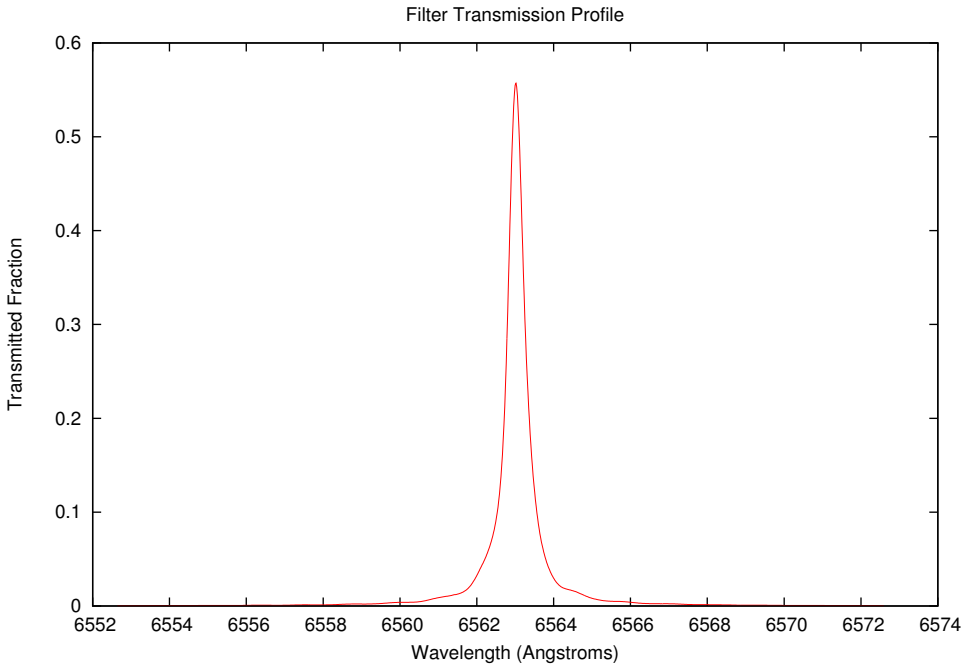

Fig. B.4.— Calibrated Filter Spectrum.

B.3. Total Throughput

Gaussian shapes were assumed for the Hα emission line with a range of Full Width Half Maximum (FWHM) and radiance values as measured by Landman & Mongillo (1979). For convenience, their Hα radiance and FWHM values are tabulated in Table B.3. The percentage of each prominence's light that would make it through the filter was determined by creating a normalized Gaussian function with FWHM in Å, as as tabulated, with the center at 6562.8 Å. This function was multiplied by the filter transmission and integrated, to get the total throughput in %. (Integrating the original function will get a value of 100 %, since it's normalized.) To determine the photon flux per pixel, the following is employed:

$$\Phi = \left(\frac{L \times \Omega \times A}{\frac{hc}{\lambda}} \right) \times T, \tag{B.3}$$

where Φ is the photon flux, L is the radiance from Table B.3, Ω is the solid angle subtended by one pixel, A is the subaperture area, and T is the percent of light transmitted. h is Planck's Constant, 6.626×10^{-27}erg s, c is the speed of light, and λ is 6562.8 Å. Ω is defined by:(Dereniak & Boreman 1996)

$$\Omega = 2\pi(1 - cos(\theta)), \tag{B.4}$$

for a circular area, where θ is the angle subtended by a pixel. For a square area, this becomes:

$$\Omega = 8(1 - cos(\theta)), \tag{B.5}$$

since the area of a circle is πr^2, and that of a square is $4r^2$. For a pixel which subtends 0.82 $''$, $\Omega = 1.584 \times 10^{-11}$sr. The subapertures used in the Off-Limb AO System are 13.07cm on a side, which comes comes out to 170.825cm^2. The

photon flux is tabulated, along with the radiance values, in Table B.3. The Falcon VGA300hg has a gain of 46.937 e^- ADU^{-1}, and a Quantum Efficiency of 55% at 6563 Å. So the total raw counts expected per second is found by dividing the photon flux by the gain and multiplying it by the Quantum Efficiency. This is also tabulated in Table B.3. All of the prominence images that were checked, have raw counts that fall within the range tabulated.

Table B.3. Prominence Radiance and FWHM

Radiance of Prominence (10^4 ergs cm^{-2} s^{-1} sr^{-1})	FWHM Å	Filter Transmission Percent	Photon Flux pixel^{-1} ms^{-1}	Raw Counts ADU ms^{-1}
9.8600	0.6853	28.6758	3300.7801	38.6780
4.4100	0.6006	29.7611	1532.1823	17.9539
13.2400	0.9625	25.0568	3872.9013	45.3820
11.6100	0.8455	26.5560	3599.3065	42.1761
9.9000	0.7962	27.2058	3144.2738	36.8441
5.7100	0.6453	29.1969	1946.2363	22.8057
5.6500	0.6545	29.0776	1917.9215	22.4739
9.5900	0.7484	27.8400	3116.8140	36.5223
8.1600	0.7007	28.4730	2712.3607	31.7830
4.5800	0.6406	29.2562	1564.2519	18.3296
8.3100	0.6222	29.4915	2861.0208	33.5250
4.2500	0.5482	30.3860	1507.6001	17.6658
9.9900	0.6345	29.3350	3421.1732	40.0887
6.5700	0.5914	29.8747	2291.3540	26.8497
12.6300	0.6684	28.8976	4260.7701	49.9270
5.9000	0.5852	29.9497	2062.8532	24.1722
8.0300	0.6083	29.6655	2780.9300	32.5865
2.6500	0.5991	29.7801	921.2876	10.7955
3.7400	0.5883	29.9123	1306.0042	15.3035
4.7900	0.6145	29.5884	1654.5533	19.3878
1.1100	0.5344	30.5424	395.7767	4.6376
8.6300	0.6129	29.6077	2982.9040	34.9532

APPENDIX C. PHASE-DIVERSE WAVEFRONT SENSOR

C.1. Introduction to Phase-Diversity

An alternate approach to deriving wavefront sensor information from prominence structure is Phase-Diversity (PD) (Gonsalves & Childlaw 1979; Gonsalves 1982). The use of phase-diverse wavefront sensors in real-time adaptive optics systems has been proposed and tested by Paxman et al. (2007) (see also Georges III et al. 2007; Warmuth et al. 2008). As opposed to the Shack-Hartman approach, PD uses images obtained with the full aperture of the telescope.

We analyzed the PD images, following the method outlined by Gonsalves & Childlaw (1979), Gonsalves (1982), and Löfdahl & Scharmer (1994). We processed a series of solar prominence images in order to extract the wavefront. These images are obtained by splitting the light beam into two components; one out of focus by a known amount from the other. Both images were recorded side-by-side, on the same CCD. The amount of defocus can vary, depending upon the seeing and other factors, however it must be known. The phase diversity algorithm performed a maximum likelihood analysis to determine the most likely optical wavefront, given the two simultaneous images. Figure C.1 shows the output of the PD algorithm.

For these tests, we utilized the Dunn Solar Telescope (DST), operating at f/32.5. We utilized a Dalsa camera, with 12 micron pixels (Datasheet 1999), yielding a pixel scale of $0.1''$ pixel^{-1}. We used an amateur filter, from Coronado instruments, with a Full Width Half Maximum FWHM of 0.7Å, centered on 6563Å (H-α). This filter is a two part system, with an ètalon that is placed in front of an amateur telescope and an interference filter which goes in front of an eyepiece. This filter was selected due to its wide bandpass, in order to maximize

the amount of light received at the CCD. However, the overall transmission of this system is approximately 0.25%, in the H-α band. This low transmission is required for eye safety (Meade 2008). (A fact that we realized only after we had attempted to use the filter.) To increase our transmission, the ètalon alone and employed one of the available interference filters. The measured flux levels were approximately 10 times higher with this setup, than with the stock filter. With this filter configuration, our exposure times were between 100 and 250 ms. A high transmission filter is on order, as stated in §2.1, but was not available at the time of these tests. This filter has a FWHM of 0.5Å and a transmission of $> 50\%$. We will repeat these observations, with this new filter.

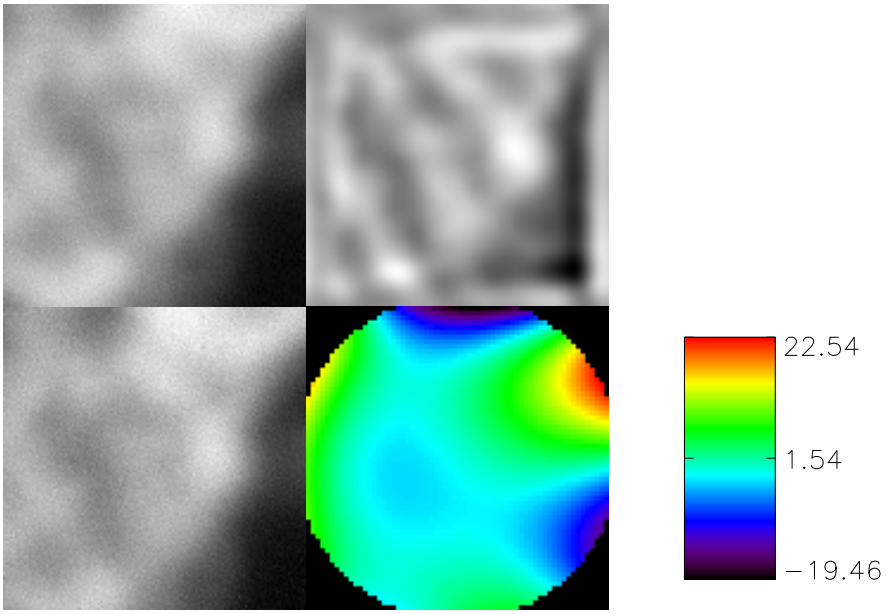

Fig. C.1.— Output of the Phase-Diversity program. On the left are the defocused and focused images, top and bottom respectively. On the top right is an estimate of the true object that was imaged, correcting for atmospheric aberrations. The bottom right shows an estimate of the wavefront as it entered the telescope. The scale is in units of radians (2π per wavelength of light, Hα, in this case). The code is measuring 15 Zernike modes in this example.

This wavefront is decomposed into the Zernike Polynomials. Once the Zernike

polynomials were determined, we analyzed their temporal variance, over the course of 100 frames, as was done in §2.1. Tip and Tilt, Z_2 and Z_3, can't be measured by PD, but can be measured separately (Löfdahl & Scharmer 1994).

In order to verify the output of the PD algorithm, several simulations were run. Using the software packages CAOS and AIRY (Cabrillet et al. 2004; Correia et al. 2002). With CAOS, we generated a model atmosphere, which obeyed Kolmogorov statistics (Noll 1976). A model wavefront from a distant point source was transmitted through this atmosphere and focused into two images, or Point Spread Functions (PSFs), one in focus and one which was 1 wave out of focus. The atmosphere was evolved and, PSFs were taken at frame rates from 500 Hz to 1 kHz. AIRY was used to save these PSFs in FITS format. The PSFs were then convolved with a sharp image of solar granulation, which was found on the NSO website (see NSO/SP 2002), since PD seems to work well for this sort of data (Löfdahl & Scharmer 1994). The PD algorithm was then run on these aberrated images.

Additionally, the PD algorithm was tested using a set of PD data which were taken of solar granulation (G-band data, courtesy of Scott Acton), to compare those results with the prominence data and with our simulations.

C.2. PD Results

The results of PD prominence wavefront sensor experiment are shown in Figure C.2.

It is evident, in Figure C.2, that the PD code was not able to reconstruct valid wavefront variances for our prominence data, due to the extremely noisy nature

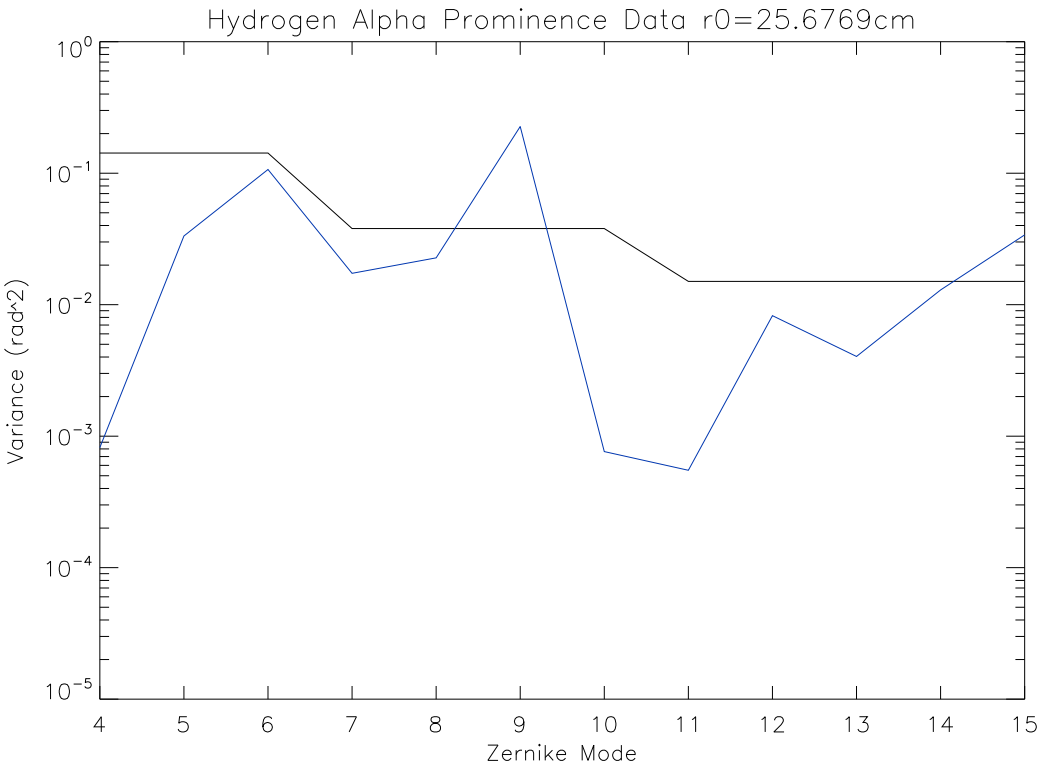

Fig. C.2.— Temporal variance of the calculated Zernike modes for the prominence data. Line colors are the same as in Figure 2.2. As stated above, Tip and Tilt, Z_2 and Z_3, can't be measured by PD. Thus, this graph and Figure C.3 are plotted, beginning at Z_4.

of the plotted variances. Figure shows the results from one of our simulations and the G-band data, as discussed in §C.1.

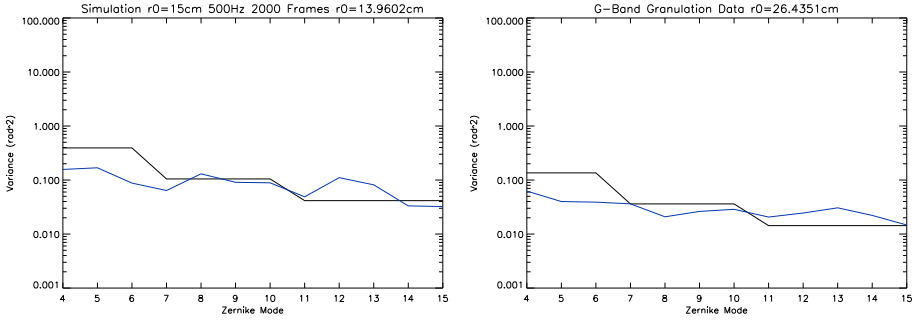

Fig. C.3.— Temporal variance of the calculated Zernike modes for simulated data (left) and the sample data. Line colors are the same as in Figure 2.2.

One can note that the measured Zernike Variances for both our simulation and the G-band data seem to follow the expected trend, in a general sense. Also note that the measured value for r0 in the simulation is close to the r0 that was input into the simulations. The expected variances were scaled to the measured variances via minimizing the average difference between the measured and estimated values.

C.3. Discussion

The Shack Hartmann wavefront sensor seems to be able to deliver the desired wavefront information and at this point appears to be the best option for the proposed Limb AO system. Remaining issues with this approach are the low flux levels available, which may drive the system towards a low order correction. Alternatively, em-CCDs could be utilized, which would greatly reduce the major source of noise at low flux levels, read noise. Thus allowing the necessary measurements to be made (e.g. Denvir & Conroy 2003; Feautrier et al. 2011).

Although the PD code does not appear to accurately reconstruct incoming wavefronts for this application, it does register some temporal variance in the Zernike modes. However, as we have shown in Figure C.2, the measured variance curve is extremely noisy. A discussion with Oskar von der Lühe (private communication) indicated that the extremely low contrast and lack of high spatial frequency content, likely due to the long exposure times and bad seeing conditions, shown in the data was insufficient for the PD technique to determine the wavefront.

REFERENCES

Andor. 2014, http://www.andor.com/scientific-cameras/neo-and-zyla-scmos-cameras/zyla-55-scmos http://www.andor.com/learning-academy/rolling-and-global-exposure-essential-why-should-buyers-understand-rolling-and-global-shutter

Ballester, J. L. 2014, in IAU Symposium, Vol. 300, IAU Symposium, 30–39

Barry, R., & Burnell, J. 2000, The Handbook of Astronomical Image Processing (Richmond, VA: Willmann-Bell, Inc.)

Berger, T. 2014, in IAU Symposium, Vol. 300, IAU Symposium, 15–29

Berger, T., et al. 2011, Nature, 472, 197

Berger, T. E., et al. 2010, ApJ, 716, 1288

Berkefeld , T., Schmidt, D., Soltau, D., von der Lühe, O., & Heidecke, F. 2012, Astronomische Nachrichten, 333, 863

Born, M., & Wolf, E. 1999, Principles of Optics, seventh edn. (Cambridge, UK: Cambridge University Press)

Cabrillet, M., et al. 2004, Proceedings of the SPIE, 5490, 637

Carrol, B. W., & Ostlie, D. A. 1996, An Introduction to Modern Astrophysics, 1st edn. (Reading, Massachusetts, etc.: Addison-Wesley Publishing Company, Inc.)

Cavallini, F. 2006, Solar Physics, 236, 415

Cavallini, F., & IBIS Team. 2004, in Bulletin of the American Astronomical Society, Vol. 36, American Astronomical Society Meeting Abstracts #204, 710

Chandrasekhar, S. 1981, Hydrodynamic and Hydromagnetic Stability (Mineola, NY: Dover Publications, Inc.)

Chen, P. F. 2011, Living Reviews in Solar Physics, 8, 1

Correia, S., et al. 2002, Astronomy and Astrophysics, 387, 733

Dai, G.-M. 1995, Journal of the Optical Society of America A, 12, 2182

Datasheet, D. C.-D. 1999, www.ni.com/third_party/dalsa/pdf/ca_d4_d7.pdf

Davidson, P. A. 2001, An Introduction to Magnetohydrodynamics (Cambridge, New York, Melbourne, Madrid, Cape Town, Singapore, São Paolo: Cambridge University Press)

de Toma, G., Casini, R., Burkepile, J. T., & Low, B. C. 2008, ApJ, 687, L123

Denvir, D. J., & Conroy, E. 2003, Proceedings of the SPIE, 4796, 164

Dereniak, E., & Boreman, G. 1996, Infrared Detectors and Systems (Hoboken, NJ: John Wiley and Sons, Inc)

Feautrier, P., et al. 2011, Publications of the Astronomical Society of the Pacific, 123, 263

Fried, D. L. 1965, Journal of the Optical Society of America (1917-1983), 55, 1427

—. 1990, Journal of the Optical Society of America A, 7, 946

Georges III, J. A., et al. 2007, Proceedings of the SPIE, 6711, 671105

Gonsalves, R. A. 1982, Optical Engineering, 21, 829

Gonsalves, R. A., & Childlaw, R. 1979, Proceedings of the SPIE, 207, 32

Guyon, O. 2002, Astronomy and Astrophysics, 387, 366

Hamamatsu. 2014, http://www.hamamatsu.com/us/en/community/life_science_camera/product/search/C11440-22CU/index.html

Hardy, J. 1998, Adaptive Optics for Astronomical Telescopes (New York: Oxford Univ. Press)

HCR. 2014, Heliophysics Coverage Registry: http://www.lmsal.com/get_aia_data/

Jaeggli, S. A., Lin, H., Mickey, D. L., Kuhn, J. R., Hegwer, S. L., Rimmele, T. R., & Penn, M. J. 2010, Mem. S.A.It., 81, 763

Jansson, P. A. 2012, Deconvolution of Images and Spectra, 2nd edn. (Mineola, NY: Dover Publications)

Khomenko, E., Díaz, A., de Vicente, A., Collados, M., & Luna, M. 2014, in IAU Symposium, Vol. 300, IAU Symposium, 90–93

Kippenhahn, R., & Schlüter, A. 1957, ZAp, 43, 36

Labrosse, N., et al. 2010, Space Science Reviews, 151, 243

Landman, D. A., & Mongillo, M. 1979, Astrophysical Journal, 230, 581

Löfdahl, M. G., & Scharmer, G. B. 1994, Astronomy and Astrophysics Suppl., 107, 243

MacKay, D. H., et al. 2010, Space Science Reviews, 151, 333

Marino, J. 2007, PhD thesis

Meade. 2008, www.optcorp.com/pdf/OPT/EDU/coronado_safety.pdf

Michau, V. 2002, Internal ONERA Report, ONERA, France

Michau, V., Rousset, G., & Fontanella, J. 1993, in Real Time and Post Facto Solar Image Correction, ed. R. R. Radick, 124

NASA Mission to Geospace. 2011, http://pwg.gsfc.nasa.gov/istp/outreach/theretohere.html

NIST. 2014, National Institute of Standards and Technology: http://physics.nist.gov/PhysRefData/ASD/lines_form.html and http://physics.nist.gov/cgi-bin/cuu/Value?c

Noll, R. J. 1976, Optical Society of America, Journal, 66, 207

NSO/SP. 2002, http://nsosp.nso.edu/dst/pics.html

—. 2011, http://nsosp.nso.edu/node/85

O'Connel. 2003, http://www.astro.virginia.edu/class/oconnell/astr511/lec13-f03.pdf

Orozco Suárez, D., Asensio Ramos, A., & Trujillo Bueno, J. 2013, in Highlights of Spanish Astrophysics VII, 786–791

Paxman, R. G., et al. 2007, Proceedings of the SPIE, 6711, 671103

pdl.perl.org. 2014, http://pdl.perl.org/

Ren, D., Hegwer, S. L., Rimmele, T., Didkovsky, L. V., & Goode, P. R. 2003, in Society of Photo-Optical Instrumentation Engineers (SPIE) Conference Series, Vol. 4853, Society of Photo-Optical Instrumentation Engineers (SPIE) Conference Series, ed. S. L. Keil & S. V. Avakyan, 593–599

Rimmele, T., Berger, T., Casini, R., Elmore, D., Kuhn, J., Lin, H., Schmidt, W., & Wöger, F. 2014, in IAU Symposium, Vol. 300, IAU Symposium, 362–369

Rimmele, T. R., & Marino, J. 2011, Living Reviews in Solar Physics, 8, 2

Rimmele, T. R., & Radick, R. R. 1998, Proceedings of the SPIE, 3353, 72

Roddier, F., ed. 1999, Adaptive Optics in Astronomy (London: Cambridge Univ. Press)

Ryutova, M., Berger, T., Frank, Z., Tarbell, T., & Title, A. 2010, Sol. Phys., 267, 75

Scharmer, G. B., Dettori, P. M., Lofdahl, M. G., & Shand, M. 2003, in Society of Photo-Optical Instrumentation Engineers (SPIE) Conference Series, Vol. 4853, Society of Photo-Optical Instrumentation Engineers (SPIE) Conference Series, ed. S. L. Keil & S. V. Avakyan, 370–380

Schmidt, D., et al. 2010, Proceedings of the SPIE, 7736, 773607

Schmitt, P. S., Webb, T. W., & Barnett, E. H. 1983, Appl. Opt., 22, 2416

Schrijver, C. J., & Siscoe, G. L., eds. 2009, Heliophysics: Plasma Physics of the Local Cosmos (London: Cambridge Univ. Press)

Stellmacher, G., & Wiehr, E. 1973, A&A, 24, 321

Tandberg-Hanssen, E. 1995, The Nature of Solar Prominences (Dordrecht: Kluwer Academic Publishers)

Taylor, G. E., Rimmele, T. R., Marino, J., & McAteer, R. T. J. 2013, in Society of Photo-Optical Instrumentation Engineers (SPIE) Conference Series, Vol. 8862, Society of Photo-Optical Instrumentation Engineers (SPIE) Conference Series

Taylor, G. E., Rimmele, T. R., Marino, J., Tritschler, A., & McAteer, R. T. J. 2012, in Astronomical Society of the Pacific Conference Series, Vol. 463, Second ATST-EAST Meeting: Magnetic Fields from the Photosphere to the Corona., ed. T. R. Rimmele, A. Tritschler, F. Wöger, M. Collados Vera, H. Socas-Navarro, R. Schlichenmaier, M. Carlsson, T. Berger, A. Cadavid, P. R. Gilbert, P. R. Goode, & M. Knölker, 321

Tyson, R. 2000, Introduction to Adaptive Optics (Bellingham, WA: SPIE Press)

—. 2011, Principles of Adaptive Optics, 3rd edn. (Boca Raton, FL: CRC Press)

Warmuth, M. W., et al. 2008, Proceedings of the SPIE, 7093, 709307

Welch, P. D. 1967, IEEE Trans. Audio Electroacoust., Volume AU-15, p. 70-73, 15, 70